UCLouvain

École polytechnique de Louvain

Superelastic Alloy Rebars for Improved Seismic Response of Reinforced Concrete Wall Buildings

Author: **Baudouin de Kerautem**
Supervisors: **João Saraiva Esteves Pacheco De Almeida, Ryan Hoult**
Readers: **Aude Simar, Martin Steinmetz**
Academic year 2021–2022
Master [120] in Civil Engineering

Abstract

Nowadays, earthquakes in addition to killing thousands of people each year (45000 people killed/year) lead to high economic losses. Modern codes fulfil the ductile failure objectives during rare or very rare earthquakes, while new objectives propose a new performance level of repairable buildings after these seismic events.

Shape Memory Alloy, used as reinforcement can help to achieve this goal, a new material that has the ability to recover large strains upon removal of stress is studied in this master thesis, NiTi rebars, an alloy of Nickel and Titanium, are used for the experimental tests.

Three RC beams of 2m x 0.19m x 0.15m are built, the first one as a control beam, the two others with 10cm of NiTi at mid-span (in the plastic hinge). The beams were tested in three point-bending. A new connection was studied, welded rather than a mechanical coupler, optical fibres were used to determine the strains in the rebars.

A numerical study is conducted and the results are compared with the experimental results.

Acknowledgements

This master thesis would have been impossible without the help of several people that I want to warmly thank.

First of all, thank you to Pr. Almeida and Dr. Hoult who helped, guided and encouraged me all this year. They took the time for answering my questions, have Namazu meetings and get me back on track when I was blocked and didn't know how to go further.

Thank you to the LEMSC who helped me with the experimental tests, from the purchase of the materials, the preparation of the tests and the realisation of the tests. Thank you to Alex Bertholet who helped me for the optical fibres installation and practical aspects of the master thesis, Christophe Bayart who managed the installation of the experimental set-up and helped with the jack's stroke process during the tests, Pierre Mertens de Wilmars for the welding of stirrups and longitudinal rebars, Stéphane Gorski for the casting of the concrete and the tests on cubes and cylinders, Quentin Mestrez for the DIC device installation and calibration. Thank you also to Catherine Doneux for the help and monitoring of the experimental tests.

Thank you also to Matthieu Lezaack and the people of the LACaMI who helped me with the friction welding.

Thank you to my jury to read this master thesis, Aude Simar and Martin Steinmetz.

Finally, thank you to my friends and family who encouraged me.

CONTENTS

Abstract ii

Acknowledgments iii

1 Introduction 1
- 1.1 Motivation . . . 1
- 1.2 Objectives . . . 4
- 1.3 Organisation . . . 5

2 State of the art 7
- 2.1 Shape Memory Alloys . . . 8
  - 2.1.1 Austenite and Martensite . . . 9
  - 2.1.2 Shape memory effect and Superelasticity . . . 10
  - 2.1.3 Applications for civil engineering structures . . . 12
- 2.2 Experimental tests with shape memory alloys . . . 14
  - 2.2.1 Beams . . . 15
  - 2.2.2 Walls . . . 23
  - 2.2.3 Columns . . . 26
  - 2.2.4 Beam-Column joints . . . 30
- 2.3 Loading rate effect . . . 32

3 Numerical analysis 35
- 3.1 Finite Element Modelling . . . 35

3.2 Calibration of VecTor2 . . . 35
3.2.1 Mesh sensitivity analysis . . . 36
3.2.2 Material models . . . 40
3.3 Description of the finite element model . . . 47
3.3.1 Material properties . . . 47
3.3.2 Link elements . . . 50
3.3.3 Numerical models . . . 51

4 Experimental tests **53**
4.1 Experimental setup . . . 53
4.1.1 Description of the beams . . . 53
4.1.2 Support conditions . . . 54
4.2 Loading protocol . . . 56
4.3 Steel properties . . . 59
4.4 SMA properties . . . 60
4.5 SMA-Steel welded connection . . . 60
4.5.1 Process . . . 60
4.5.2 Properties . . . 62
4.6 Concrete properties . . . 63
4.7 Instrumentation . . . 63
4.7.1 Optical fibre . . . 63
4.7.2 Others . . . 65

5 Results and analysis **69**
5.1 Beam S1 . . . 69
5.1.1 Load-Displacement response . . . 69
5.1.2 Recovered displacements . . . 70
5.1.3 Strains . . . 71
5.1.4 Cracks . . . 73
5.2 Beam N1 . . . 74
5.2.1 Load-Displacement response . . . 74
5.2.2 Recovered displacements . . . 75
5.2.3 Strains . . . 75
5.2.4 Cracks . . . 76
5.2.5 Temperature . . . 76
5.3 Beam N2 . . . 78
5.3.1 Load-Displacement response . . . 78
5.3.2 Recovered displacements . . . 79
5.3.3 Strains . . . 79
5.3.4 Cracks . . . 80
5.4 Numerical results . . . 80

5.4.1 Beam S1 . . . 80
5.4.2 Beam N1 . . . 82
5.5 Overall comments . . . 83

6 Comparison between numerical and experimental results 87
6.1 Beam S1 . . . 88
6.1.1 Load-Displacement curves comparison . . . 88
6.1.2 Residual displacements comparison . . . 88
6.2 Beams N1 and N2 . . . 89
6.2.1 Load-Displacement curves comparison . . . 89
6.2.2 Residual displacements comparison . . . 90

7 Conclusion 93
7.1 Future developments . . . 94

Bibliography 95

A Construction of the beams 105

B Experimental tests 107

C Strains of beam N2 111

CHAPTER

1

INTRODUCTION

1.1 Motivation

Nowadays, earthquakes (ground motion and tsunamis) in addition to killing thousands of people each year (45000 people killed/year [1]) lead to high economic losses and are responsible for nearly 20% of all the economical losses due to natural disasters (floods, storms, landslides, epidemic,...)[2]. Figure 1.1 shows the estimated damages by country between 2000 and 2022 due to earthquakes. And Fig. 1.2 indicates the 10 countries with the biggest estimated damages in US$.
This budget goes mainly to the reconstruction of broken buildings due to failure of structural elements or to important permanent deformations. For example, the Christchurch earthquakes in 2010-2011 in New Zealand took place from September 2010 to December 2011. These earthquakes involved widespread damage during the February 2011 event and ongoing aftershocks led the country to big economical losses (the total estimated damage was up to $40 billion $\approx 20\%\ GDP$), demolition of approximately 60 % of multi-storey concrete buildings (3 storeys and up), and closure of the core business district for over 2 years [3].

Modern design standards (for example Eurocode 8 [4]) try to obtain ductile failure and avoid brittle failure of RC structures. Fig. 1.3 presents the current performance objective matrix, after a very rare or rare earthquake, it's accepted to have non repairable buildings. Damages and permanent deformations of the

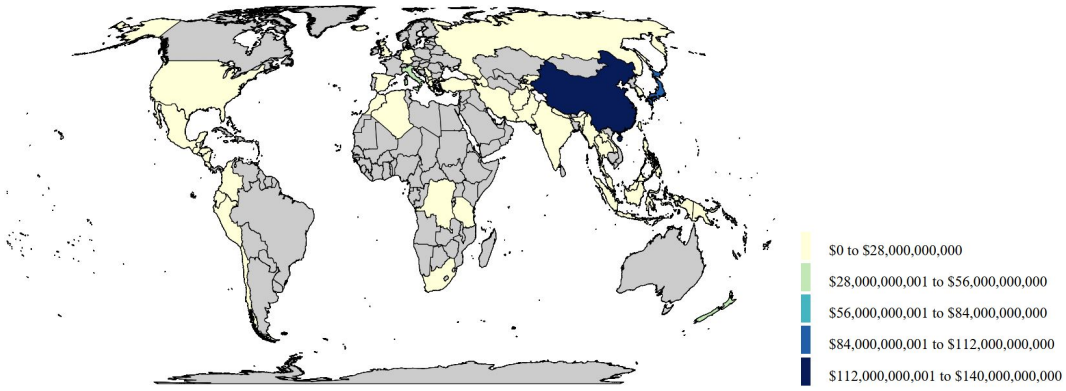


Figure 1.1: Total estimated damages(in US$) from Ground movement Disasters, 2000 to 2022 [2]

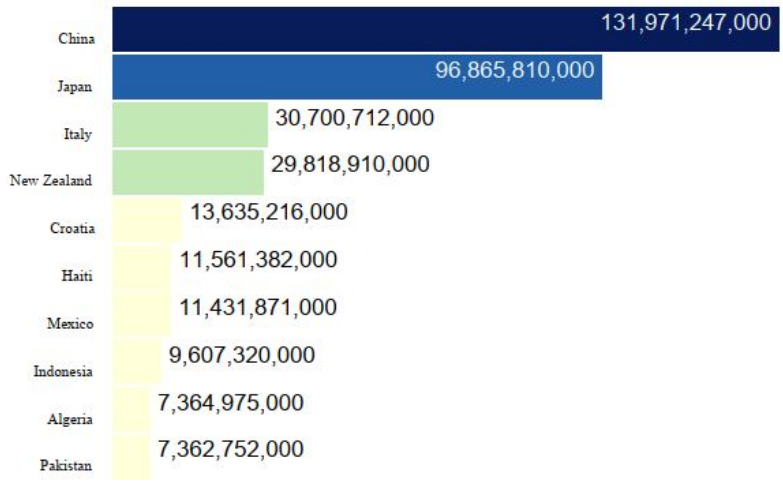


Figure 1.2: Total estimated damages(in US$) from Ground movement Disasters, 2000 to 2022 [2]

structure can prevent the building from being serviceable and in some cases require demolition. The proposed goal is to avoid non repairable buildings after seismic events, as written on the proposed performance objective matrix. The link between the inter-story drift (i.e. residual deformation divided by the story's height) and the damage state is shown in table 1.1. If the residual deformation can be limited at the reparable damage state (inter-story drift $< 0.5\%$), it can lead to great economical and life savings.

When a RC wall is subjected to seismic forces, the wall will withstand the forces mainly in a *plastic hinge* (cf. Fig. 1.5). That means that the structural element

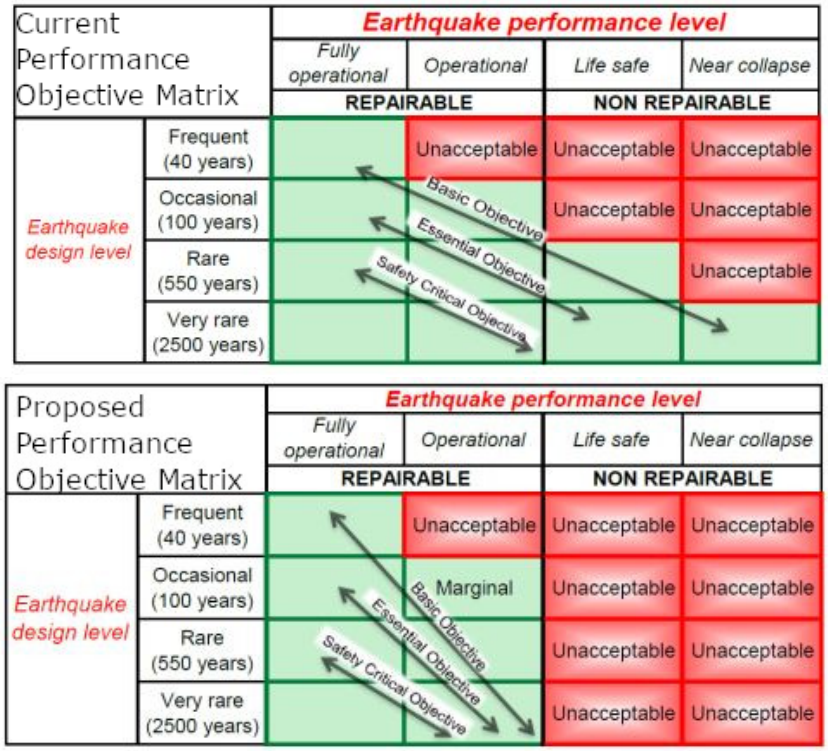


Figure 1.3: Current Performance Objective Matrix (modified from SEAOC, 1995) and Proposed modification to Performance Objective Matrix from Buchanan et al. (2011) [5]

(i.e. wall for this picture but can be beam or column) deforms mainly at the plastic hinge, cracks and big efforts are localised in this part, and it becomes a mechanism. So, all the residual deformations will be caused by the behaviour of the plastic hinge. It is important to find new solutions or implement better structural technologies to decrease the residual displacements in order for the buildings to remain operational. Shape memory alloys (such as NiTinol) can be one of these structural technologies due to their ability to recover large deformations upon removal of stress. The idea is to have inelastic deformation recovery of the structural elements in order to stay at a serviceable state after an earthquake and limit the amount of repair to provide. Due to the cost of the NiTinol, it's not economically viable to put NiTinol for all the reinforcement rebars. A good understanding of the behaviour of RC structures can lead to great improvements, such as putting these rebars in the plastic hinge.

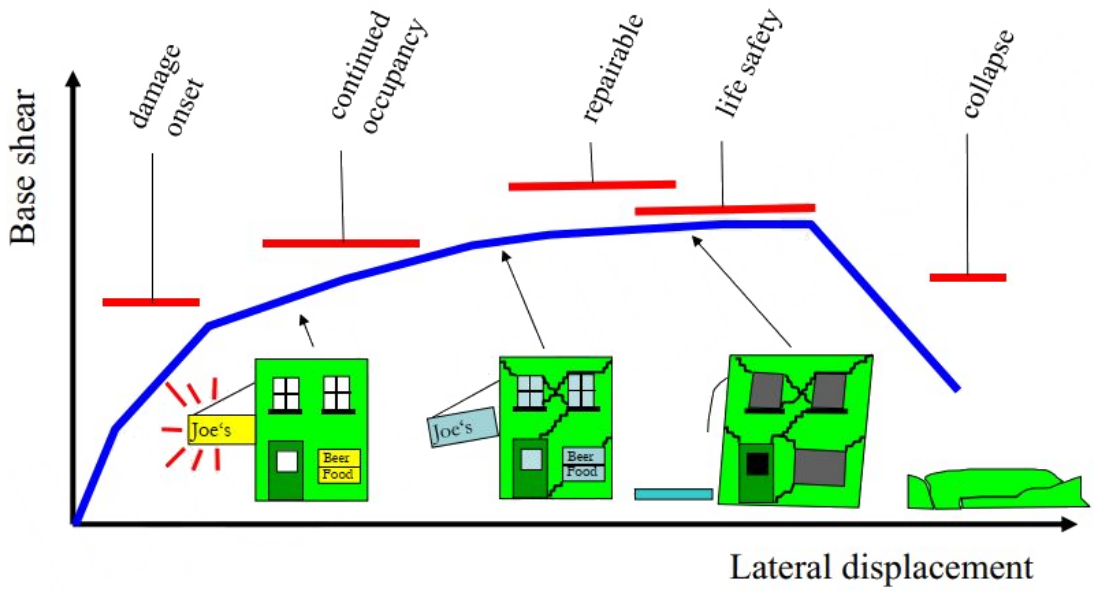


Figure 1.4: Damage state of a building from Pr. Almeida course [6]

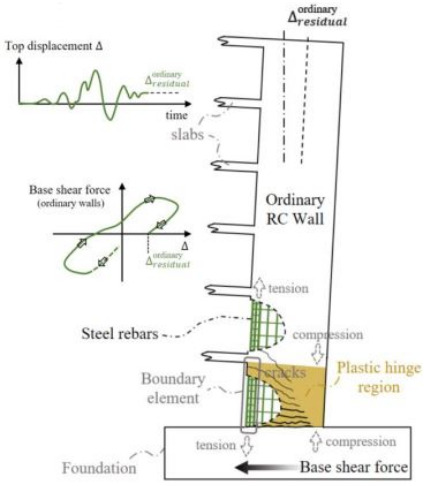


Figure 1.5: Residual displacements in ordinary reinforced concrete walls from earthquake ground motions [7]

1.2 Objectives

The objectives of this master thesis are:

Performance objective	Damage state	Inter-story drift	Residual drift level
Fully operational	No damage	$< 0.2\%$	$< 0.002\,rad$
Operational	Repairable	$< 0.5\%$	$< 0.005\,rad$
Life safe	Irreparable	$< 1.5\%$	$< 0.015\,rad$
Near collapse	Severe	$< 2.5\%$	$< 0.025\,rad$
Collapse	-	$> 2.5\%$	$> 0.025\,rad$

Table 1.1: Performance objectives corresponding to damage states and inter-story drift. Adapted from Hoult [7]

- To determine the recovered displacement as a function of in-plane displacement or drift of beams reinforced with SMA in the plastic hinge area. In order to do this, new experimental tests of SMA reinforced beams will be presented. The first beam will be studied with only steel reinforcement, as a control specimen (called S1), and two other beams will be tested with SMA in the plastic hinge region (called N1 and N2).

- To present new experimental tests on RC beams reinforced with SMA in the plastic hinge region in the literature, one beam will be tested at quasi-static rate (0.25mm/s), and the other at a rate of 5 mm/s, to simulate an earthquake to see the effect of the loading rate on the response of the beams.

- To study a new type of connection between steel rebar and SMA rebar, not a mechanical coupler as used in all the other studies but a welded connection. This will ensure no slippage at the anchorage.

- To calibrate and validate numerical simulations made with a state-of-the-art finite element modelling software thanks to the experimental results.

1.3 Organisation

This manuscript is structured as follows:

1. It starts with a literature review about the SMA (Shape Memory Alloys), the experimental tests already done in the literature and the loading rate effect in Chapter 2.

2. Then, in Chapter 3, the author provides explanations about the finite element method, and the finite element models used.

3. Afterwards, in Chapter 4, the experimental tests, the material properties, the set-up, the loading protocol, and the instrumentation used to measure are described.

4. In the following Chapter, are shown the results of the numerical models, and of the experimental tests in terms of load-displacement response, strains, cracks and recovered displacements.

5. Finally, the last Chapter includes a comparison between the results of the experimental tests and the numerical models and discusses it. Then the author concludes this master thesis.

CHAPTER

2

STATE OF THE ART

The Shape memory alloys (SMA) are used in a lot of domains (e.g. robotics, automotive, medicine, telecommunication, civil engineering,...).
Here is a list of examples of applications in different domains [8]:

- Biomedical Application – Fixation of a frontozygomatic fracture with a shape-memory staple
- Automotive Applications – EAGLE (Electrically Actuated antiglare rear-view mirror)
- Aerospace Application – Boeing's variable geometry chevron
- Robotic Application – Prosthetic hand
- ...

In what follows, attention will be paid to civil engineering applications only.
In 1932, Arne Ölander discovered the pseudoelastic behaviour of the Au-Cd, the first SMA. No use of the Ölander'discovery was made until 1962 and the discovery of the shape memory effect in a Nickel-Titanium (NiTi) alloy, by the United States Naval Ordnance Laboratory (hence comes from the name Nitinol for Nickel-Titanium alloys: "NiTi" for the chemical composition and "nol" for *Naval Ordnance Laboratory*). Commercial uses have been developed in medicine, electronics, and

other engineering fields. Civil engineering applications began in the late 20th century with an increase in studies and research in the last five years.

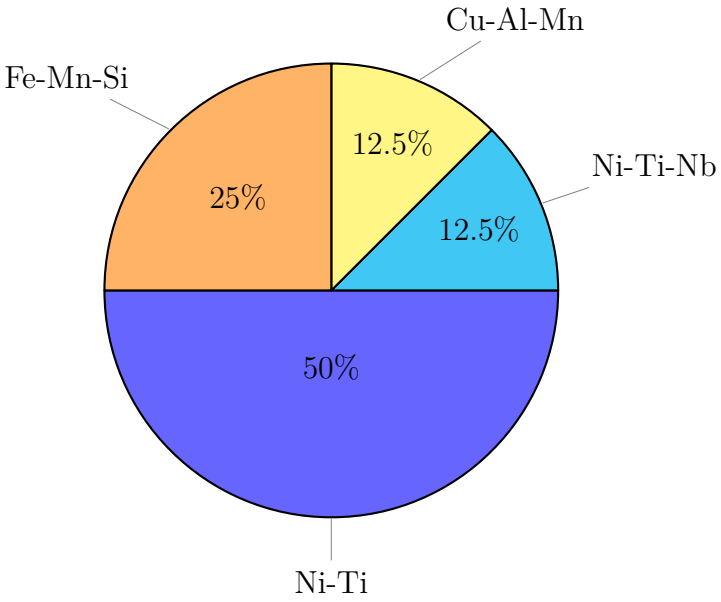
2.1 Shape Memory Alloys

Shape memory alloy is a subclass of smart material. The alloy returns to its original form when subjected to temperature variations or removal of stress. A SMA has two main effects: shape memory effect and superelastic behaviour. Several alloys have these two characteristics.
In previous studies, four main types of SMA have been considered [9]:

- Ni-Ti
- Ni-Ti-Nb
- Cu-Al-Mn
- Fe-Mn-Si

Nickel-Titanium alloy (NiTi) is the most common type of superelastic SMA in civil engineering applications because they are commercially available and used in other fields. It is an equiatomic compound of Nickel and Titanium, it is corrosion-resistant and thermally stable.

According to Raza et al. [9], the distribution of the SMA types in the past studies:



To compare these four types of SMA, the main material and thermomechanical properties are summarised in table 2.1.

Type of SMA	Elastic Modulus GPa	Yield Stress MPa	Failure Strain %	Optimum Prestrain %	Activation Temperature °C	Recovery Stress MPa	Recovery Strain %
Ni-Ti	38-84	379-746	40-50	6-8	100-200	400-700	6-9
Ni-Ti-Nb	25-63	232-350	9-37	6-7	108-200	354-560	5-7
Cu-Al-Mn	20-35	180-210	18	/	/	/	7-12
Fe-Mn-Si	75-165	400-550	40	2-4	160-500	130-580	0.15-4

Table 2.1: Material and mechanical properties of SMAs used for strengthening RC structures from [9].

2.1.1 Austenite and Martensite

Austenite and Martensite are two distinct phases that occur during the lifetime of a SMA, each one has specific properties.
The austenite phase (A-phase) has a symmetric crystalline structure and is typically stable at high temperatures and low stresses. On the contrary, the martensite phase (M-phase) has a low-symmetry lattice structure and is typically stable at low temperatures and high stresses.
The two important effects of SMA occur each in one phase. The Shape Memory Effect (SME) occurs during the martensitic phase, and the SuperElasticity (SE) occurs during the austenitic phase.

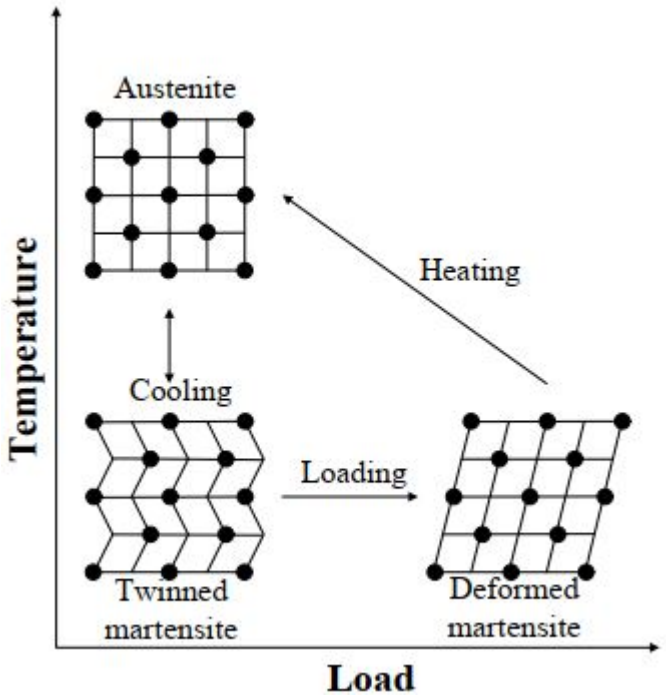


Figure 2.1: SMA phases at different temperatures and loads [10]

The graph in Fig. 2.2 explains well the phase transformation due to the temperature. Four temperatures are known to define a shape memory alloy:

- M_s: Martensite start temperature
- M_f: Martensite finish temperature
- A_s: Austenite start temperature
- A_f: Austenite finish temperature

Below M_f, the alloy is fully in the martensite phase, when heated, the SMA structure starts to transform into austenite at A_s, and is fully in the austenite phase above A_f. During cooling, when the temperature decreases below M_s, the alloy returns to the martensite phase and is totally in the martensite phase beneath M_f.

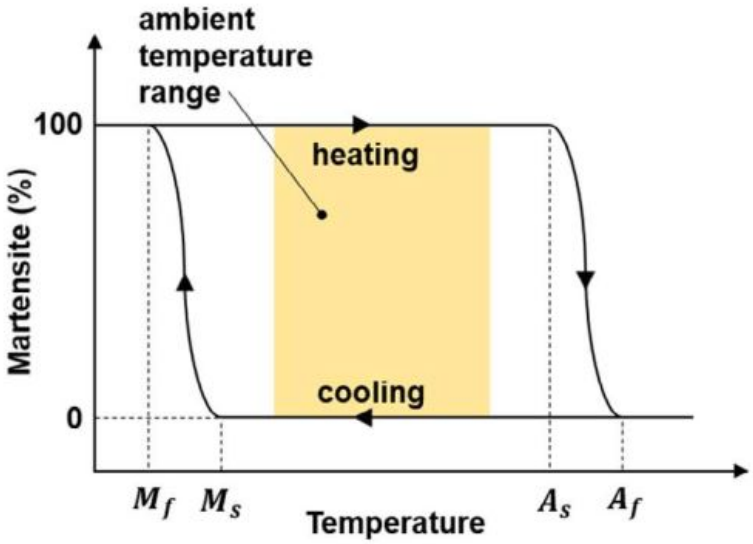


Figure 2.2: Thermomechanical properties of SMA: thermal hysteresis [11]

2.1.2 Shape memory effect and Superelasticity

The shape memory effect is the ability for a deformed SMA to return to its original position after heating as sketched in Fig 2.3a). It occurs during the martensitic phase.

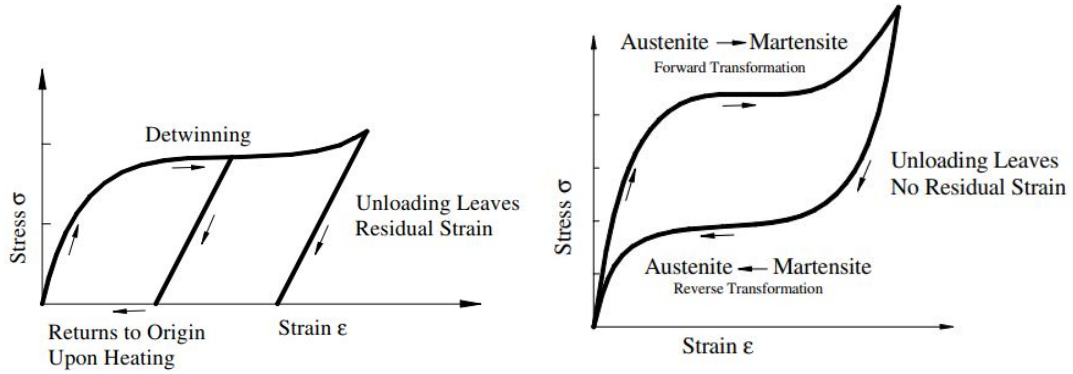


Figure 2.3: Idealised stress-strain curve for a) shape memory effect and (b) superelasticity effect [12]

Superelasticity is a typical feature of Austenite SMAs, it is the ability to recover large strains after the removal of stress as sketched in Fig 2.3b).
In summary, a SMA in the Austenite phase will fully recover residual deformations through unloading of mechanical stress, while heat is required to recover residual deformations when the alloy is predominantly in the Martensite phase [10]. Figure 2.4 shows a 3D representation (Stress, Strain and Temperature) of the behaviour of a SMA.

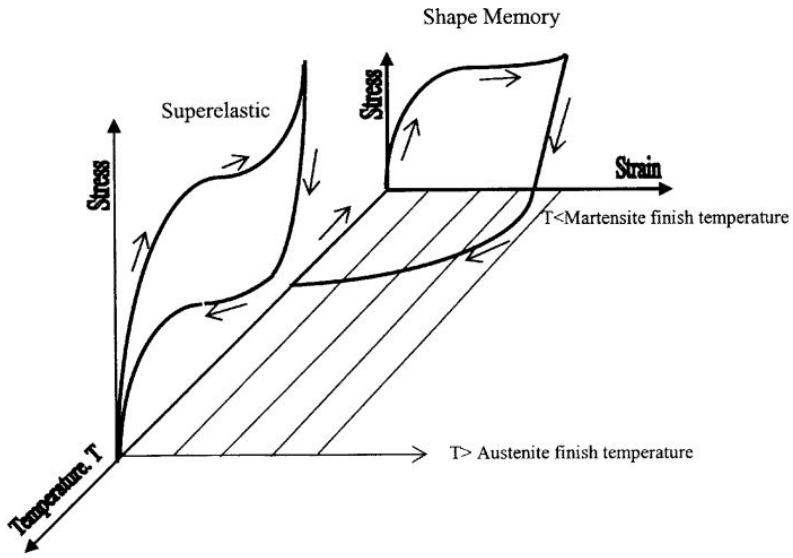


Figure 2.4: Three-dimensional stress-strain temperature diagram showing superelastic and shape memory behaviour of NiTi alloy [13]

2.1.3 Applications for civil engineering structures

Shape memory alloys possess several properties (SE and SME) that make them useful for seismic applications, and they have been used for over 20 years.
The following paragraphs explain the first uses of SMA in building renovation.

Bell tower of the Church of San Giorgio at Trignano, Italy (1999) [14, 15]:

It's a renovation project after the 1996 earthquake, (magnitude 4.8, intensity VII), the Bell tower had a lot of damage. After the earthquake, the tower was renovated with SMA devices. Four steel rebars with SMA devices were placed on the four inner corners of the monument to increase its bending and shear resistance. Each SMA device was manufactured with 60 Ni-Ti superelastic wires (diameter 1 mm and length 300 mm). The combined devices were anchored to the top and to the foundation of the tower and then post-tensioned with a force of 20 kN (total force of 80 kN) in order to apply a compressive stress distribution to the masonry and to keep the applied force constant. This renovation site was considered the first worldwide application of this innovative intelligent material as seismic design and retrofit on a historic masonry tower. In June 2000, an earthquake of Richter magnitude 4.5 occurs at the same epicentre as the event of 1996. After the main shock, the bell tower was investigated and no damage was found.

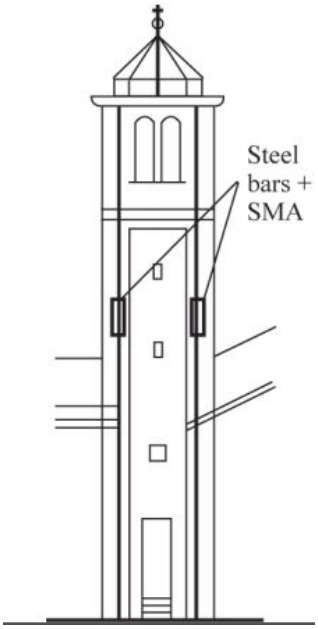


Figure 2.5: Location of the retrofitting [14]

Retrofitting of the Basilica of San Francesco at Assisi, Italy (2000)[16]:

The main RC beams of the roof structure were supported by the tympanum walls of the San Francesco Basilica at Assisi. But this system doesn't allow any control of the force that can be transmitted during seismic events to the tympanums.
An earthquake occurred in 1997 and damaged the Basilica of San Francesco at Assisi, the south tympanum masonry wall collapsed, vertical cracks opened and amplified by previous seismic events were largely reopened and needed protection to avoid excessive crack openings. Engineers had to find structural solutions to protect

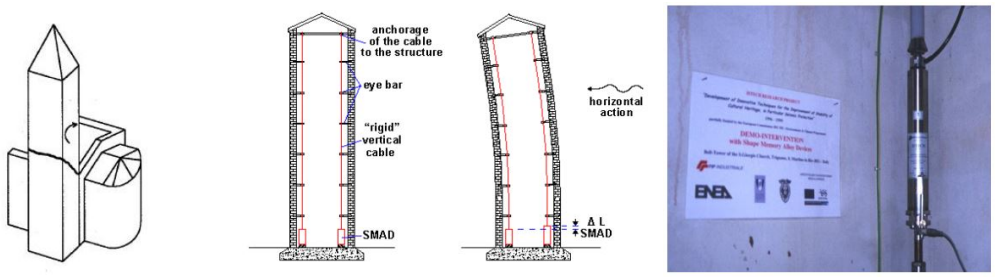


Figure 2.6: (a) Flexural collapse of a bell tower, (b) Proposal of use of SMA devices on slender buildings, (c) SMA devices application in the Trignano Bell-Tower [15]

the tympanum walls and avoid excessive cracks. Classical steel was not a good idea due to the stiffness of the steel, forces would have been directly transmitted to the tympanum wall and could have caused further damage.
Shape Memory Alloy Devices were installed spaced 50cm apart to better distribute the forces moreover the roof structure and the tympanum walls were disconnected.



Figure 2.7: The transept tympanum of the S. Francesco Basilica in Assisi: (a) damaged and (b) restored, (c) by the insertion of SMA Devices [15]

Repair of a cracked region of a highway bridge in Michigan, USA (2001)[12]:

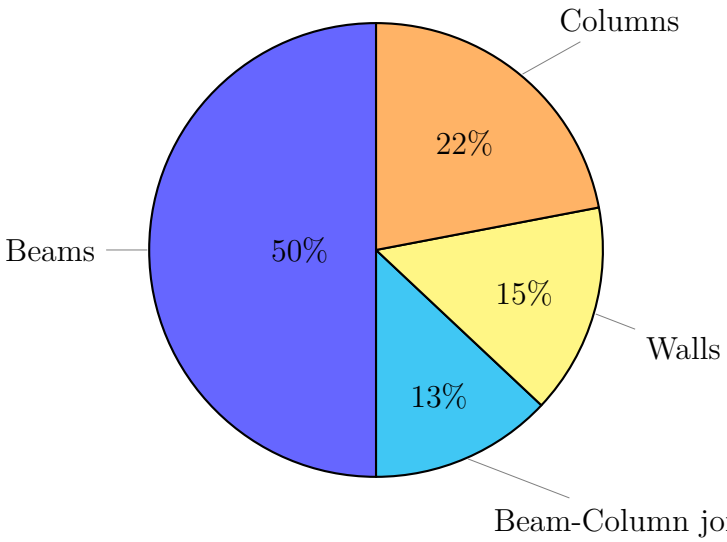
This reparation was the first use of SMA (FeMnSiCr) in post-tensioning of a concrete structure to reduce the crack widths. The T-beam of the bridge had an average crack width of 0.55mm. SMA rods (10.4mm diameter) were placed at both faces of the web and heated by an electrical current up to 300°C, the residual stress after cooling down was 120 MPa and the crack width decreased by 40%. Additional examples of bridge repairs or new bridge constructions with SMA are available in [17].

2.2 Experimental tests with shape memory alloys

In this section, the author will analyse structural elements already studied with experimental tests in the literature. The following chart indicates the distribution of the experimental tests already performed divided into four categories.

- Beams
- Columns
- Walls
- Beam-column joints

The number of studies about SMA as structural reinforcement is limited because the subject is still new (first experimental test in 2001 [18]) and costly.



Distribution of the experimental studies sorted by the type of structural component. Adapted from Raza et al. [9].

All the papers that will be cited in the next pages, to the author's knowledge, use a mechanical coupler to connect the steel and the SMA rebars. This system has disadvantages, the main one is that it can lead to structural failure due to a bad connection between the two rebars. Indeed, the coupler is not able to limit the displacement (local slipping) between two rebars when subjected to large stresses. Welding SMA rebar is very difficult because it can lead to brittle failure around the heated zone as mentioned by Desroches and Smith [19]. Different welding techniques are detailed by Akselen [20] with attention to the type of joints and the brittleness. But with a good knowledge of the microscopic composition and of the process of welding, a good connection can be made as studied and experimentally tested by Lezaack et al. [21]. More details on the process used for the welding

between SMA and steel for this master thesis are available in section 4.5.
Figure 2.8 is an example of one mechanical coupler used in a wall by Almeida et al. [22], and in Fig. 2.9, one threaded coupler used in a beam by Abdulridha [10]. Additional information about mechanical couplers and tests performed on them can be found in Alam et al. [23].

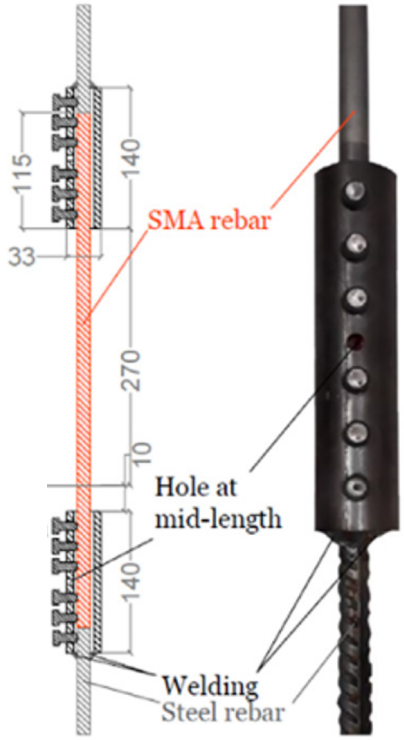


Figure 2.8: Mechanical coupler [22]



Figure 2.9: Threaded Coupler [10]

For the next subsections, the studies with experimental tests and the main features are presented by categories in chronological order.

2.2.1 Beams

Due to the subject of this thesis and the experimental tests done in the lab, the author will mainly focus on the experimental tests on beams. Furthermore, half of the tests already done in the literature are on beams as explained before.
Beams are very often used in the construction of buildings, bridges,... Furthermore, small-scale specimens can easily be studied, which reduces the cost of the experiment by reducing the amount of SMA reinforcing bars.

The first experimental tests were conducted by Soroushian et al. [18] in 2001. The experimental tests consisted of using external post-tensioned SMA rods to repair and strengthen damaged RC beams. The results showed that after shear cracking, SMA post-tensioning, and heated up to 300°C, can provide a load-capacity almost equivalent to the original.
Deng et al. [24] investigated the effect of SMA wires heated and prestressed for the control of beam's deflection. They made a parametric study, varying the area of the SMA wires, the cross section of the RC beam, the prestress force,... They concluded that SMA can recover large deformations of the RC beam, and have found factors influencing the recovery force of the RC beam (i.e. prestrain, diameter of the wires and actuation mode of the SMA) and factors that need more studies (i.e. specimen curing condition, curing age and actuating times).
Eight RC beams were tested at quasi-static rate under cyclic loading by Saiidi et al. [13] as represented in Fig. 2.10. The variables of the tests were the type (4 with steel vs 4 with NiTi) and the amount of reinforcement in the critical region (midspan). The experimental results showed that the residual displacements of the NiTi RC beams were smaller than 1/5 of the residual displacements of the control reinforced beams. They also noticed that the stiffness of NiTi RC beams was 60% lower than the stiffness of control RC beams. They concluded their paper by proposing a beam with both steel and NiTi as reinforcement to have an acceptable stiffness and the capability to recover deformations.

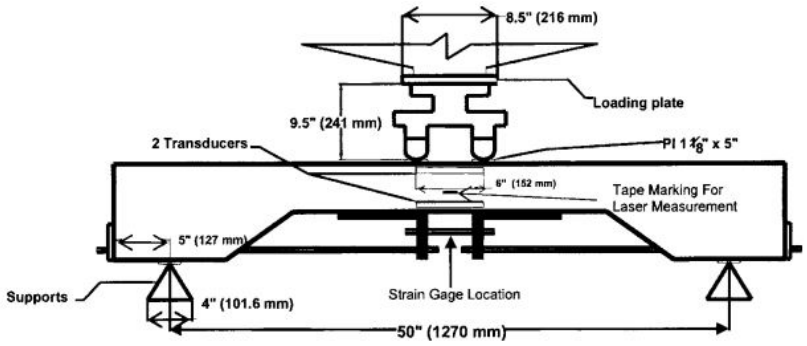


Figure 2.10: Beam test setup [13]

Li et al. [25] investigated the repair of RC beams, by strengthening of RC beams by temporary SMA wires in addition to perpetual CFRP (Carbon Fibre Reinforced Polymer). Four specimens were tested. The results obtained showed that SMA wires can reduce residual displacements of RC beams. The system proposed (short-term strengthening by SMA wires and permanent strengthening with CRFP plates) is validated to strengthen RC structures.
RC beams that repair by themselves were proposed by Kuang and Ou [26], using

NiTi wires and brittle fibres with adhesives. The system works as follows: when deformed, the brittle fibres break, the adhesives are released in the breach to decrease the crack width while the SMA by their properties will recover the deformation of the beam. Tested under static loading, after large deformation (2% of the span length), cracks were nearly closed.
Abdulridha et al. [27] tested seven beams under monotonic, cyclic and reverse cyclic loading using four-point bending setup (cf. Fig 2.11). They compared the experimental results obtained by testing three control specimens, with only steel reinforcement, and four beams with 600mm of SMA (NiTi) centred at mid-span. The results obtained indicate that SMA beams can recover larger deformations than the control beams, 85% and 26% recovery of mid-span displacements respectively. A better crack recovery was observed for the SMA beams while similar strength capacity and displacement ductility were noticed. A numerical simulation was also conducted by the authors using VecTor2 and gave satisfactory results. A part of these numerical results will be used in Chapter 3.

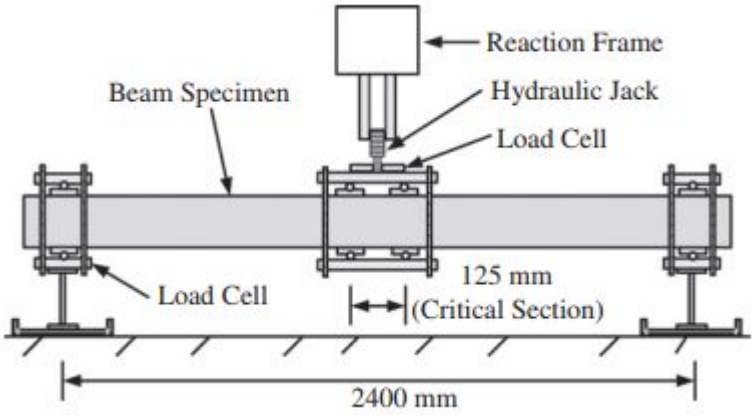


Figure 2.11: Test set up [27]

Shrestha et al. [28] tested one 1/3 scaled steel RC beam under cyclic loading in terms of crack recovery and two with 150mm long Cu–Al–Mn SMA rebars as longitudinal upper and lower reinforcements in the middle of the beam (with and without pretensioning). They found that SMA beams can recover larger cracks opening than steel RC beams. For one equal angular deformation, the steel RC beam recovered 0.5mm of crack width after a crack opening of 6mm while the SMA beams recovered 4.7 mm and 4.4 mm from the crack opening of 5 mm without prestressing and 6 mm with prestressing respectively.
A study by Zafar et al. [29] focused on the use of SMA-FRP (Shape Memory Alloy - Fibre Reinforced Polymer) to increase the recentering capability. Flexural tests done on one T-beam under quasi-static cyclic loading (tension and compression)

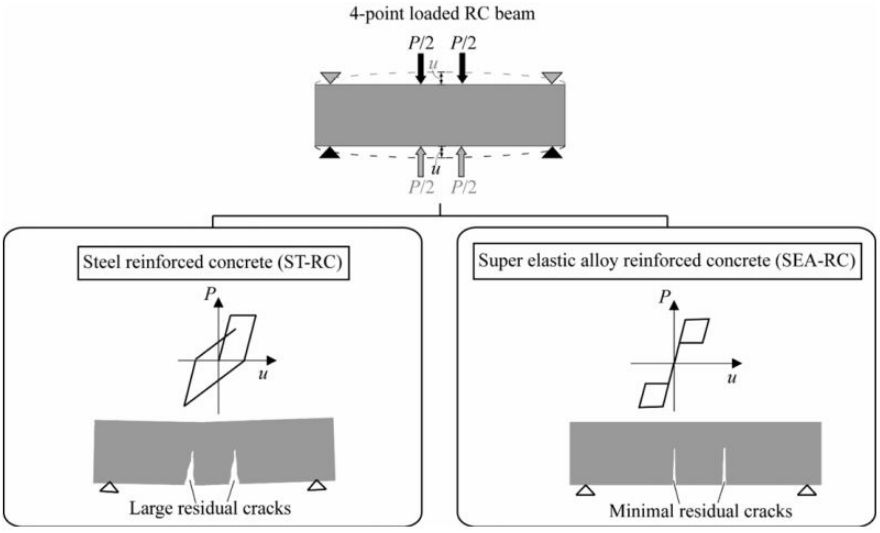


Figure 2.12: Expected features of RC beams based on hysteresis of reinforcement [28]

indicates that the SMA-FRP reduces the crack width by 96% due to its recentering capacity. Results also show better performance of SMA composite rebars in terms of ductility, energy dissipation, recentering to recover residual deflections, without permanent damage to the reinforcement.
The ability of an externally activated self-repairing system with epoxy and SEA (Super Elastic Alloy) to repair RC beams is studied by Pareek et al. [30]. They tested three 1/3 scale beams, with a three-point cyclic loading. First beam with classical steel deformed rebar, the second one with threaded rebars and the last one with SEA (Cu-Al-Mn) threaded rebars. Cracks of 0.5mm were observed in all specimens but due to its recentering capacity, the self-repairing system proved successful for the SEA specimen. This technique is effective for rotation up to 1/40 rad for SEA beams, much higher rotation than the 2 first beams.
Shahverdi et al. studied the flexural behaviour of RC beams with prestressed Iron based SMA strips [31] and the use of ribbed Fe-SMA in shotcrete layer to strengthen RC structure [32]. In the first study, after have tested six RC beams with four-point bending (one control beam, one Fe-SMA reinforcement without prestressing, three Fe-SMA reinforcement with prestressing, and the last one with CFRP strips) to see the feasibility of strengthening with prestressed Fe-SMA strips, they concluded that the technique works well, the beams with prestressed strips have an average cracking load 80% higher and 75% less displacement for a load of 8kN than beam with Fe-SMA wires without prestressing.
For the second study, where they tested four beams (one beam without any strengthening used as a reference beam, one strengthened by two normal steel ribbed

bars, one strengthened by two ribbed Fe-SMA bars and the last one strengthened by four ribbed Fe-SMA bars) in order to demonstrate the application of the strengthening method. The conclusions are that, in comparison with a reference beam, at 4mm displacement at mid-span, beams with 2 steel, 2 Fe-SMA and 4 Fe-SMA, the applied load increased by 95%, 163% and 265% respectively. The cracking load was also increasing, the control beam cracking load was 5.4kN while for the beam with 2 prestressed Fe-SMA bars it was 9.5kN.
The use of NiTi as shear reinforcement was studied by Mas et al. [33], the objective of the study was to see if it was possible to have ductile shear failure. They tested seven small-scale RC beams changing shear reinforcement's spacing, angle or material (Steel or NiTi). Results indicate that it's possible to obtain ductile shear failure with SMA shear reinforcement. For 3 on 4 NiTi beams, the ductility factor is greater than 5, while the ductility of steel RC beams is around 1. All the beams were designed to fail in shear.
Nubailah et al. [34] analysed the ability of SMA to recover permanent deformations. They tested 2 small-scale RC beams, one control and one with SMA at mid-span (cf. Fig. 2.13) under monotonic loading. The results obtained confirm that SMA beams residual displacement and residual cracks were smaller than for the control beam.

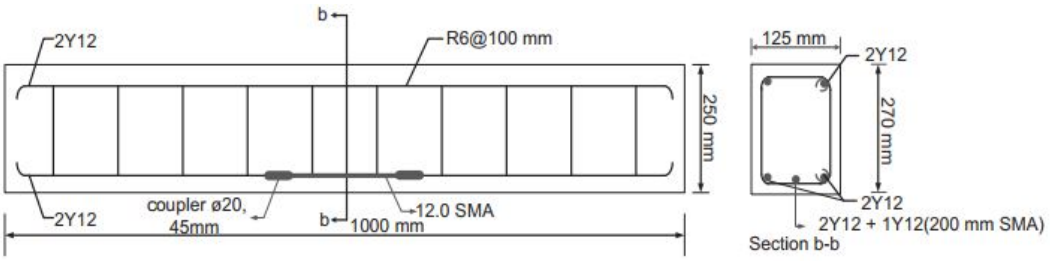


Figure 2.13: Treated beam [34]

In 2017-2018, Rojob and El-Hacha published 3 papers on experimental tests with Iron-based SMA, the first one [35] is dedicated to the study of flexural self-strengthening with prestressed Fe-SMA rebars (not by hydraulic jack but by heating of the rebars) of RC beams. Experimental results showed that the technique used is efficient to increase the flexural capacity at SLS and ULS and the ductility. On the three tested beams (one control and 2 with SMA), the ductility index for beams B-SMA-1 and B-SMA-0 increased by 33% and 41% over the control beam and the ultimate load of beams B-SMA-0 and B-SMA-1 was 33% and 36% more than the control beam, respectively.
The second one [36] speaks about the strengthening of RC beams with near-surface-mounted self-prestressed iron-based SMA strips. They tested four beams under

four-point bending monotonically up to failure (1 control beam and 3 strengthened beams with Fe-SMA). They concluded that the prestressed Fe-SMA strips improved the flexural behaviour at SLS and ULS and the ductility of SMA beams 1 and 2 were 71% and 90% bigger than similar CFRP beams from another study.
The third paper [37] investigates the fatigue performance of RC beams with pre-stressed Fe-SMA strips. Four beams (two batches of two beams, one control beam and one strengthened beam) were tested, the first batch was subjected to 6 million cycles at 3Hz in three loading stages. During low levels of fatigue, the SMA beams showed better behaviour than the control beam. But at higher stress levels, the bond between SMA and concrete caused degradation and stress concentration at the anchor. The SMA bar failed at the anchor location at 5.5 million cycles.
Pareek et al. [38] explored the use of SMA bars (Cu-Al-Mn) to shift the plastic hinge of RC beams by moving the SMA bars away from the beam end. Four beams represented in Fig. 2.14 were tested under cyclic loading, one control beam and three beams with 100mm SMA reinforcement at different locations as shown in the figure. Experimental results showed that the alloy can reduce the residual displacements, and are approximately on the SMA beam one-third of the control RC beam.

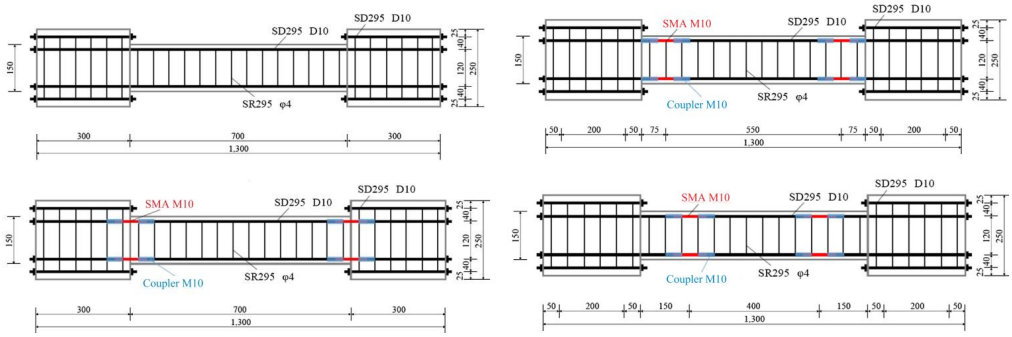


Figure 2.14: Elevation of tested beams: SD, SMA(0D), SMA(0.5D), and SMA(1.0D) [38].

Seven RC beams were tested to evaluate the flexural behaviour of strengthened beams with SMA strips activated by heating by Hong et al. [39], varying the numbers and the type of strips and the level of prestress. It has been shown that the ultimate load increased with the prestress level and the cracking load of RC beams strengthened with prestressed SMA strip (SL-60S-2 and SL-60S-4), increased by 15.89 and 35.41% in comparison with non-activated Fe-SMA RC beam.
Michels et al. [40] analysed the feasibility of a flexural strengthening method for RC beams with Fe-SMA strips. To do so, they tested four beams under static loading with four-point bending, as sketched in Fig. 2.15, (including a control RC beam) varying the strengthening type (with CFRP or SMA strips) and the

prestress (activated by resistive heating of the SMA). They concluded that the 3 strengthened beams had smaller deflection for a given load and greater ductility than the control RC beam. The presented technique proved to be efficient.

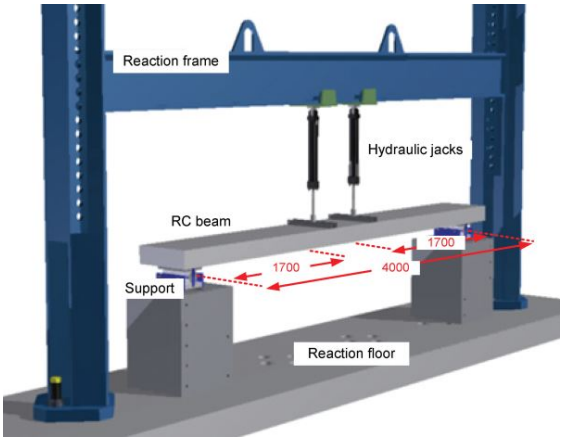


Figure 2.15: Setup for the static loading tests [40]

An external shear strengthening of RC beams with Fe-SMA strips activated by a heating method is experimentally validated by Montoya-Coronado et al [41]. Experimental tests were done on 10 small-scale beams, two control RC beams and 8 with different strip widths and activated or not Fe-SMA. Results showed that the failure mode changed from a shear failure for the control beams to a flexural failure for 25mm strips strengthened beams, showing high ductility. The load capacity increased with this strengthening method (83% and 65% bigger load capacity for one beam strengthened with 25mm strips and with 12.5mm strips respectively, in comparison with the control beam). When SMA strips are activated, the SMA beams have smaller deflections and fewer shear cracks.
Strieder et al. [42] studied the behaviour of strengthened RC beams with external Fe-SMA activated by infrared heating. Four beams were tested under four-point bending, two with SMA strips prestressed by heating, one with steel strengthening and the last one is a control beam without strengthening. The SMA prestressed strips increased the ultimate load by 160% and the first cracking load by 320%. The global behaviour of strengthened RC beams improved in comparison with the control beam.
Rius et al. [43] investigated the effectiveness of a shear strengthening method for RC beams with external Ni-Ti-Nb wires around the beam as represented in Fig. 2.16. Small-scale beams were tested up to shear failure (designed at this purpose) and proved the efficiency of the technique (concrete confinement and transversal prestress). A shear strength increase of about 90% and 115% of the retrofitted beams in different arrangements and a ductility increase in comparison with control

beams were noticed.

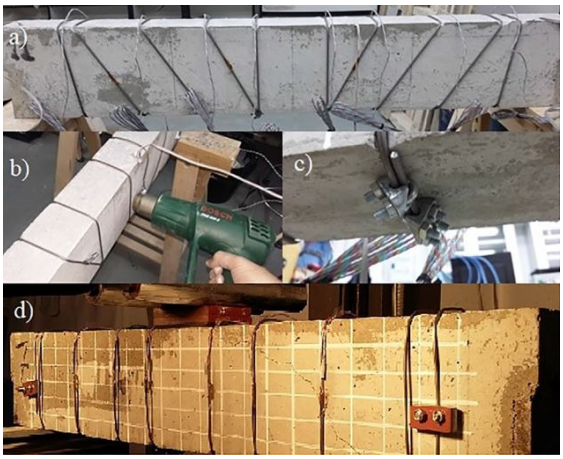


Figure 2.16: (a) Rear view of a strengthened beam, (b) activation process by means of a heat gun, (c) detail of the anchoring using U-Bolt saddle clamps, and (d) front view of a beam with left and right outermost wire anchors [43]

Sinha et al. [44] proposed a post-tensioning system with heat activated NiTiNb wires to repair RC beams based on the ability of SMA to recover deformation under heating. They tested 4 beams under four-point bending up to failure, one control beam and three others with different SMA quantities. The post tensioning method improved the behaviour of the beam, the ultimate moment capacity increased by 45% while the residual displacement at mid-span decreased by 49%.
Cladera et al. [45] tested 8 real scale RC beams to study the shear strengthening of RC beam T-shaped with external Fe-SMA strips, 2 control beams, and the others with various combinations of SMA shear strengthening. The beams were loaded under a three-point bending and were designed to fail in shear. The strengthening technique showed an increase of about 30% of the shear capacity in comparison with control beams. The activation of SMA wires delayed the emergence of cracks in the beams and crack width decreased.
To determine the displacement recovery of RC beams under four-point bending cyclic loading, Azadpour and Maghsoudi [46], experimental tests on 8 RC beams were done with two types of concrete (normal and high strength), different reinforcement ratios and strengthened or not by SMA strands. Beams were tested cyclically up to failure. Beams with SMA strands were able to recover 50% of cracks before failure, the curvature of these beams was greater than the control one's curvature, showing a better ductility behaviour of SMA RC beams than control RC beams.
Czaderski et al. [47] investigated the SMA U-shaped shear reinforcement for bridge girders. Six beams were tested, a control one (B1), 2 lots of 2 beams with the same amount of stirrups (B2 and B3: 3 stirrups; B5 and B6: 5 stirrups), one activated

by electrical heating, the other not, and the control beam was repaired and retested (B4). The effects of prestress and SMA strengthening are compared. Beams failed in shear but the shear capacity of beams with SMA stirrups increased more than 170% while the midspan displacement, crack width and beam deflection decreased. The technique is validated because of the global improvement of the behaviour of the tested RC beams.

2.2.2 Walls

Walls are a very important structural part of a building because they have big horizontal inertia and are widely used to withstand horizontal/ seismic forces. The lateral forces are dissipated in the plastic hinge region of the shear walls, which leads to permanent damage in this region. The goal of SMA in the plastic hinge region of RC walls is to decrease the residual displacement during an earthquake. Also, SMA can help to strengthen RC walls.
The low number of studies of walls with SMA rebars is mainly due to the high cost of SMA rebars and the complexity of the experiment to be performed.

Effendy et al. [48] studied the resistance of RC shear walls under reverse cyclic loading with SMA bars acting as structural bracing systems in order to increase the ductility and the energy dissipation capacity of the walls. The height, width, and thickness of the designed shear walls were 1.0 m, 2.0 m and 0.12 m, respectively. The main parameter used in the study is the type of SMA bars, namely Superelastic (shape recovery upon removal of load) and Martensite (shape recovery through heating) SMA bars. Three walls were tested, the first one only with steel reinforcement, the second one with superelastic SMA bars, and the last one with martensite SMA bars activated at 150°C. The tests conclude that, in comparison with the control specimen, the shear wall with Martensite SMA bars has greater residual displacement. In contrast, the shear wall with Superelastic SMA bars has less residual displacement.
Abdulridha and Palermo [49] investigated the performance of a hybrid SMA-steel RC shear wall (cf. Fig. 2.17). One wall with steel was also tested as reference. The walls were tested under cyclic reverse loading up to failure. The conclusion they have drawn from the experimental tests is that the hybrid wall was more effective to recover residual displacement after being subjected to drift bigger than 4%. The lateral strength and displacement capacities were similar for the two tested walls.
In another study, Cortés-Puentes et al. [50] analysed the response of a repaired RC wall under a reverse cyclic loading using the wall of Abdulridha and Palermo [49], repairing the concrete in the plastic hinge region and substituting the old rebars with new SMA rebars, as sketched in Fig. 2.18. They also used a repaired wall

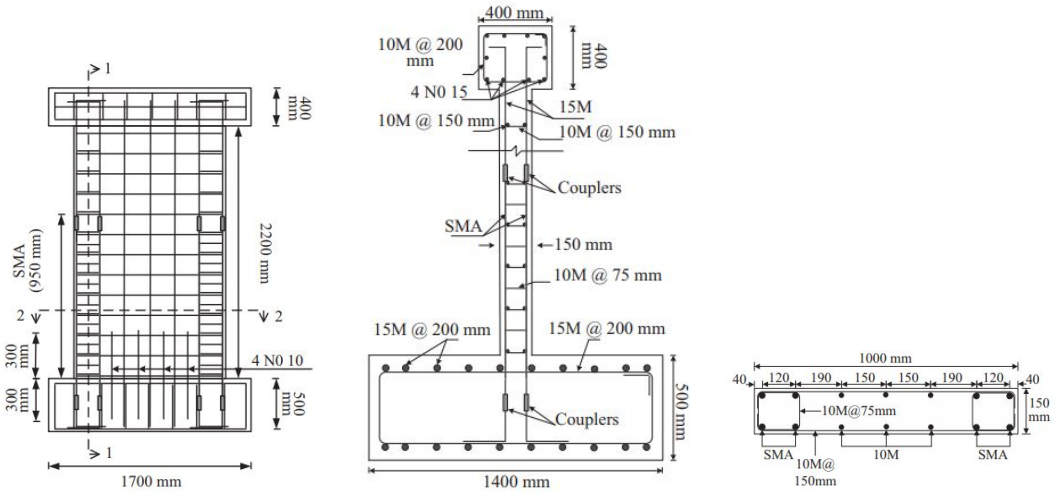


Figure 2.17: Reinforcement Details of Wall W2-NR: (a) Elevation View; (b) Section 1-1; and (c) Section 2-2 [49]

with steel reinforcement to compare. The repaired walls were capable of restoring the yield and ultimate lateral load capacities but sustained lower drift capacities. The repaired SMA wall was capable of recovering the imposed lateral drifts up to 2%. The repaired walls dissipated up to 7.8% more energy than their original walls for a significant portion of the loading range. The length of the SMA bars and the presence of starter bars in the original walls were influencing factors in the location of failure of the SMA- and steel-reinforced walls.

Cortés-Puentes and Palermo [51] studied the effect of a bracing system made of superelastic SMA as retrofitting for seismically deficient RC shear walls. This paper focuses on four one-third-scale RC walls, two control and two retrofitted with the SMA bracing system susceptible to shear sliding and diagonal tension cracking under reversed cyclic loading. The retrofitting device shows good performance in terms of lateral strength capacity, ductility, energy dissipation, and displacement recovery. The first aim of the system was to minimise the damage at the base of the walls.

Yan et al. [52] tested six RC shear walls reinforced with Fe-based SMA, testing the influence of the steel stirrup ratio and SMA reinforcement ratio. The experimental results show that the ratio of the residual force to the maximum force in each cycle, of the SMA-reinforced walls was found to increase by 21.7% compared to that of the conventional shear walls. Yan et al. conclude that the steel stirrup ratio and SMA reinforcement ratio in the edge member have a great influence on the resilient performances of the shear wall structures.

Kian and Noguez [53] tested 4 walls with different reinforcements, one with classic

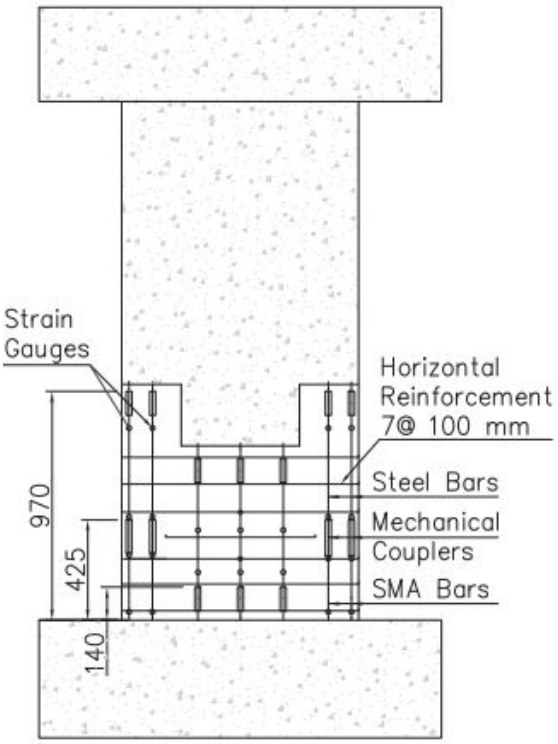


Figure 2.18: Reinforcement layout of RW2-NR [50]

steel, the three others with a hybrid reinforcement system: shape memory alloy bars, glass fibre reinforced polymer bars or high-strength steel strands. The tests were done until failure under pseudo-static cyclic loads. It's stated that the SMA reinforced shear wall exhibited the highest drift capacity among all the specimens tested.
The last experimental study of SMA in walls was conducted by Almeida et al. [22], two 2/3 scaled RC walls were tested under cyclic quasi-static loading in flexure. The first one was designed thanks to Eurocode 8 [4], the second one with the same reinforcement and four SMA rebars in the plastic hinge region. The tests showed a reduction of residual displacements and damage to the second wall.

2.2.3 Columns

Columns are generally used in buildings because they are easy to build and install on site, they can withstand all the vertical forces, but if one column collapses, it can lead to a total collapse of a building. Columns can be used for buildings, bridges,... but don't resist well to seismic action.
SMA can be used to increase the active confinement (cf. Fig. 2.19) of the concrete using prestrained SMA spirals as in the paper of Jung [11] represented in Fig. 2.21 or as main reinforcement in the plastic hinge region to achieve self-centring behaviour as studied by Nakashoji [54] in Fig. 2.20. Small-scale specimens can be studied, which can lead to reducing the costs of the experiment by a decrease in the amount of SMA rebars needed.

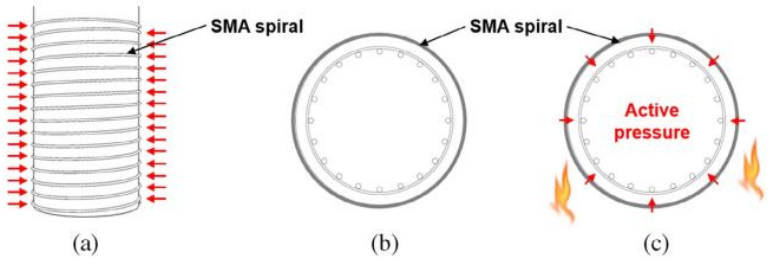


Figure 2.19: Application of active confinement using SMA spirals: (a) prestrained SMA spirals wrapped around the plastic hinge zone, (b) cross section before heating and (c) cross section after heating [11]

The first experimental tests done on columns with SMA were conducted by Saiidi and Wang [55] in 2006. They put SMA as reinforcement in the plastic hinge area of one column, and compare the response of the column with a control specimen (only steel reinforcement) on a shake table with a focus on residual displacements. They also analysed the effect of repair with engineered cementitious concrete (ECC).

Results show that most of the plastic deformations were recovered for the SMA reinforced column and that the use of ECC reduced the concrete damage.
Saiidi et al. [56] tested three columns, the first with steel reinforcement and conventional concrete, the second with SMA rebars in the plastic hinge region and conventional concrete and the last with SMA in the plastic hinge region and ECC, under slow cyclic loading until failure. From the experimental results, they concluded that the third column had least damage and a higher drift capacity in comparison with the others.
Shin and Andrawes wrote two papers on SMA on columns. In the first one [57], they studied the feasibility of column repair with SMA spirals to apply active confinement pressure on the damaged zone of the column. This repair technique is successful, the initial stiffness, strength and ductility were regained due to the active pressure.
Their second study [58] focused on an innovative active confinement technique to improve lateral behaviour. They built four 1/3 scale models and tested them under quasi-static lateral cyclic loading, without confinement technique for the first and three different methods for the three other columns. The SMA active confinement showed benefits such as an increase in the ductility capacity, a higher ability to mitigate the damage under high drift ratios and a higher energy dissipation than the other columns.
Noguez and Saiidi [59] constructed and tested on a shake table a 1/4 scale bridge with three pairs of columns, with three different details at the bottom plastic hinge, one with SMA rod in the plastic hinge region and ECC, one with post-tensioning tendons and the last one with elastomeric pads. They conclude that the residual displacements were minimal with the SMA rods, the damages were also reduced on the SMA/ECC bridge pier in comparison with the others.
Choi et al. [60] compared two types of SMA, NiTi and NitiNb wires in terms of mechanical behaviour and studied the effect of each alloy when applied to a RC column. Three pairs of 3/5 scale columns were studied and tested under cyclic loading. The varying parameters were the lap slice and the type of SMA wire used (NiTi or NiTiNb) to retrofit the column. They concluded that the SMA wires have risen the ductility of RC columns, and that NiTiNb wires had larger residual stress than NiTi wires, significant factor for the active confinement of RC columns. However, the article advises the use of NiTiNb because the temperature hysteresis is larger when prestrained than NiTi, which makes them applicable to a larger range of civil applications.
Nakashoji did a thesis under the supervision of Dr. Saiidi on the seismic performance of RC columns reinforced with SMA [54]. He tested three 0.3-scale bridge piers under cyclic loading, the first one with conventional steel and conventional concrete and two with different lengths of SMA at the plastic hinge analysis and ECC

for all the height of the column (cf. Fig 2.20). The drift ratio was 85% lower for the columns reinforced with SMA than the conventional one. The residual displacements decreased because steel dissipates energy by permanent deformations while the SMA has a flagged hysteresis curve. The overall performance of RC columns with the smart materials was improved (better resilience, higher drift capacity and less residual displacements).



Figure 2.20: SR99-SSE Hinge Area without Corner Bars [54]

Hosseini et al. [61] studied the performance of six columns under seismic loading with or without Cu-Al-Mn superelastic alloy in the plastic hinge analysis. In comparison with the control specimen, if the steel is totally replaced by the alloy rebars or partially replaced, a decrease of 91% and 33% of the residual displacements is measured, respectively. On the other side, the RC column had a greater lateral force capacity and bigger stiffness than the SMA columns.
Tazarv and Saiidi [62] proposed a design to minimize the seismic damage of RC precast pier of a bridge with SMA and ECC compared to cast in place bridge pier with conventional steel and concrete. The new bridge pier had a greater drift ratio without important damage. And the residual displacements were 79% lower with the new bridge pier than with the control one.
Varela and Saiidi [63] came up with a new concept of structure where its components can be disassembled and reassembled. They tested a 0.25 scale column, with Niti rebars in the plastic hinge analysis, on a shake table that simulated earthquakes. The disassembled-reassembled column experienced similar results (force and drift capacity) to the initial column. They were no significant damage in the tested

columns with a drift ratio up to 7% while a RC column would have damage with such a drift ratio.
After that, Varela and Saiidi published a paper [64] to evaluate the seismic behaviour of the system developed in [63], where the plastic hinge region can be disassembled. For this purpose, they tested two 0.25 scale columns with SMA bars and ECC subjected to uniaxial simulated seismic loading. One other objective was to determine the properties and the feasibility of disassembled-reassembled columns. The experimental tests showed that the damage in the critical region was small for drift between 6-7%, and SMA rebars were effective for the re-centring of the column. Also, the secondary purpose was fully reached, the reassembled column had similar seismic behaviour to the original one.
Jung et al. [11] studied the active confinement of RC columns with SMA spiral wires. They built two 1/6 scale specimens retrofitted and repaired with SMA spirals to test on one bidirectional shake table (cf. Fig. 2.21). Results show that SMA spirals protect the concrete from crushing but also help to delay damage in the rebars, which helps to reduce residual displacements. SMA retrofitted columns show bigger ductility when subjected to strong seismic actions with a maximal drift ratio of 10.5% without crushing the concrete (cf. Fig. 2.22).

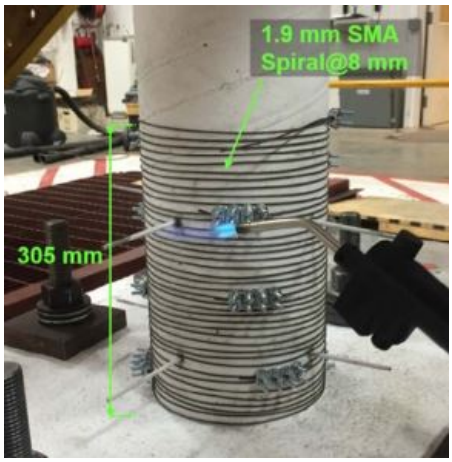
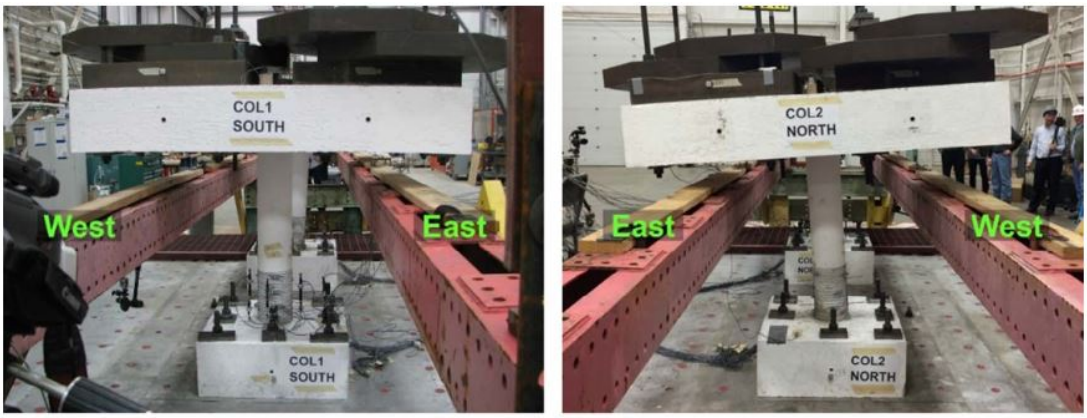


Figure 2.21: Test specimens in retrofitted condition [11]

Xing et al. [65] tested seven RC columns under cyclic lateral loading to study the strength improvement of RC columns. Several parameters varied, such as the type of reinforcement, the presence of Carbon Fiber Reinforced Polymer,.. and their influence was investigated. The measurements stated that the lateral load capacity and the energy absorption increased and the stiffness degradation decreased for SMA or CFRP bars strengthening.



(a) (b)

Figure 2.22: Residual drift of the test specimens after test run 6: (a) COL-1 (SMA retrofitted) and (b) COL-2 (as-built) [11]

2.2.4 Beam-Column joints

Although they are several studies about the beam-column connection, not so much due to the complexity of the experiment and the measurements to do.

During seismic actions, beam-column joints can undergo large stresses and damage, which can lead to the failure of the structure. The properties of superelasticity can be used to reduce residual displacements in the plastic hinge region. Several studies recommend using SMA rebars rather than steel rebars in the plastic hinge region of beam-column joints.

The first experimental tests were conducted by Youssef et al. [66], one beam-column joint reinforced with steel and another with SMA rebars were tested under reverse cyclic loading. After a comparison of the drifts, rotation and ability to dissipate energy, they conclude that the SMA-joint had a residual drift of 1.98% and the steel-joint 4.94%, the first one was able to recover a big part of its post-yield displacement.
Nehdi et al. [67] studied two 3/4 scale SMA–FRP hybrid RC beam-column joints under reverse cyclic loading, the first one made of steel while the other was reinforced with SMA rebars at the plastic hinge region and FRP rebars for the rest of the structure, as represented in Fig. 2.23. Although lower residual displacements could be expected for the SMA joint due to the superelasticity, similar residual displacements were observed for both models, but mostly due to slippage of the bars in the couplers. But comparable force-displacement hysteretic responses were recorded for both models.

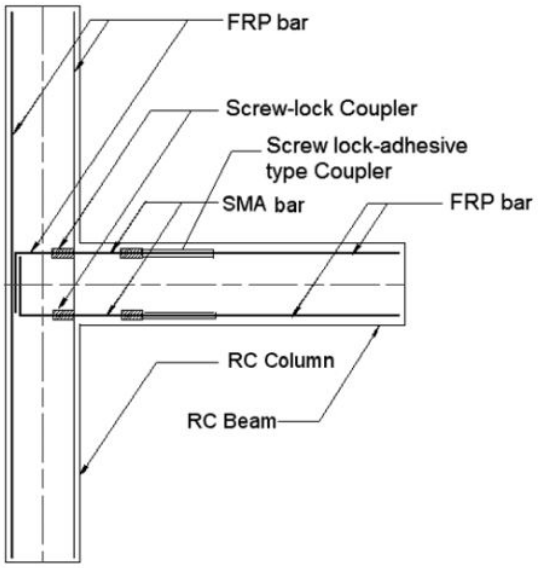


Figure 2.23: Beam column joint with SMA [67]

One year after, Nehdi et al. [68] tested a 3/4 scale beam-column joint with SMA reinforcement and then repaired with commercially available flowable Structural-Repair-Concrete (SRC) and retested under reverse cyclic loading. Then a comparison between the original one and the rebuilt one was done. The results show that SMA joints are able to recover nearly all of their post-yield deformation, requiring a minimum amount of repair even after a large earthquake. It was also shown that the use of SRC to repair damaged beam-column joint can restore its full capacity.
Oudah and El-Hacha wrote 2 papers where they tested beam-column joints. In the first one [69], six beam-column joints were tested under cyclic loading varying several parameters such as SMA or steel reinforcement, the spacing between the stirrups and the anchorage of the rebars. The results obtained show that the SMA-joint has a lower ultimate force capacity (78 kN) than the steel one (145 kN) due to the slippage and fracture of the SMA reinforcement in the coupler.
In the second one [70], they tried to move away the plastic hinge analysis from the beam-column joint by doing a vertical slot in the beam at a distance equal to the depth of the beam of the joint as sketched in Fig. 2.24. Three joints were built, the first without a slot and made of regular steel (control), the second with a slot and regular steel, the last one with slot and SMA reinforcement, and tested under cyclic loading. The results indicated better behaviour of the SMA joint than the control specimen in mitigating the pinching shear effect, maintaining a self-centring behaviour, reducing joint distortion, and relocating the plastic hinge region away

from the face of the column. SMA-joint had also smaller residual displacements and a bigger drift capacity than the two other beam-column joints.

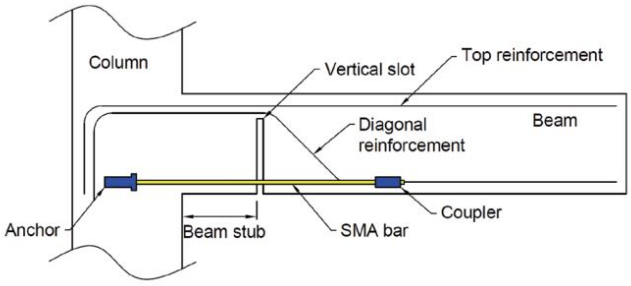


Figure 2.24: Schematic drawing of proposed plastic hinge detail [70]

Yurdakul et al. [71] studied the retrofit of non-seismically designed beam-column joints by post-tensioned superelastic shape memory alloy bars. They built three full-scale beam-column joints, the first one is reinforced with steel (control) and two retrofitted with post-tensioned SMA, tested under quasi-static cyclic loading with a drift ratio up to 8%. The control specimen underwent a brittle failure with cracks concentrated at the connection. While the SMA post-tensioned specimens had a ductile failure with few cracks at the connection. And the lateral load capacity of the retrofitted specimens with both post-tension materials was considerably improved compared to the reference specimen.
Oudah and El-Hacha [72] proposed a new monolithic self-centring beam-column joint to move away the plastic hinge region from the connection between the beam and the column thanks to a double vertical slot in the beam (one from the top, the second from the bottom) placed at a distance of the connection equal to the depth of the beam. Test results indicated the ability of the connection to self-centre at drift up to 14% while experiencing a flag-shaped hysteretic response.

2.3 Loading rate effect

The loading rate effect is already studied in the scientific literature, especially the strain rate, which allows having a better comparison than the loading rate. This section provides a summary of important information found in the literature on the loading-rate effect of SMA, the thermomechanical properties of SMA and the loading rate effect of RC structures.

According to Jin et al [73] and Asprone et al [74], during seismic events, the strain rate ($\dot{\varepsilon}$) is $10^{-3}/s$ for typical earthquakes, and $\dot{\varepsilon} = 10^{-1}/s$ for severe earthquakes.

As mentioned by Deng et al. [24], the time of loading will have an impact on the behaviour of the structure. Indeed, the longer the actuating time, the greater the fraction of martensite will be transformed to austenite.

Tobushi et al. [75] tested NiTi wires in tension to study the effect of the strain rate. The influence of mechanical training and temperature variation on the deformation properties is also investigated.
An exothermic reaction occurs in the SMA (Martensite transformation) when the alloy is cooled down under no loading, and on the other hand, an endothermic reaction occurs when heating the alloy. In the same manner, endothermic and exothermic reactions occur during phase transformations at the same time as the loading/unloading process.
According to the experimental results, they concluded that the temperature variation and the strain rate influence the mechanical response. For $\dot{\varepsilon} \leq 2\%/min(\simeq 3.3\times10^{-4}/s)$, the temperature variation was small, also, the superelasticity property effect isn't modified. While for $\dot{\varepsilon} \leq 10\%/min(\simeq 1.67 \times 10^{-3}/s)$, so in the earthquake strain rate range, the temperature increases during the loading accordingly to $\dot{\varepsilon}$ and the Martensite transformation stress also.

Sia Nemat-Nasser and Wei-Guo Guo [76] tested six SMA samples in compression at different strain rates and different temperatures. Results indicate that the transformation stress raises with the loading rate. The stress levels are greater when the loading rate is important. Figure 2.25 shows the effect of temperature on the plateau stress for samples loaded at $10^{-3}/s$ strain rate. The plateau disappears for a 396 K initial test temperature. And Fig 2.26 shows the plateau slope of the stress-strain curves increasing with temperature.
Above a critical temperature, the austenite phase is stable and adding stress will not lead to martensitic transformation.

In RC structures, according to Jin et al. [73], a greater stiffness of the beam is expected. Indeed, the results of their experimental tests showed that the initial stiffness of a RC structure at a strain rate of $10^{-1}/s$ is about three times that at quasi-static state.
Asprone et al. [74] concluded that increasing the strain rate leads to higher mechanical properties, larger ultimate bending moment and larger curvature with seismic strain rates than at quasi-static rate. An increase in the force capacity and displacement capacity can be expected if a brittle failure mechanism doesn't occur.

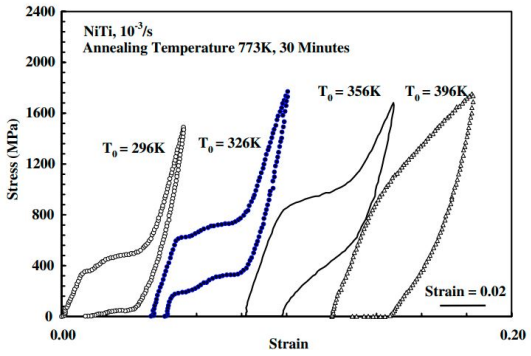


Figure 2.25: Stress–strain curves at $10^{-3}/s$ strain rate and indicated initial temperatures; each curve starts at zero strain [76]

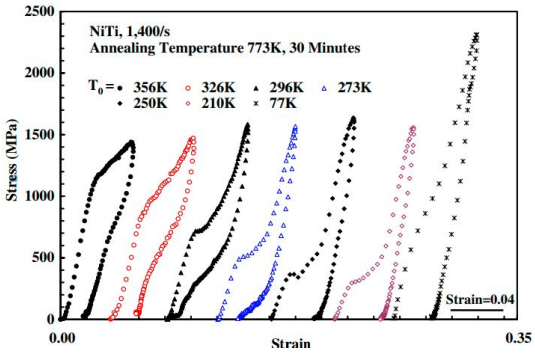


Figure 2.26: Stress-strain curves at $1400/s$ loading strain rate and indicated initial temperatures; each test starts at zero strain [76]

CHAPTER

3

NUMERICAL ANALYSIS

"All models are wrong, but some are useful." – George E. P. Box

3.1 Finite Element Modelling

In this chapter, the numerical analysis will try to numerically anticipate the experimental behaviour of the beams that will be tested, with a focus on residual displacements. To do so, a program that can simulate the behaviour of RC beams will be used.
The software used is VecTor2, a finite element modelling program to simulate the behaviour of RC structures based on the Modified Compression Field Theory for nonlinear finite element analysis of reinforced concrete membrane structures developed at the University of Toronto. Explanations about the software are available in the manual [77].

3.2 Calibration of VecTor2

Before starting the simulations of the beams that will be tested as part of this master thesis, a calibration of the finite element model is necessary. This section is divided into two parts, an analysis with different mesh sizes and an analysis of

the different material models to justify the decision of mesh and model that will be created in section 3.3. To perform this analysis, the beam B1-SM presented in Abdulrhida's thesis [10] is used. In his research, he tested 7 beams, 3 with only steel reinforcement, and 4 with steel and Nitinol reinforcement. The beams were simply supported and 2 points loads were located at the centre of the beams (as sketched in Fig. 3.1).
The details about the reinforcement ratios, properties of materials and support conditions of the numerical model are well presented in Abdulridha's thesis [10].

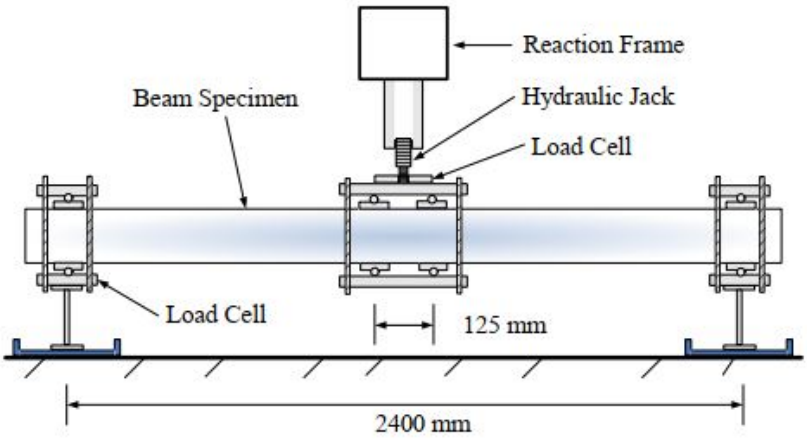


Figure 3.1: Test set up from Abdulrhida [10]

3.2.1 Mesh sensitivity analysis

As a general remark, only rectangular elements are used, and triangular elements are avoided in the mesh, the more coherent the elements are, the better the convergence of the program and the ideal behaviour will be. Small elements can introduce strain/stress concentrations, which can result in weird results. On the same principle, in order to have a regular mesh, the maximum shape ratio is 1:1.5 for the rectangular elements. Every numerical simulation is displacement-based controlled.
The mesh sensitivity was tested by changing the number of elements of the beam. The names of the beam come from the dimension of the square elements ($dx = 25$ mm means that nodes are 25mm apart in the numerical model). If dx increases, the number of elements decreases.
In this subsection, the basic options implemented in VecTor2 (cf. Fig. 3.2) are used for the calculations while in the next subsection, these parameters will be modified

in order to find those that best represent the behaviour of the beam under loading.

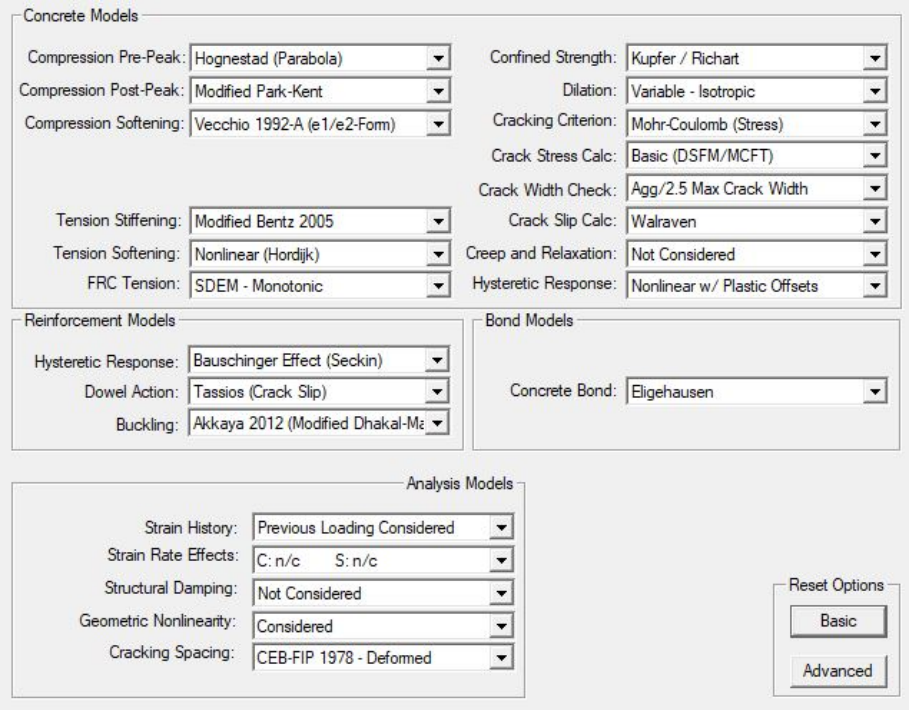


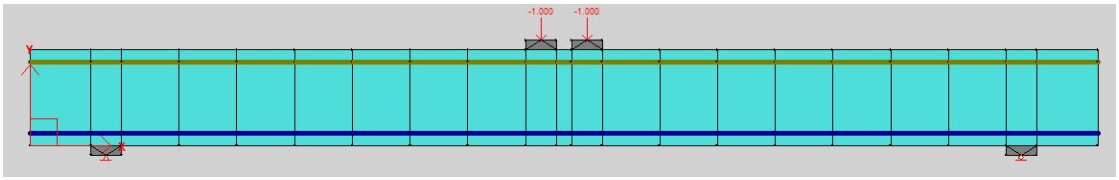
Figure 3.2: Basic options for models in VecTor2

B1-SM:
In his thesis, Abdulridha tested the beam B1-SM in bending with a monotonic loading. In the real experiment, the beam failed at 65mm, which is equivalent to 36 kN by concrete crushing in the flexural compression zone after the yielding of the longitudinal rebars.

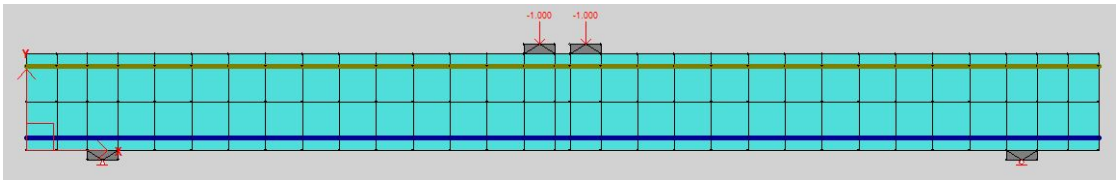
To study the effect of the size mesh, 5 mesh sizes are considered: dx=150mm, dx=100mm, dx = 75mm, dx=50mm, dx=25mm as it can be seen in Fig. 3.3.
For the support conditions and the applied forces, steel plates are numerically modelled as in the real experimental tests. This avoids undesirable local phenomena.

For a monotonic force applied on the beam up to failure (displacement-based with $\Delta_{increment} = 1mm$), the Load-Displacement curves calculated are represented in Fig. 3.4 (the experimental result is represented in this graph in blue to show which curve is the better approximation of the reality).

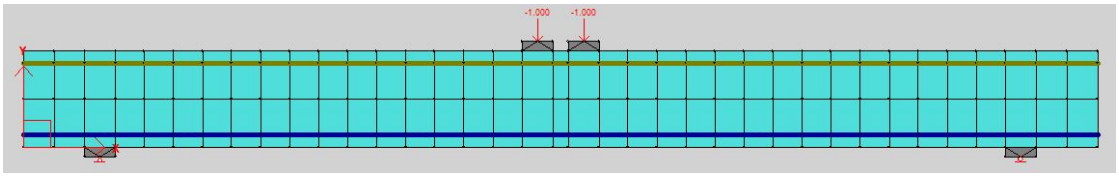
What can be concluded from the graph in Fig. 3.4 is that the finest the mesh is, the better and smoother the results are. Even though the real behaviour of



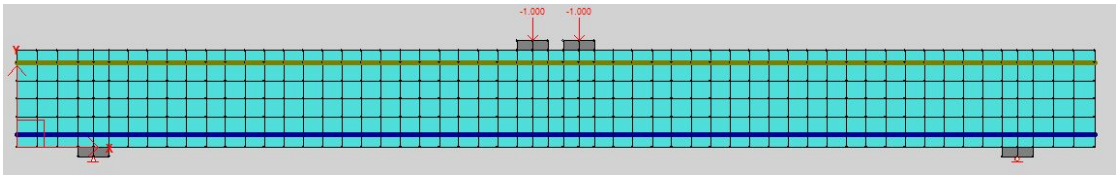
(a) dx=150



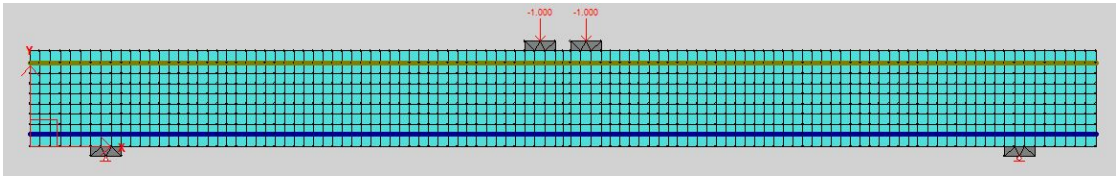
(b) dx=100



(c) dx=75



(d) dx=50



(e) dx=25

Figure 3.3: Mesh size analysis

the beam is not caught up by these simulations, It can be seen that the $dx = 25$ mm model is the better one. It is the nearest to the experimental result (=blue curve) and breaks at 79 [mm], 10 [mm] above the measured results and has the best numerical stability. But the other meshes give a good first idea with a lower computation time, the $dx = 75$ mm model seems to be a good compromise in terms of results-computational time.

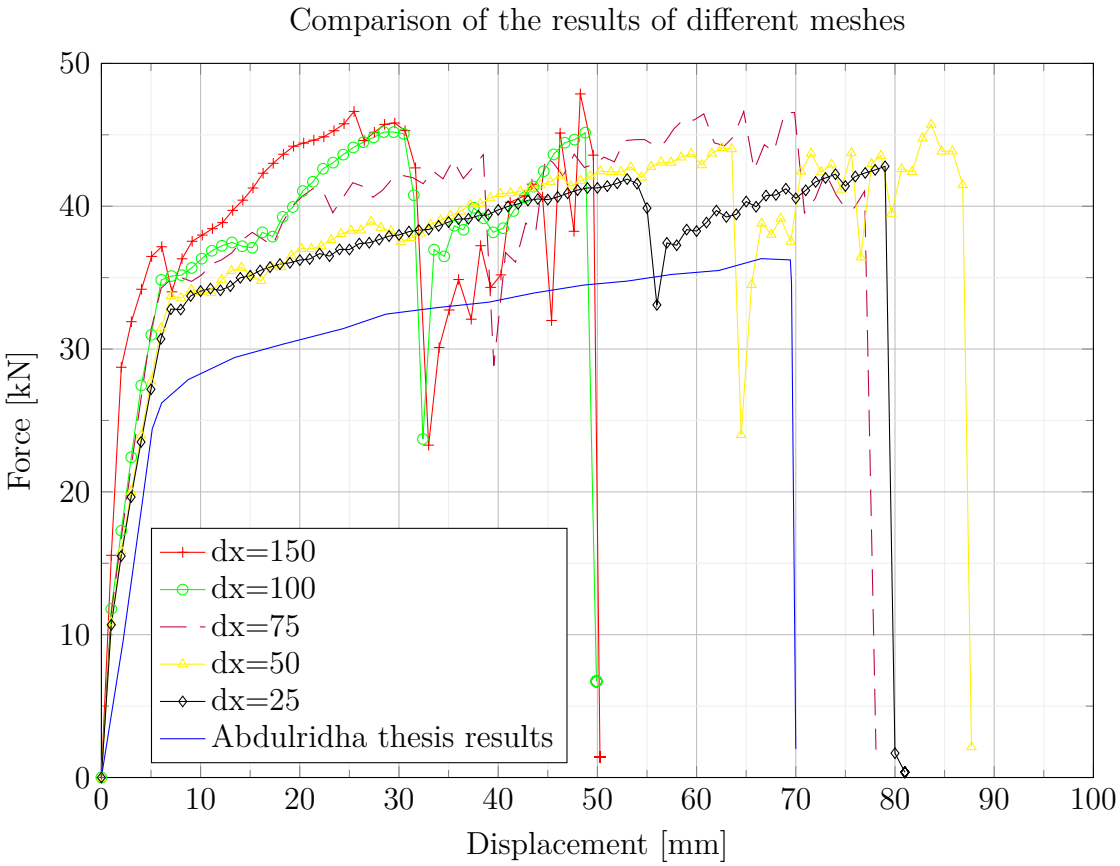


Figure 3.4: Load-Displacement response for several meshes

3.2.2 Material models

Knowing the mesh size to be used, the calculation models implemented in Vector2 will be modified for the second analysis. For the previous mesh analysis, the default basic parameters were used. Now, the models will be changed one by one to see the effect of each of them.
Performing sensitivity studies for all the material models would be very time-consuming. So, this sensitivity study is based on the analysis performed by Constantin [78] in his thesis. The following parameters are analysed: concrete compression pre-peak behaviour, concrete compression post-peak behaviour, confined concrete strength, lateral expansion model for concrete (dilatation) and concrete tension softening.

Compression pre-peak behaviour:
The behaviour of the concrete in uniaxial compression before the peak is nonlinear and is described by 10 models in VecTor2, the linear model isn't represented because it's too simplified and unrealistic results are obtained. In this part, the ascending branch only is studied. These models compute the principal compressive stress f_{c3} if the principal compressive strain ε_{c3} is less than the peak strain ε_p. The model tested with incremental displacements and with the following support conditions is represented in Fig. 3.5 a). Stress-strain curves of the different models are represented in Fig. 3.5 b). For the final model, the author chooses the Hogenestad model (which is the model by default) due to its realistic behaviour and the other models have the peak occurring too early in terms of strains, the strains of such a concrete should be around 2.2‰ [79].

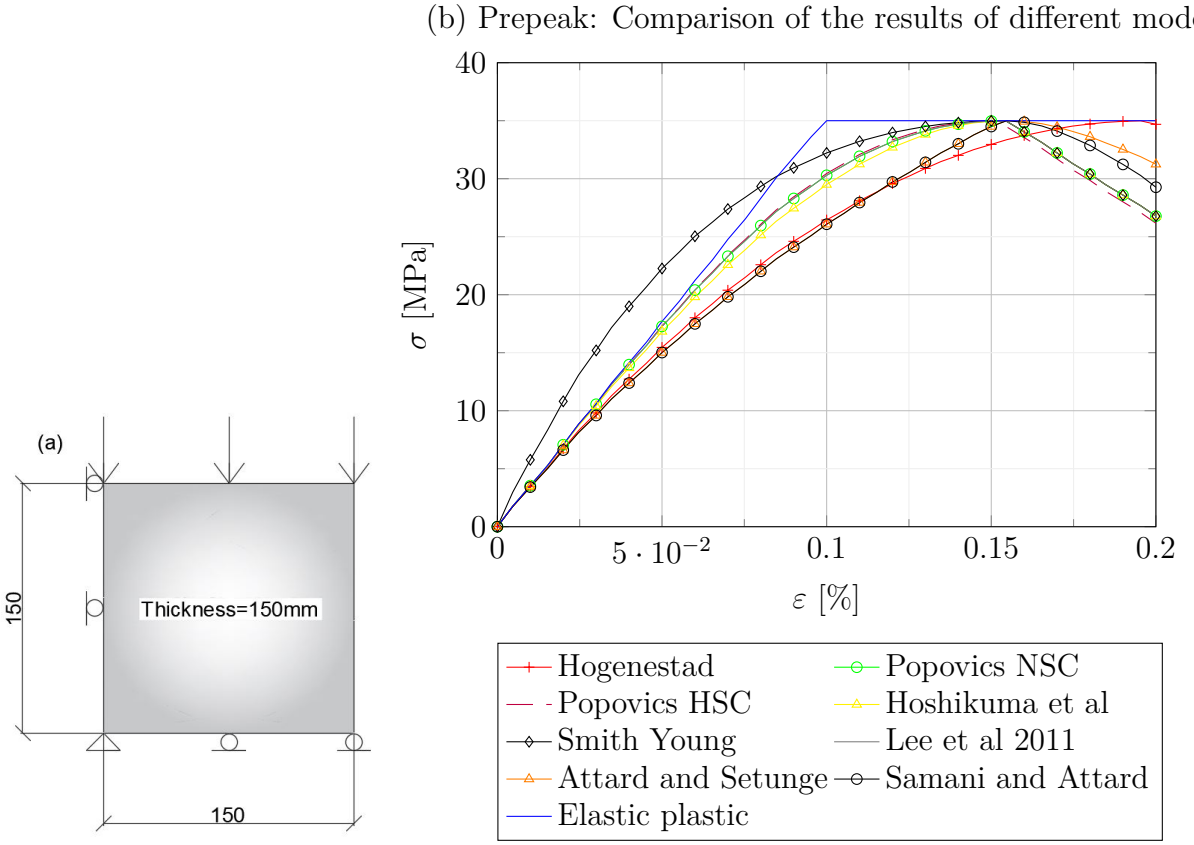


Figure 3.5: Behaviour of concrete in compression: tested model (a) and response of pre-peak models (b).

Compression post-peak behaviour:
The second part of the compressive resistance after the peak, when the strain is greater than ε_p, computes the principal compressive stress f_{ci}. The different strain-stress models are made for confined concrete, except for Saenz/Spacone. Thus, an out-of-plane reinforcement ratio of 0.32% is used for the V2 calculations in the cube (typical reinforcement of the experimental beam used in this master thesis). The support conditions are represented in Fig. 3.6 a) and the stress-strain relation curves are given in Fig. 3.6 b).
The Elastic-Plastic model looks unrealistic because, after the peak, the stress in the concrete never decreases. While the others have different ascending branches, from fast degradation like Hoshikuma et al. and Lee et al. to lowest degradation like Popovics/Mander or Park Kent (default model). The Samani and Attard and the Attard and Setunge models have a peak at 1.5‰, which is too early in terms

of deformations. The model chosen for the numerical analysis is the Park-Kent model due to its shape near the actual behaviour of concrete in compression.

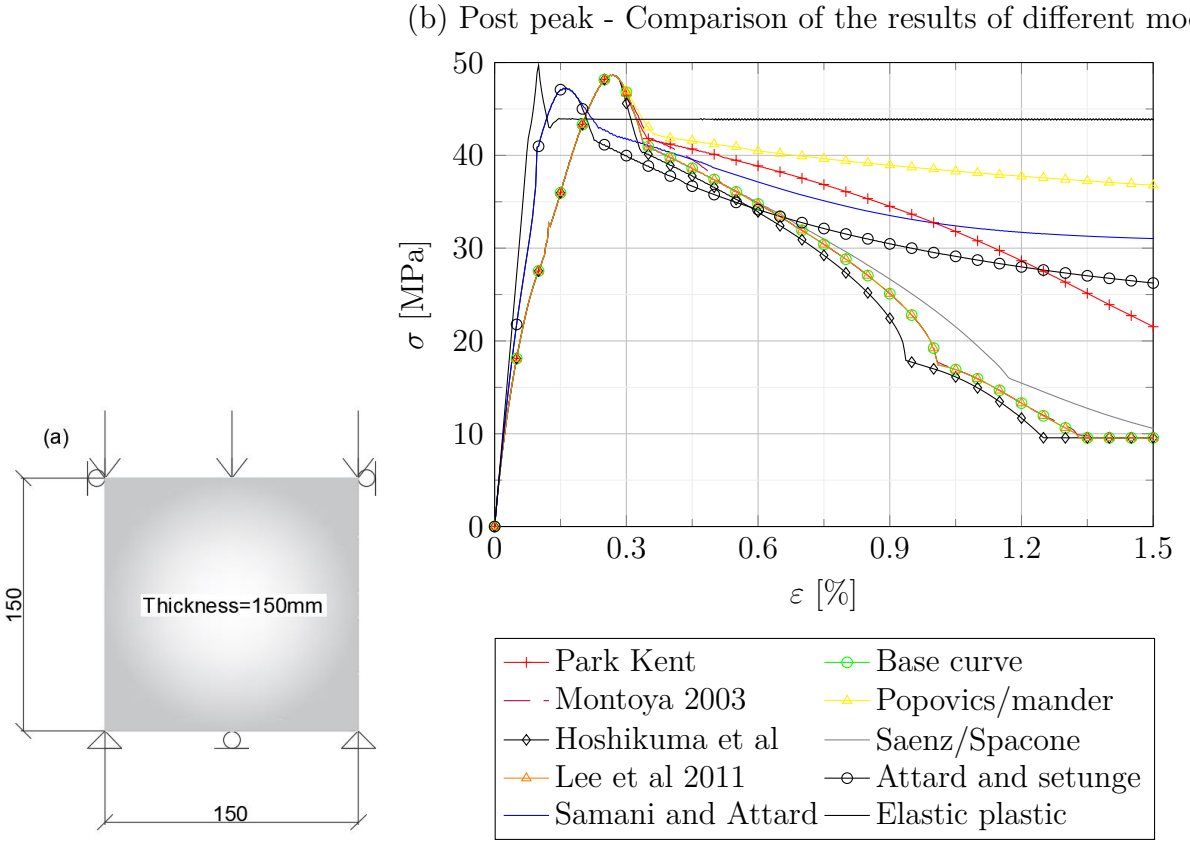


Figure 3.6: Behaviour of concrete in compression: tested model (a) and response of post-peak models (b).

Confined concrete strength:

Confined concrete improves the compressive strength and the ductility of concrete. In VecTor2, the new strength f_p and the new strain ε_p are calculated as follow:

$$f_p = \beta_d \beta_l f'_c$$
$$\varepsilon_p = \beta_d \beta_l \varepsilon_0$$

With β_l used to increase the uniaxial compressive strength and corresponding strain, the β_d factor accounts for compression softening. With these factors, it's possible to determine the new peak compressive strength f_p and strain ε_p.
The different models tested used different ways of calculating these parameters. Figure 3.7 a) shows the support conditions of the concrete cube and the results of the different models available in VecTor2 are sketched in Fig. 3.7 b). The Neglected model doesn't take into account the reinforcement, so it's not a good one, the Montoya/Ottosen model gives unrealistic results, the strains in the concrete are too important without failure. The three last models present results with an increase in the maximal stress and corresponding strain. The decreasing branch is very steep for the Kupfer/Richart model and becomes flatter for Selby and Cui and Sheikh. The Selby model is chosen for the final model because the values of σ and ε increase in a realistic way and the behaviour after the peak is representative of reality.

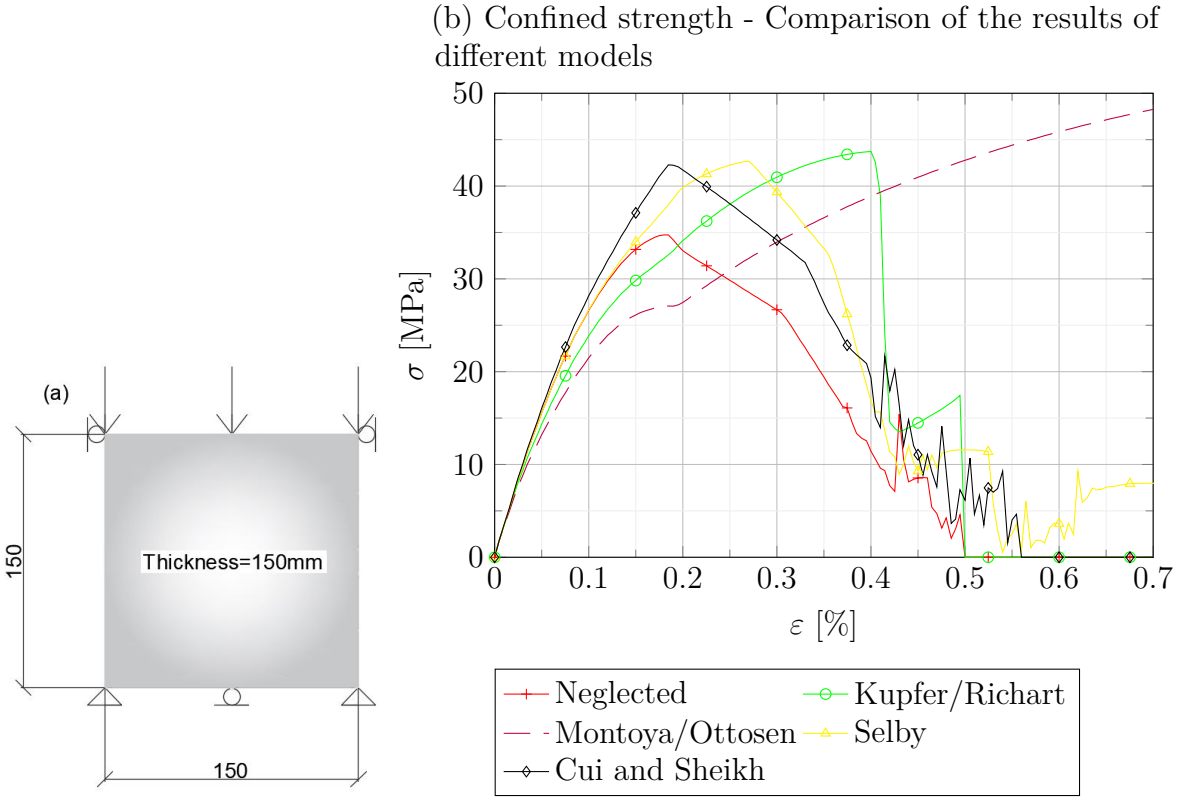


Figure 3.7: Behaviour of concrete in compression: tested model (a) and response of confined strength models (b).

Concrete dilatation:

When compressed, the concrete will expand itself, the more the compression stress applied is important, the more the dilatation will be large due to internal micro-cracking of the concrete. If the concrete is confined with reinforcement, the lateral expansion produces a passive confinement pressure that will increase the strength and ductility of the concrete. In VecTor2, the lateral expansion is implemented using the Poisson ratio, different models are using different ways of calculating this ratio, leading to different results.
Figure 3.8 a) shows the concrete's support conditions and the results of all the models are represented in Fig 3.8 b).
There are instabilities in some curves obtained (Montoya 2003 isotropic, Montoya 2003 orthotropic and Montoya w/ limit isotropic) while the fixed Poisson ratio leads to stable numerical behaviour and is preferred to maybe more realistic models for the numerical stability of the final model. Indeed, even if instabilities aren't shown for all the models on the graph, instabilities appear for larger strains ($\varepsilon \geq 0.7\%$).

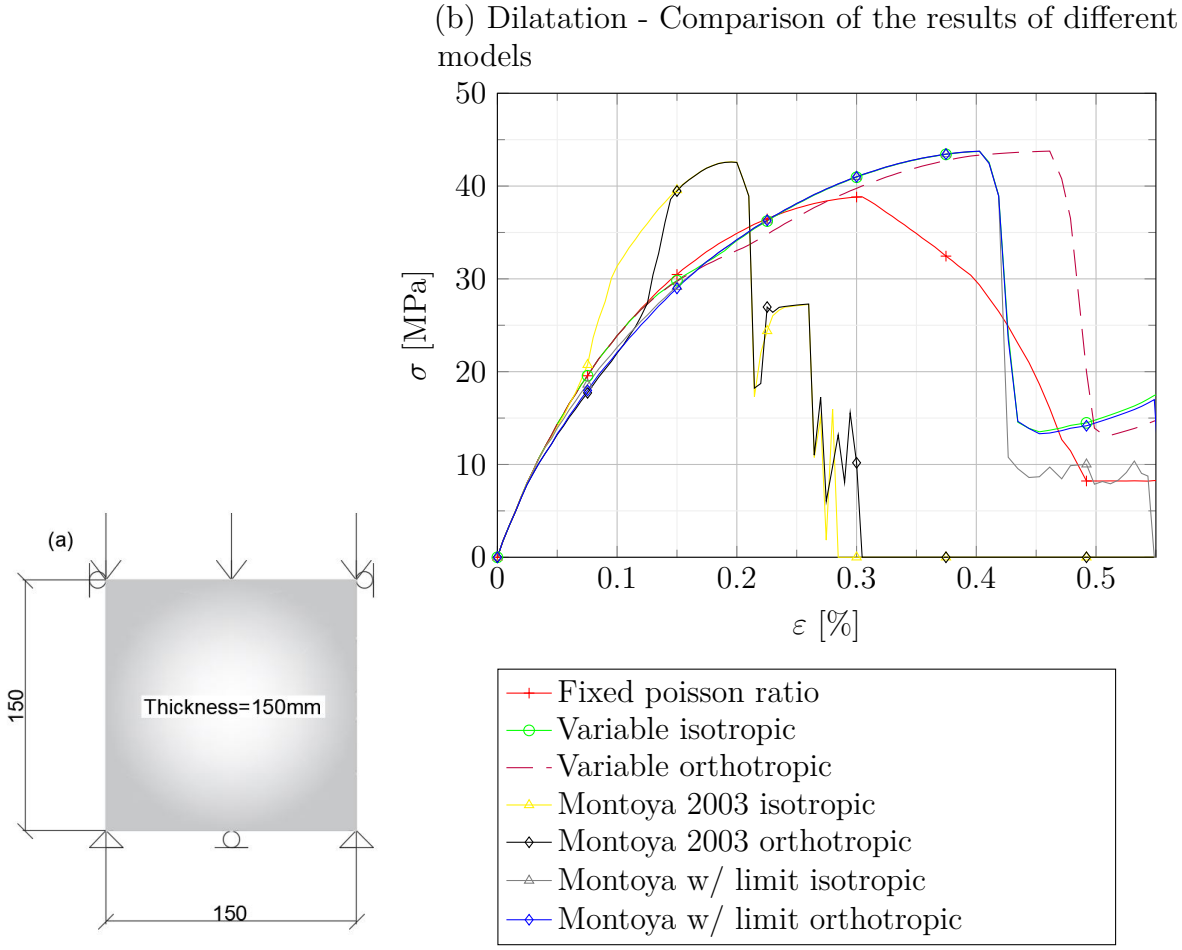


Figure 3.8: Behaviour of concrete's dilatation: tested model (a) and response of dilatation models (b).

Tension softening:

When tension stress is applied on concrete, cracks will appear. After cracks, the tensile stress will not drop to 0 immediately. The concrete is not perfectly brittle, so when cracks are appearing, concrete will progressively release stress. Tension softening takes into account this post-cracking tensile resistance in plain concrete. This phenomenon is important to model because it allows estimation of stress redistribution in RC structures. The decreasing part after the cracks apparition helps to determine accurately the load-deformation curves and the ductility of RC structures.
The cube tested and the support conditions are represented in Fig. 3.9 a) and the results obtained for the 6 models are represented in Fig. 3.9 b).

The different models give different results. When the tension softening isn't considered, a very abrupt behaviour after the peak is observed while the other models show more slowly descending branches. According to Raluca Constantin [78], the influence of this parameter is negligible for the global results and relatively small for the local results. The numerically simplest model (Linear model) is chosen to reduce the calculation time.

(b) Tension softening - Comparison of the results of different models

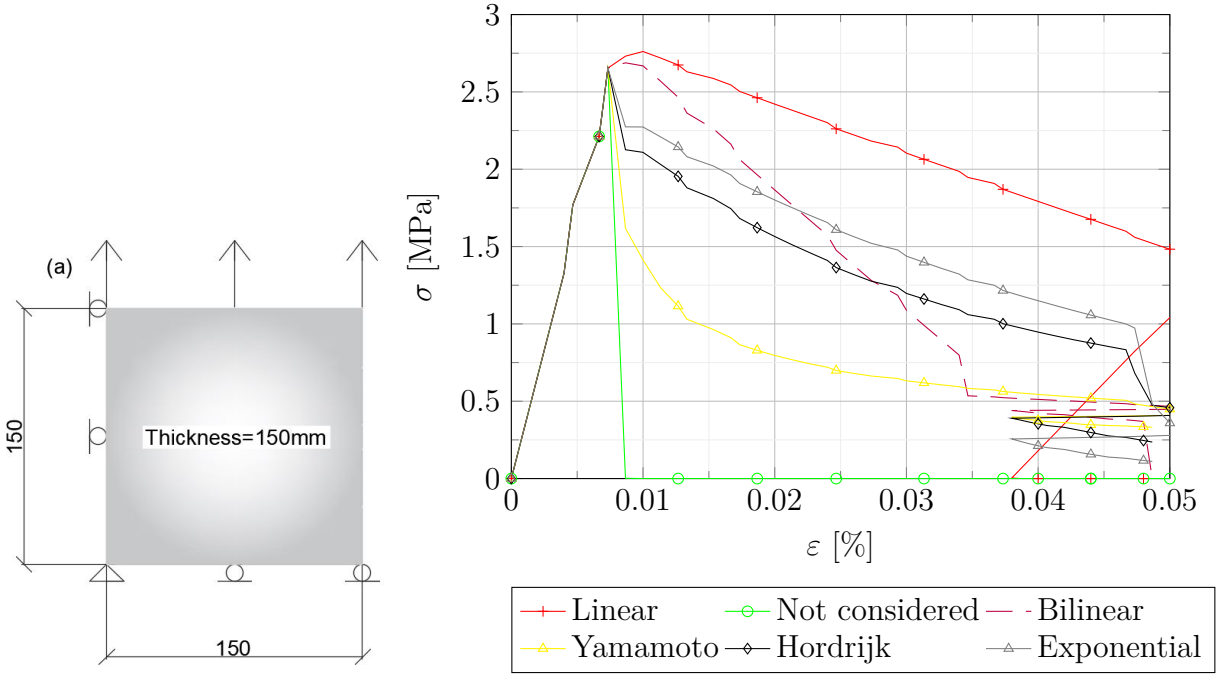


Figure 3.9: Behaviour of concrete in tension: tested model (a) and response of tension softening models (b).

Bond type:

One crucial point to model is the bond-slip connection between the SMA rebar and the concrete. The Nitinol rebar is smooth and thus the truss cannot be considered as perfectly bonded over the entire length. It is an imperfect connection, this can be modelled in VecTor2 with link elements. Numerical link elements will be detailed in section 3.3.2.
One type of bond is created for the SMA due to the smooth shape of the rebar, the connection between the concrete and the SMA is imperfect. The steel reinforcement can be considered as perfectly bonded over the entire length because of the ribs

and lugs.

3.3 Description of the finite element model

In this section are taken the properties given in the finite element software

3.3.1 Material properties

The material properties are taken from experimental tests done in the lab or are the properties given by the producer.

Steel

From the tests done in lab, the stress-strain relation given in Fig. 4.8 for the $\phi 12$ and $\phi 8$ steel reinforcement rebar is given and used to model the following steel properties in VecTor2.
According to the manual, the following equations lead the steel response (cf. Fig. 3.10):

$$f_s = \begin{cases} E_s \varepsilon_s & \text{for } \varepsilon_s \leq \varepsilon_y \\ f_y & \text{for } \varepsilon_y < \varepsilon_s \leq \varepsilon_{sh} \\ f_u + (f_y - f_u)\left(\frac{\varepsilon_u - \varepsilon_s}{\varepsilon_u - \varepsilon_{sh}}\right)^4 & \text{for } \varepsilon_{sh} < \varepsilon_s \leq \varepsilon_u \\ 0 & \text{for } \varepsilon_u \geq \varepsilon_s \end{cases}$$

The hysteretic response of the steel is modelled by the Seckin Model w/ Bauschinger Effect. The response of one cycle of loading and unloading can be seen in Fig. 3.11. The Bauschinger effect is the fact that the reinforcement exhibits premature yielding upon load reversal after plastic prestraining due to stress changes at the microscopic level.
On the graph of the hysteretic response are the following parameters: the plastic offset strain in the current cycle ε_0, the yield strain ε_y, the maximum positive strain attained in previous cycles ε_m, the tangent stiffness E_m at ε_m, the unloading modulus E_r, the elastic modulus of the monotonic stress-strain response E_s and f_m is the stress corresponding to ε_m.

In VecTor 2 are implemented the following values (cf. Table 3.1).

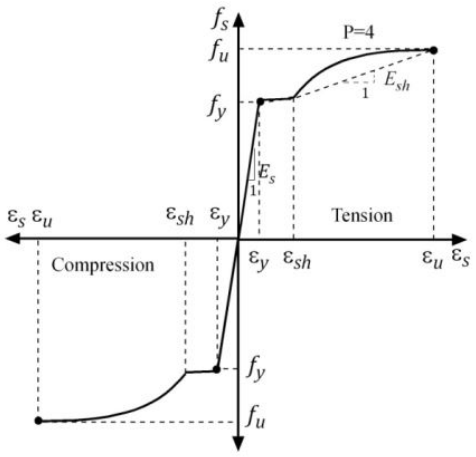


Figure 3.10: Typical stress-strain response of steel used in VecTor2 [77].

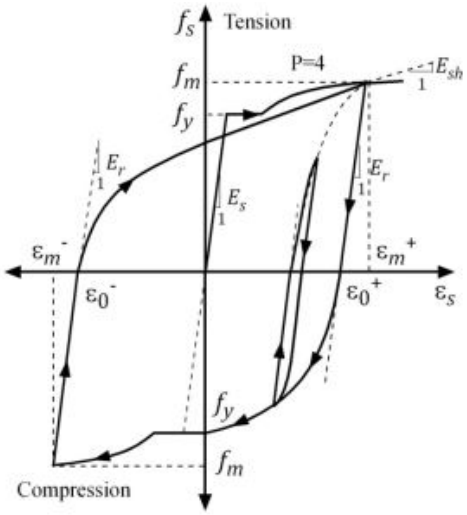


Figure 3.11: Seckin model of ductile steel reinforcement for hysteretic response: Seckin w/ Bauschinger-HP4 [77].

φ [mm]	E_s [MPa]	f_y [MPa]	f_u [MPa]	ε_{sh} [me]	ε_u [me]
8	196000	538	664	25	128
12	199000	580	690	20	113

Table 3.1: Steel properties in VecTor2.

SMA

Two types of SMA are available in VecTor2: SMA type 1, which is not used in the numerical simulations, has an idealised behaviour with no strain offsets, and SMA type 2, which corresponds to a more realistic behaviour, the stress-strain relation is given in Fig. 3.12.

In VecTor 2 are implemented the following values (cf. table 3.2).

φ [mm]	E_s [MPa]	f_y [MPa]	f_u [MPa]	ε_{sh}[me]	$\varepsilon_u[me]$
12.7	31000	330	1053	40	177

Table 3.2: SMA properties in VecTor2.

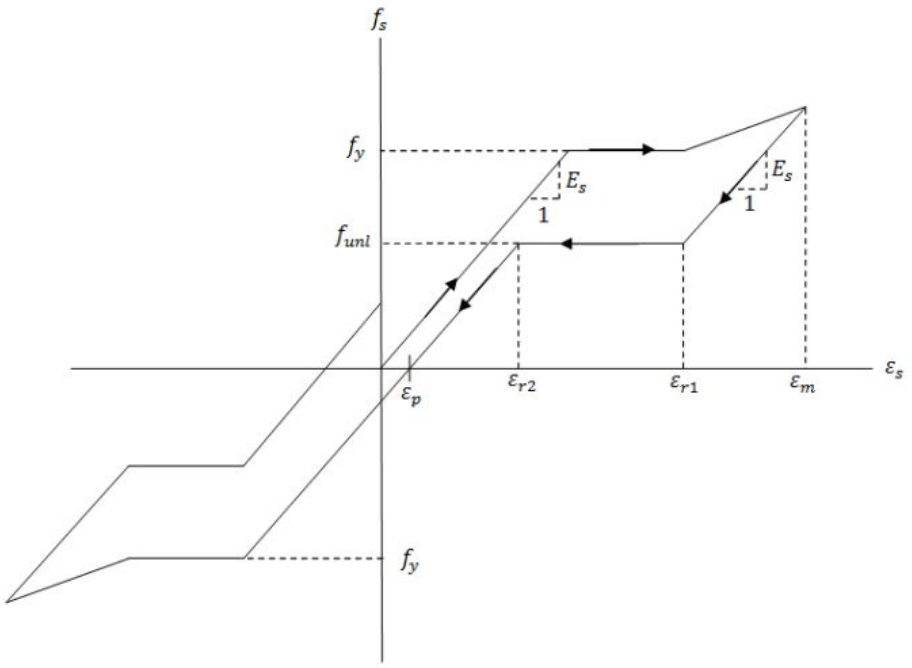


Figure 3.12: Typical stress-strain response of SMA type 2 used in VecTor2 [77]

Concrete

VecTor2 only needs two parameters, the compressive strength of the concrete and the thickness. The rest is calculated automatically. The reinforcement can be put as truss when defining the mesh and the structure (which is done for the longitudinal reinforcement) or smeared in the concrete when defining the concrete (which is done for the transversal reinforcement).
The following values were used (S1 beam has different values than N1 and N2 beams because the concrete wasn't poured at the same moment and therefore has small differences in the mechanical properties):

	Beam S1	Beams N1 and N2
Cylinder compressive strength [MPa]	34.4	32.3
Tensile strength [MPa]	2.76	3.46

3.3.2 Link elements

Since the SMA rebar is smooth as it can be seen in the pictures in Chapter 4, the interaction between the concrete and the rebar isn't perfect, unlike the interaction between steel and concrete. All along the SMA rebars, *'Link Elements'* are placed in VecTor2.

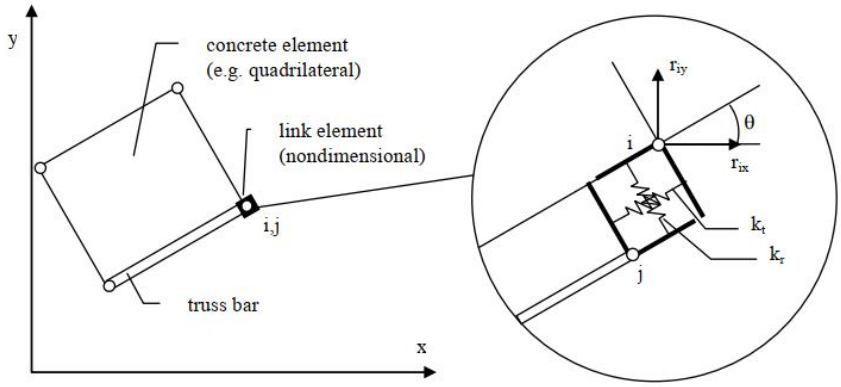


Figure 3.13: Link element [77].

A link element is a bond-slip type of element used as an interface between concrete and reinforcement rebars. Two nodes are defined, one on the reinforcement, the other on the concrete with the same coordinates. When the stress is applied, there will be a relative displacement between the rebar and the concrete.
A link element can be represented as two orthogonal springs as represented in Fig. 3.13. The springs are tangentially and radially to the discrete reinforcement element and will deform tangential or radial when stress or deformation is applied.

In VecTor2, a bond model for embedded smooth rebars is defined with the following properties (cf. Fig. 3.14) and the Eligehausen model is used. This model is the most commonly used in the literature (cf. [10], [78], [80]) and gives generally adequate results.

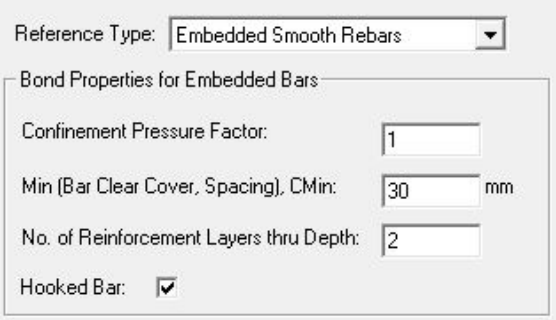


Figure 3.14: Bond type properties

3.3.3 Numerical models

In addition to the properties and models used explained earlier in this chapter, the numerical model used for beam S1 (control beam) and for beams N1 and N2 (with SMA) are shown in Fig. 3.15 and 3.16 respectively.

For beam S1, the support conditions are steel plates simply supported on the bottom to represent the real experimental set-up. At mid-span, steel plates are represented on the top and the bottom of the beam, as in the experimental test. The bottom plate wasn't a perfect set-up because it doesn't allow the beam to deform freely at the mid-span, and limits the central crack opening. For the SMA beams, where the intention was to localise the deformation at the middle, this kind of steel plate wasn't a good idea. So the experimental set-up was modified as explained in Chapter 4, and no steel plates are represented in the numerical model to simulate the behaviour of the beam that can deform and crack freely at the centre of the beam.

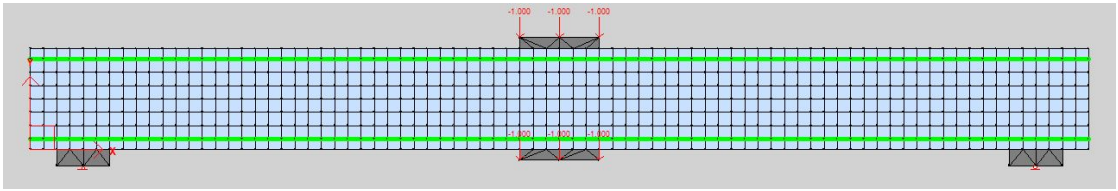


Figure 3.15: Numerical model of beam S1

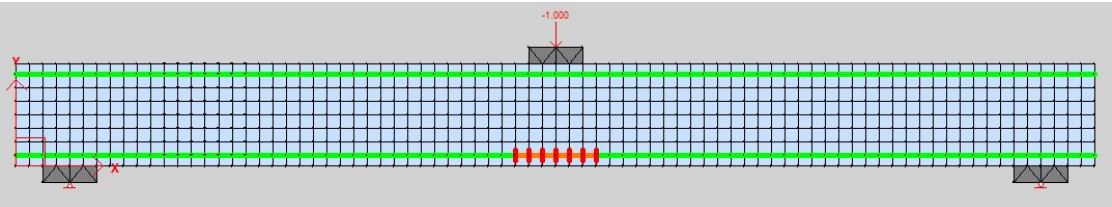


Figure 3.16: Numerical model of beam N1 and N2

CHAPTER

4

EXPERIMENTAL TESTS

4.1 Experimental setup

4.1.1 Description of the beams

For the experimental part of this master thesis, three RC beams are tested, the first one, a control beam (S1), is reinforced with only steel rebars. Two other RC beams have in the bottom reinforcement 100 [mm] of NiTi at the centre of the beam (N1 & N2). Plans of the RC control beam and the SMA beams are given in Fig. 4.1 and Fig. 4.2 respectively. The difference between the 2 NiTi beams is the loading protocol that will be discussed in the following section.
Pictures of the construction of the beams are available in Appendix A.

	Upper Longitudinal Reinforcement	Bottom Longitudinal Reinforcement		Stirrup
		Centre	Extremities	
S1	$2\phi12$	$2\phi12$	$2\phi12$	$\phi8@150mm$
N1	$2\phi12$	2 NiTi	$2\phi12$	$\phi8@150mm$
N2	$2\phi12$	2 NiTi	$2\phi12$	$\phi8@150mm$

Experimental tests were done on beams because of the availability of test setup and moulds in the lab and also to reduce the cost (the SMA is very expensive). And

to have an added value to the actual literature, three important features were added:

- A new connection type (welded connection) between the SMA and the steel. As mentioned in the chapter 2, every experimental study used mechanical couplers to link steel and SMA rebars. This new connection type will avoid relative slippage between the NiTi and the steel.
- Measures done by optical fibres, this allows to have very accurate strain and temperature measurements all along the beam as explained in section 4.7.1, and are represented in Fig. 4.23 and 4.24.
- Different loading rates for the SMA beams.

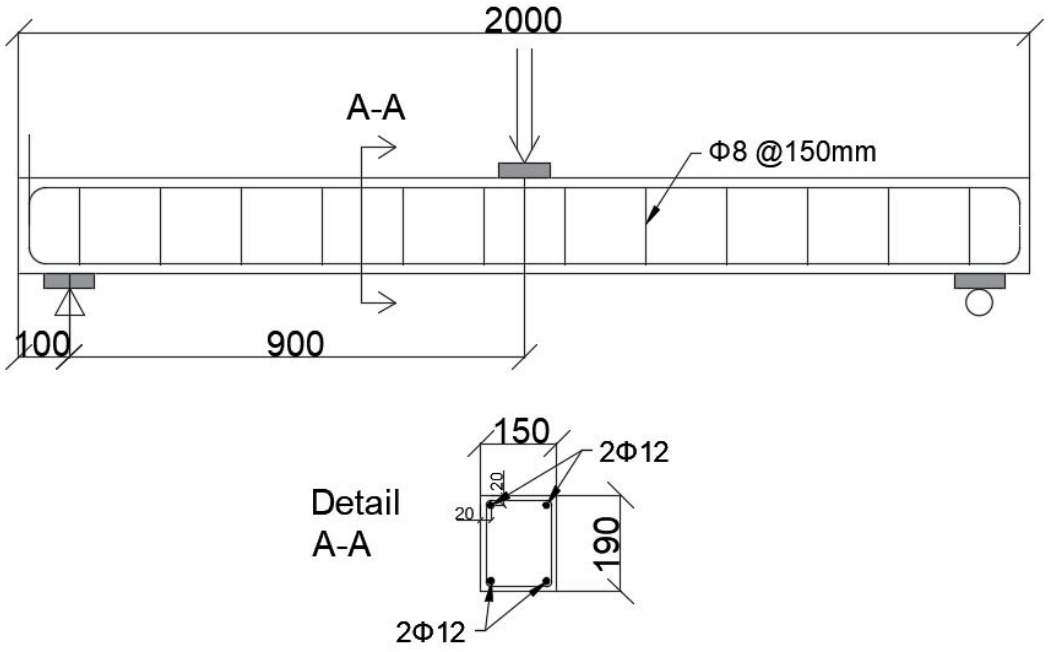


Figure 4.1: RC control beam reinforcing bars

4.1.2 Support conditions

The beams are simply supported. After each cycle, the beams have to come back to 0[mm] displacement in order to avoid an accumulation of residual displacements after several loading stages. Because the beams come back to 0 [mm] displacement,

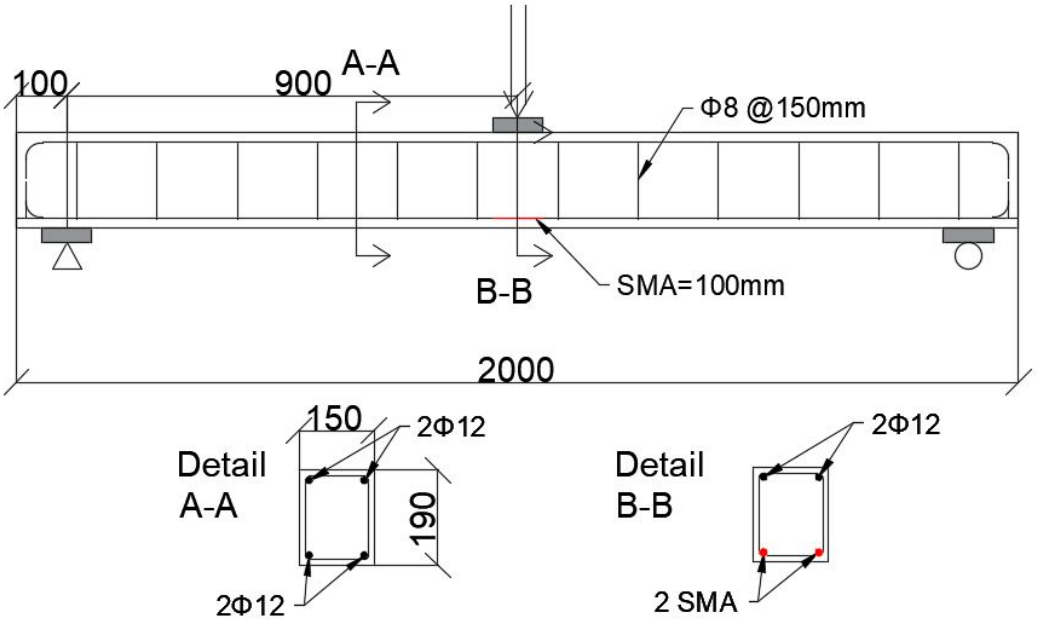


Figure 4.2: RC SMA beams reinforcing bars

a vertical upward force will be transmitted in the supports. The support conditions are illustrated in Fig. 4.3.

The central plate at the bottom of the beam is used to transfer the upward force to the beam. After the test on the RC beam, it was decided to change the central bottom plate because the first setup didn't allow the middle of the beam to deform freely. The crack in the middle was not the bigger one. For the SMA beams, it was important that the central part of the beam (with the SMA rebars) controls the behaviour of the beam and thus can deform freely. The steel plate has been cut into two small disconnected steel plates, allowing the central part to crack and deform freely. This setup is represented in Fig. 4.4 and Fig. 4.5 for the RC control beam and for the SMA beams.

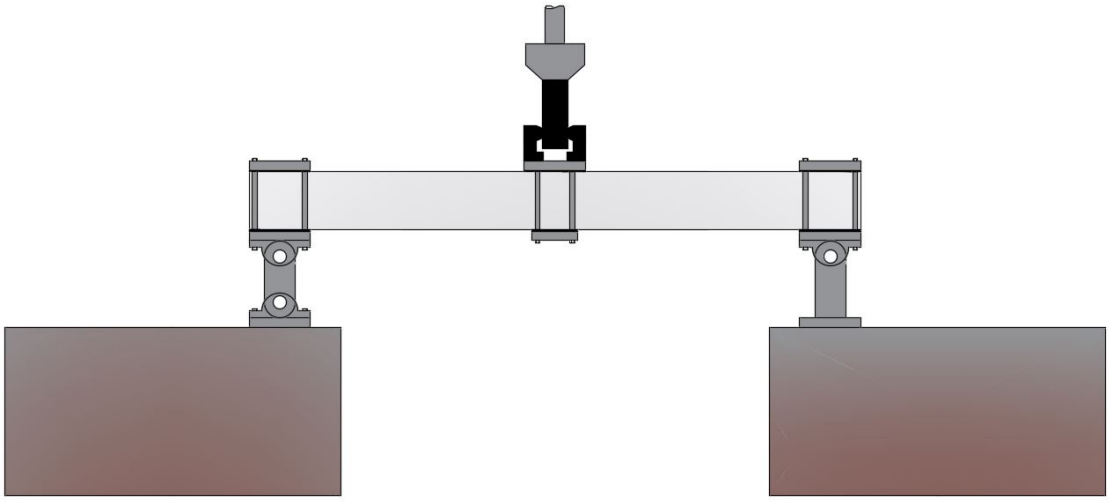


Figure 4.3: Experimental setup

4.2 Loading protocol

To allow a good comparison between the three tests, it was decided to apply the same loading protocol for the three beams. The tests are displacement-based. The difficulty was to find the yielding points of the control RC beam and the SMA RC beams. Using a numerical analysis of the beams loaded monotonically up to failure, it was found that both beam models have approximately the same yield displacement $\Delta_y = 10mm$. The same value of yield displacement for both types of beams is taken, which allows to have one loading protocol and facilitates further comparisons, especially for residual displacements.
Under the yielding point, the four first loading stages are: $\Delta_y/4$, $\Delta_y/2$, $3\Delta_y/4$. At the yielding point and after, the beam is loaded twice at each increment, with an increment of Δ_y. The two peaks are used in the literature, for example by Nakashoji [54], by Choi et al. [60], by Hosseini et al. [61] or even Almeida et al. [22].
The displacements represented in Fig. 4.6 are the vertical displacement measured by the laser on the ground pointed towards the bottom face of the beam and not the displacement of the stroke.
The loading protocol is sketched in Fig. 4.6.

The loading of the control beam S1 and the first SMA beam N1 is done at quasi-static rate, at a speed of 0.25 [mm/s].

For beam N2, the loading protocol will be with a quicker loading, up to 5 [mm/s]. The data of the first experimental test (Beam S1) is used to determine this protocol loading, to have a strain rate comparable to that of an earthquake.

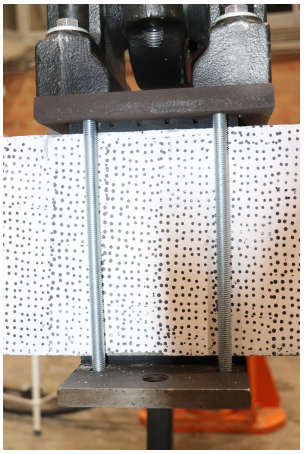


Figure 4.4: Steel plate of RC beam

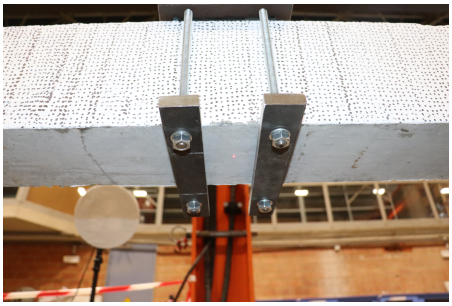


Figure 4.5: Steel plates of SMA beams

Loading protocol for RC control beam S1 and SMA RC beam N1 at quasi-static rate

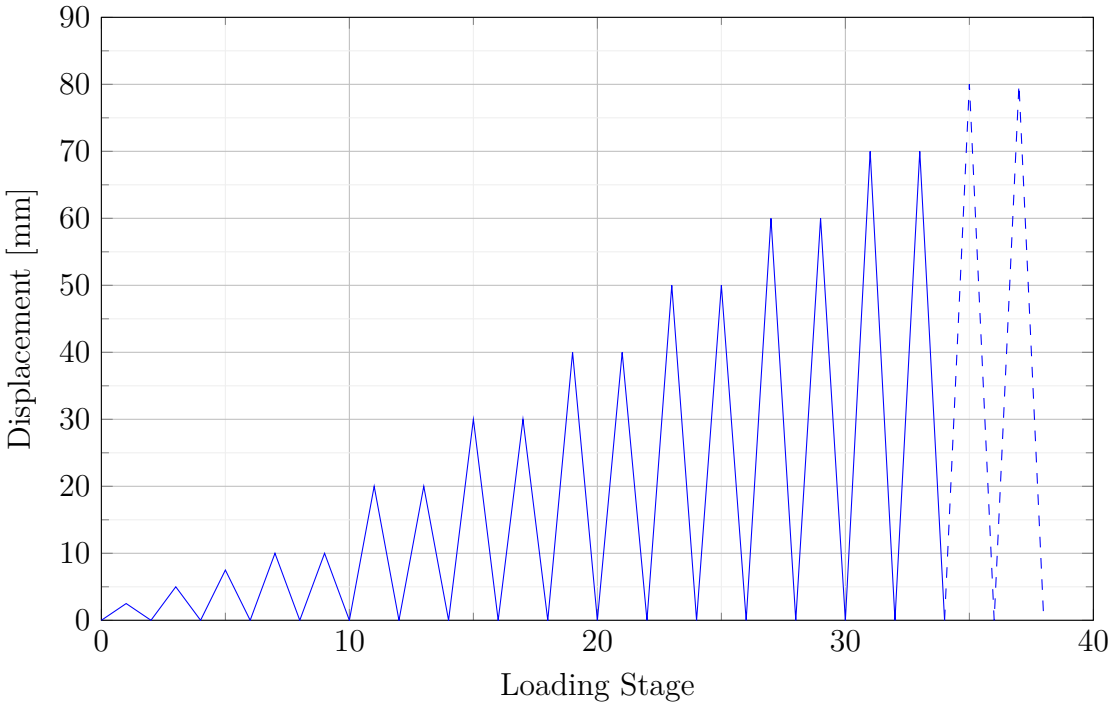


Figure 4.6: Loading Protocol 1

This is detailed in Chapter 5.
For the load stages where the displacement is smaller than 10 [mm], the loading rate is the displacement of the load stage divided by 2, in order to make the load stage in 2 seconds. For the loading stages with displacements bigger than or equal

to 10 [mm], the loading rate is 5 [mm/s] as represented in Fig. 4.7.

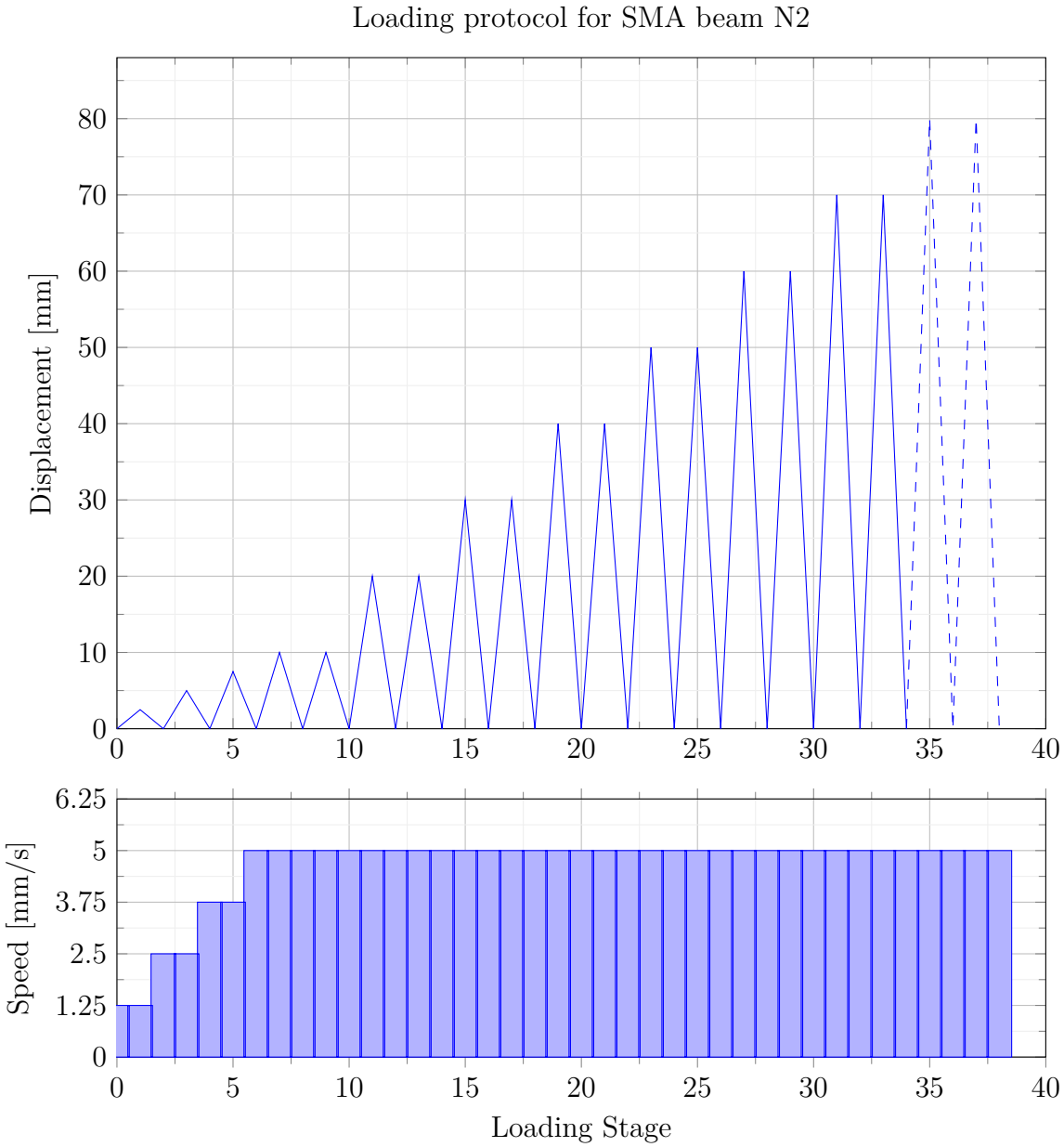


Figure 4.7: Loading Protocol 2

4.3 Steel properties

Two different rebar sizes are used, a diameter of 8mm for the stirrups and 12 mm for the longitudinal rebars. In table 4.1 are written the physical properties of these two rebars. The stress-strain relations are given in Fig. 4.8.

d_{bl}	f_y	f_u	ε_{sy}	ε_{su}	E_s
[mm]	[MPa]	[MPa]	[mm/mm]	[mm/mm]	[GPa]
8	538	664	0,0027	0,128	196
12	580	690	0,0029	0,113	199

Table 4.1: Steel rebar properties

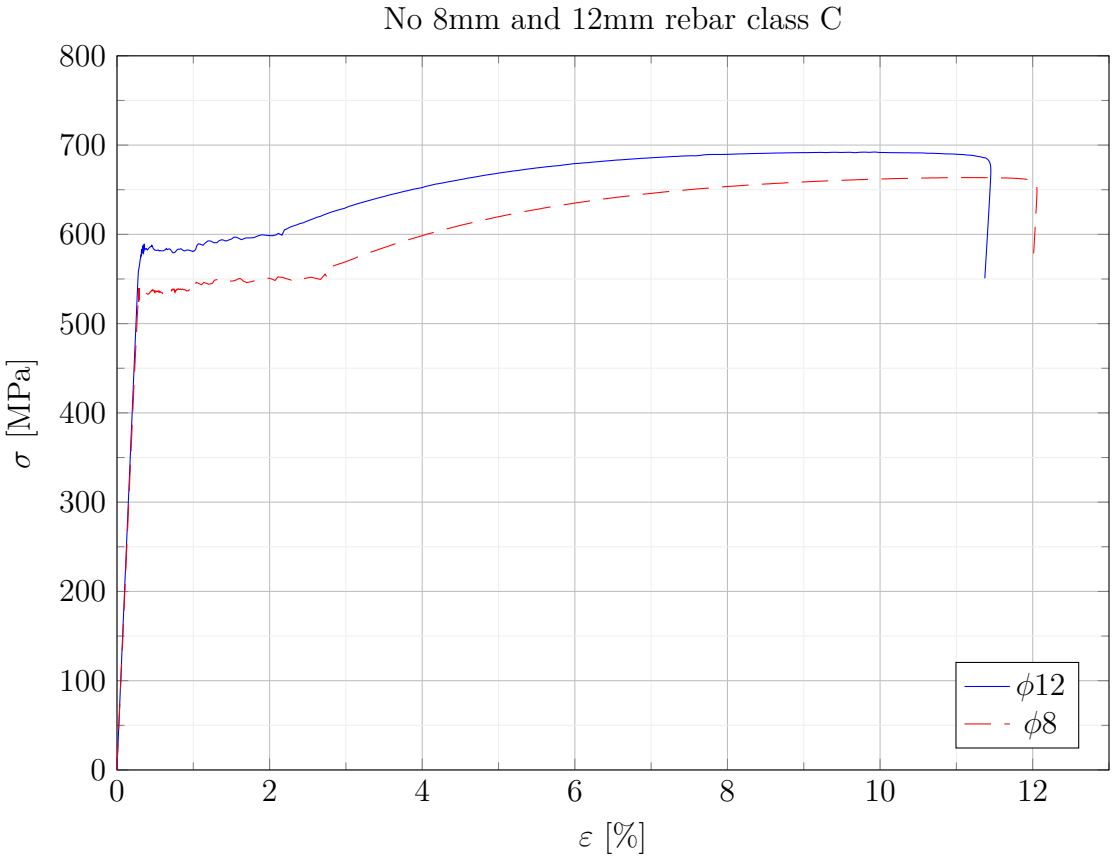


Figure 4.8: Typical strain-stress response of 8mm and 12mm steel reinforcement

4.4 SMA properties

Cyclic test on SMA is done by Almeida et al. [22] and the stress-strain response is given in Fig. 4.9.

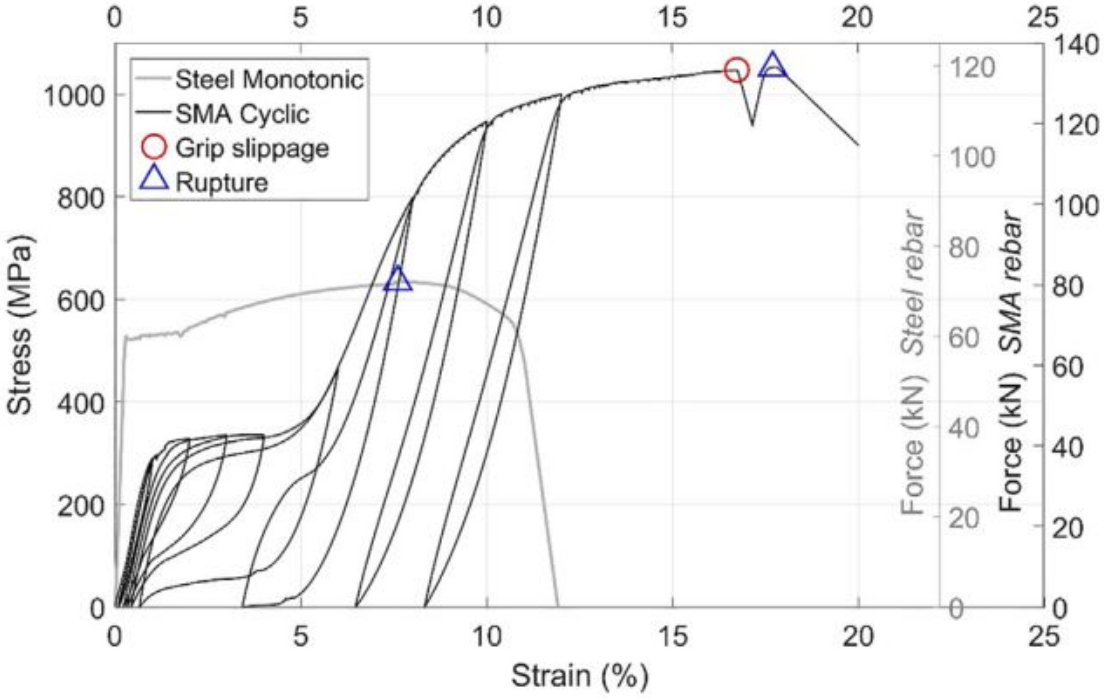


Figure 4.9: Stress–strain laboratory tests of steel rebar (monotonic) and SMA bar (cyclic, based on the displacement measured by the machine head) [22]

4.5 SMA-Steel welded connection

4.5.1 Process

The welded connections were done in the LaCAMi with a Friction Stir Welding (FSW) machine, following this process:

1. Prepare the rebars: cut SMA rebars of 13 [cm] and remove the lugs and the ribs of an ϕ16 steel rebar and remove materials up to the diameter of the SMA rebar (cf. Fig. 4.10).

2. Place the steel and the SMA in the FSW machine (cf. Fig. 4.11).

3. Make rotate the steel part at 1500 rpm and bring closer together the 2 rebars.

4. When the friction generates enough heat (a red circle is visible), the machine pushes the steel part up to 15 mm into the SMA. The faster this operation is done, the better the welding connection will be (cf. Fig. 4.12 and 4.13).

5. Once this is done, the other side of the weld must be done, the operations are the same, but in order to be able to put the weld into the machine's clamping system, the lab technician has to plane the weld bead.

6. Once the second welding is done, the beads are removed (cf. Fig. 4.14).



Figure 4.10: Step 1



Figure 4.11: Step 2



Figure 4.12: Step 4

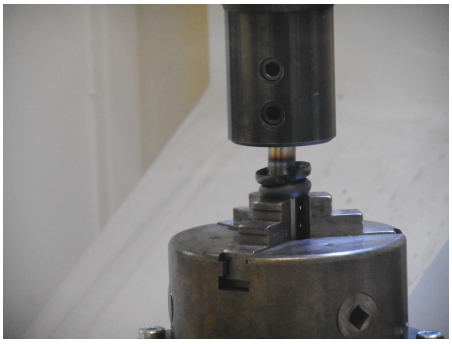


Figure 4.13: Step 5



Figure 4.14: Step 6

4.5.2 Properties

These connections were tested by Leezack et al [21], experimental results of uniaxial tensile monotonic tests are given in Fig. 4.15.

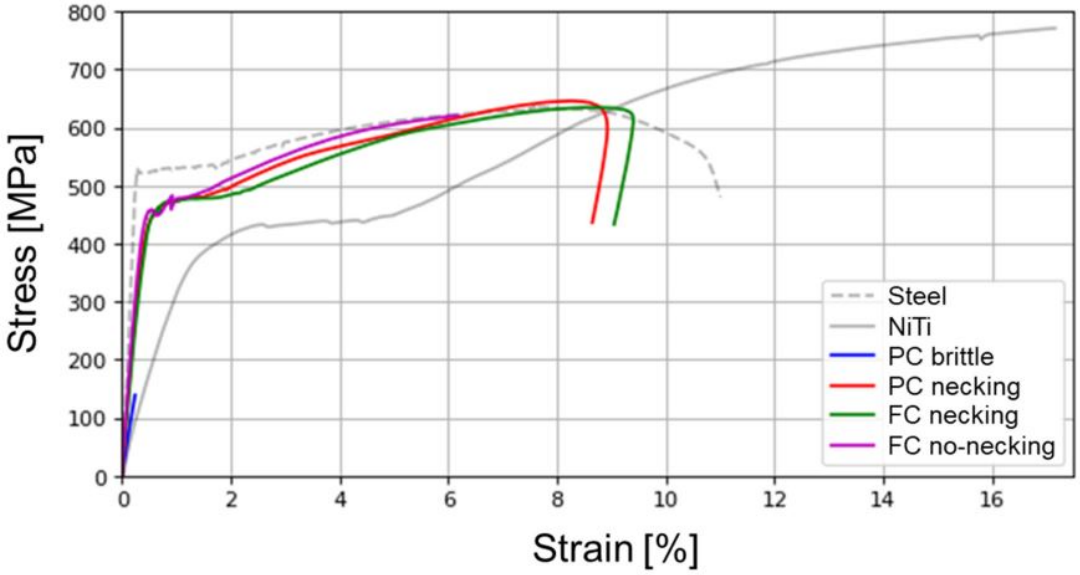


Figure 4.15: Tensile response of 'PC brittle', 'PC necking', 'FC necking' and 'FC no necking' welded samples in contrast with the base material tensile curves; 'PC brittle' sample breaks at low stress and low strain, in the elastic regime. Oppositely, both 'PC necking' and 'FC necking' samples show the same behaviour and fail by necking at a strain corresponding to the crossing of the base materials tensile curves, around 9% strain [21]

4.6 Concrete properties

During the casting of the beams, cubes and cylinders were cast to test the physical properties of the concrete. The size of the aggregates is between 7mm and 14mm. Standard 150 [mm] cubes and 150 [mm] x 300 [mm] cylinders were cast with the specimens to obtain the compressive strength and the splitting strength and were tested in the lab on the same day as the beams were tested.

		Beam S1	**Beam N1 and N2**
Tensile test 1	[Mpa]	2.76	3.66
Tensile test 2	[Mpa]	/	3.38
Tensile test 3	[Mpa]	/	3.34
Cylinder compressive test 1	[Mpa]	34.4	32.7
Cylinder compressive test 2	[Mpa]	/	32.4
Cylinder compressive test 3	[Mpa]	/	31.8
Cube compressive test 1	[Mpa]	37.5	44.6
Cube compressive test 2	[Mpa]	/	45.5
Cube compressive test 3	[Mpa]	/	40.9

4.7 Instrumentation

4.7.1 Optical fibre

Strains and Temperature sensors

Optical fibre is used as sensor since its use in telecommunication, it has lots of pros, it's linear, flexible, non electrical and can be embedded in RC structures to give information inside the concrete. One optical fibre sensor can provide thousands of strain or temperature measurements per meter. Quasi continuous profile in real time, fast measurements, high sensibility and establishment of a map of strain / temperature are advantages of this technology. This technology has a lot of advantages in comparison with classical measurement tools and it's why it is used in this master thesis. The technology is based on the

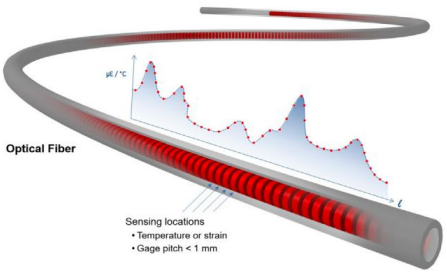


Figure 4.16: High definition distributed fibre [81]

Rayleigh scattering physical phenomena. It occurs when inhomogeneities in the core of the optical fibre smaller than the light wavelength is on the path of the light. At first, the Rayleigh diffusion is stored as reference. After, when the optical fibre is subject to stress or temperature variation, measurements are made. The data is transformed from the space domain to the frequency domain using the FFT (Fast Fourier Transform). The change in deformation or stress can be found by comparing the initial and disturbed states.

In a paper published by Berrocal et al. [82], interesting results that can be obtained with optical fibres on a three points bending RC beam are described. They managed to obtain the strains, the detection of crack formation, the crack location and the crack width evolution over time. To confirm the results obtained by the optical fibre, they compared the results of the optical fibres and the results measured by traditional equipment (foil gauge and DIC), they were in excellent agreement.

Installation

The installation of the optical fibres on the reinforcing bars was as follows:

1. Dig a trench on a rebar with a Dremel 4000 (cf.. Fig 4.17, 4.18 and 4.19)
2. Wash the trench (sandpaper+ Degreaser + M-Prep Conditioner A (contains acid) + M-Prep Neutralizer 5A)
3. Put the optical fibre in the trench
4. Glue it at points and use activator (cf. Fig. 4.20)
5. When everything is well placed, glue all
6. Wait for glue to dry
7. Put epoxy on it to protect the optical fibre, which will almost not affect the contact between concrete and reinforcement (cf. Fig. 4.21).
8. Save gauges, to know the exact location of important points (ie. middle of the rebar, welded connection between SMA and steel,...)
9. Prepare the connection's protections (funnel, tube) (cf. Fig. 4.22)
10. The rebar is ready to be used in a cage rebar



Figure 4.17: Step 1



Figure 4.18: Step 1



Figure 4.19: Step 1

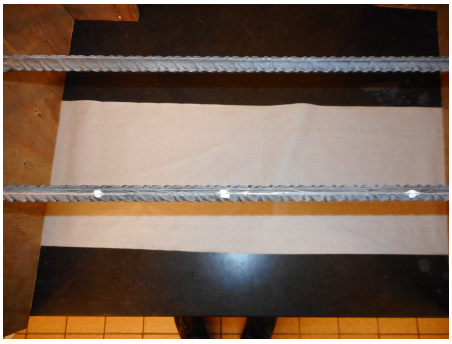


Figure 4.20: Step 4

The following measurement tools are used to evaluate the evolution of the beam (displacement, strains and temperature).

Optical fibre: As explained, these fibres can measure the strains and the temperature. In the classical RC beam strain sensors on the bottom side of the bottom longitudinal rebars are placed. In the SMA RC beams, strain and temperature sensors on the bottom side of the bottom longitudinal rebars are installed. The strain sensors were 5 meters long, so were used by running back and forth along the beam, whereas the temperature sensors were 2 meters long, and were used along the length of one rebar. The location of optical fibres in beams is sketched in Fig. 4.23 and 4.24 for the RC classical beam and for the SMA beams respectively.

4.7.2 Others

DIC: Digital Image Correlation is an optical technique for determining the strains in concrete. Black dots are painted on the beams, and due to the deflection of the beam, points will slightly change their position. With the movement, a dedicated



Figure 4.21: Step 7



Figure 4.22: Steps 9-10

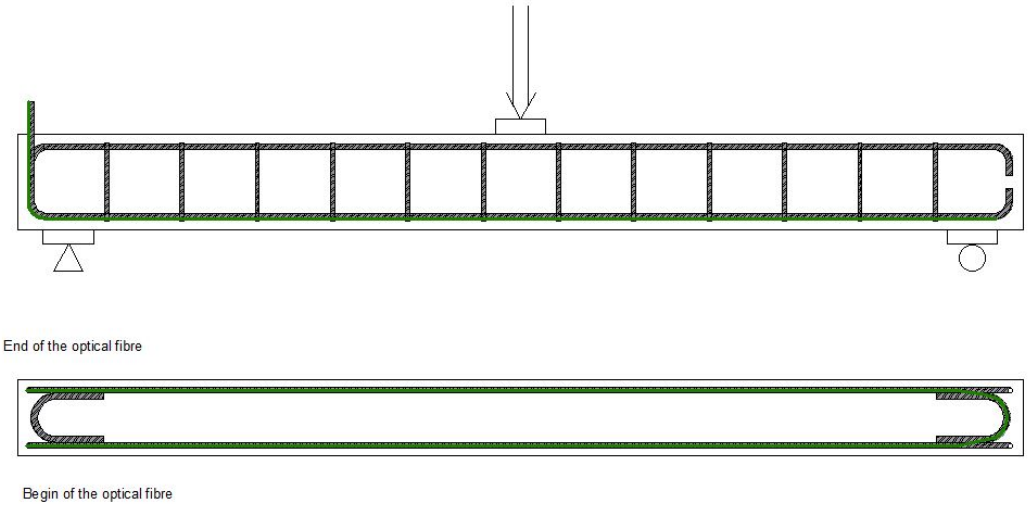


Figure 4.23: Optical fibre in the classical RC beam (Strains)

software will calculate the strains.
Laser: A laser will also be placed on the ground to measure accurately the vertical displacement of the bottom of the beam. This displacement is taken as a reference for the loading protocol and used for the Force-Displacement response.

The setup is sketched in Fig. 4.25 and a picture of the setup in the lab is in Fig. 4.26.

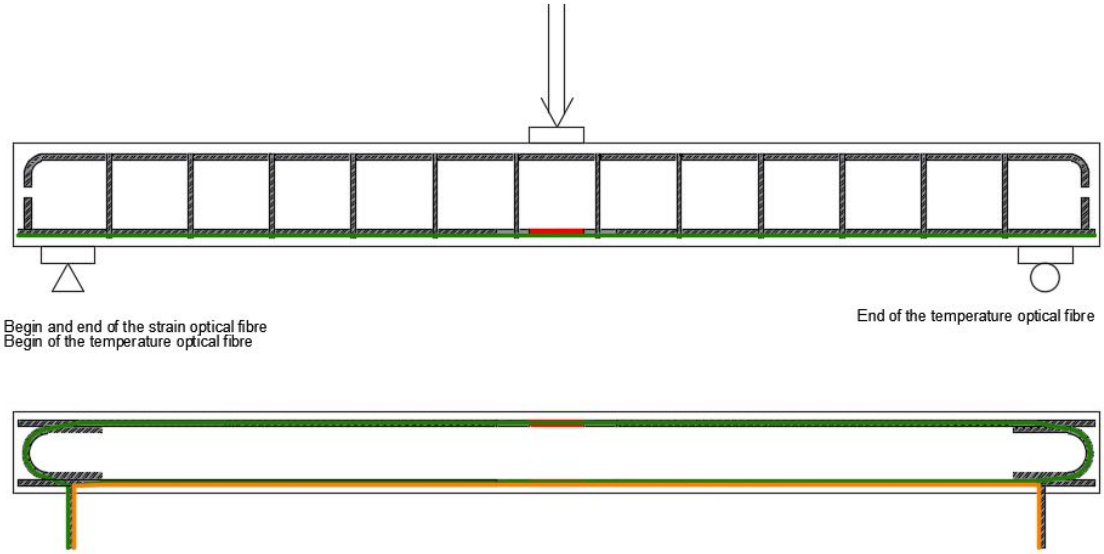


Figure 4.24: Optical fibre in SMA RC beams (Strains and Temperature)

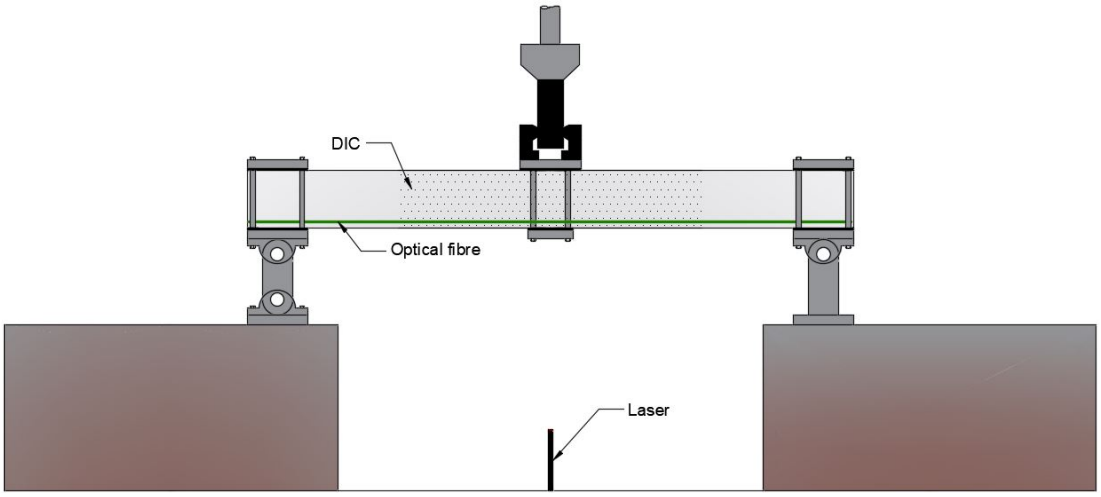


Figure 4.25: Experimental setup and measurements tools

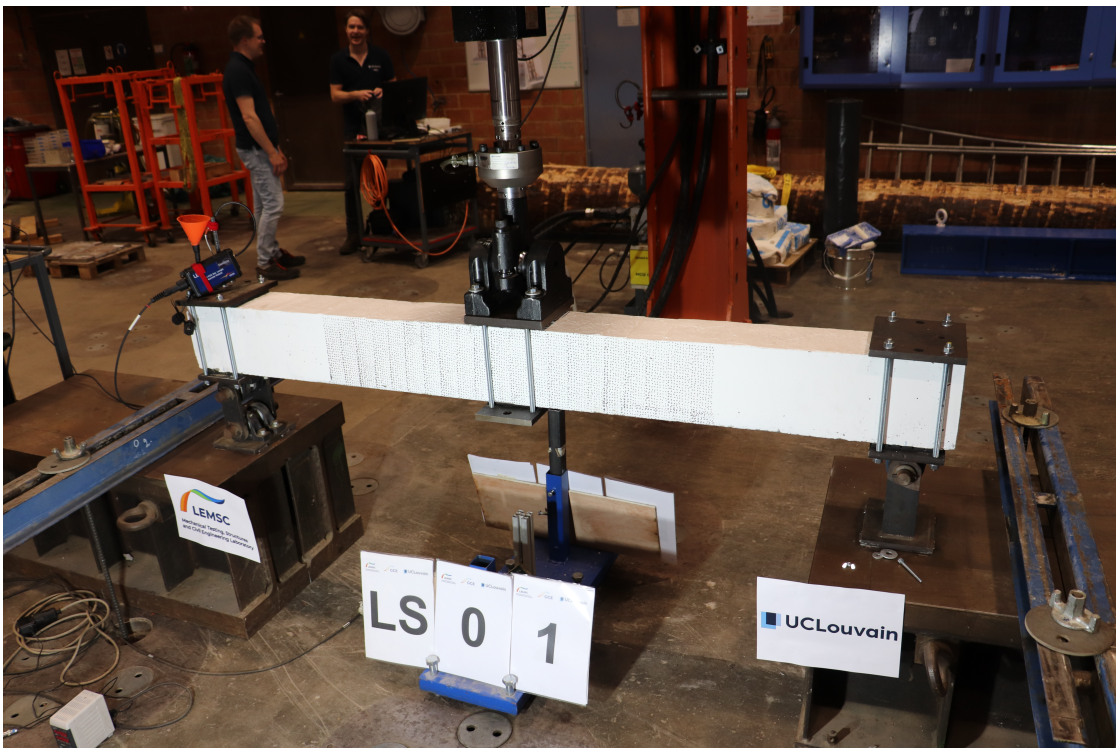


Figure 4.26: Picture of the experimental setup

CHAPTER

5

RESULTS AND ANALYSIS

Pictures of the tests of the beams are available in Appendix B.

5.1 Beam S1

5.1.1 Load-Displacement response

In Fig. 5.1, the Load-Displacement response of the first beam, the control beam, is represented. the maximal applied force is 45.2 [kN].
After the two peaks loading up to 70 [mm], the loading stage imposed a beam displacement of 76 [mm] rather than up to the failure of the beam as programmed in the software governing the jack because a maximal jack's stroke was implemented in the software, and this stroke was equivalent to a displacement of the beam of 76mm. After solving this problem, the beam was loaded up to a displacement of 100 [mm], the physical maximal stroke of the jack. Since the beam was still not broken, the setup had to change in order to modify the jack location to allow a greater stroke. So, the next day, lab technicians changed the setup of the jack and the beam was tested with a quicker loading protocol (1mm/s) up to 70 [mm] and then up to failure (now that the jack's stroke is long enough), one longitudinal bottom rebar broke. This second loading is represented in red and can be seen by

the change of stiffness of the beam.
During the loading stages going to 0 [mm] displacement, after large displacements, it was possible to see the bottom longitudinal rebars buckle. On the graph, this phenomenon can be seen on the left bottom side.

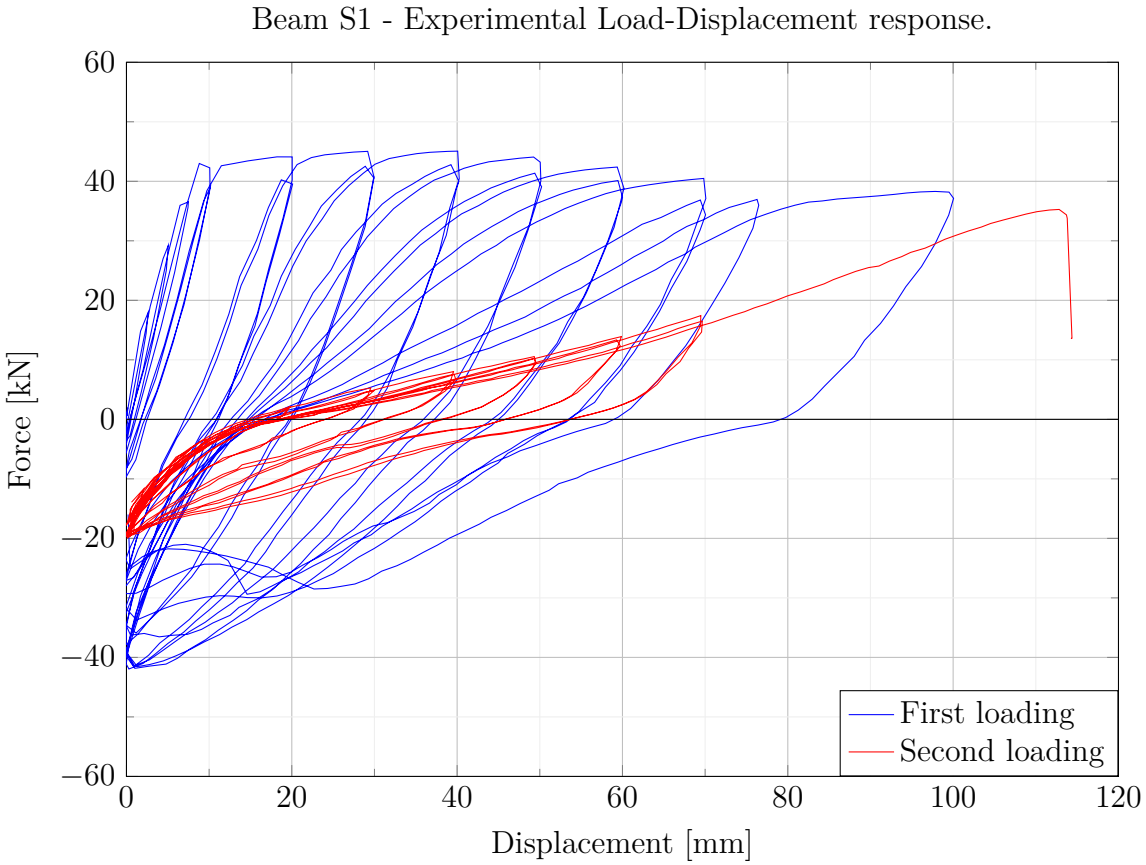


Figure 5.1: Load-Displacement response of beam S1

5.1.2 Recovered displacements

Figure 5.2 shows the residual displacements of beam S1 as a function of the maximal displacement. Two zones are noticeable, the first one, before the yielding, the beam behaves in the elastic domain (when maximal displacements are smaller than 10 mm), so the residual displacements are small and don't increase much with the maximal displacements. In the second zone, after the yielding of the steel, the residual displacements increase linearly. A linear approximation that fits well is represented on the graph.

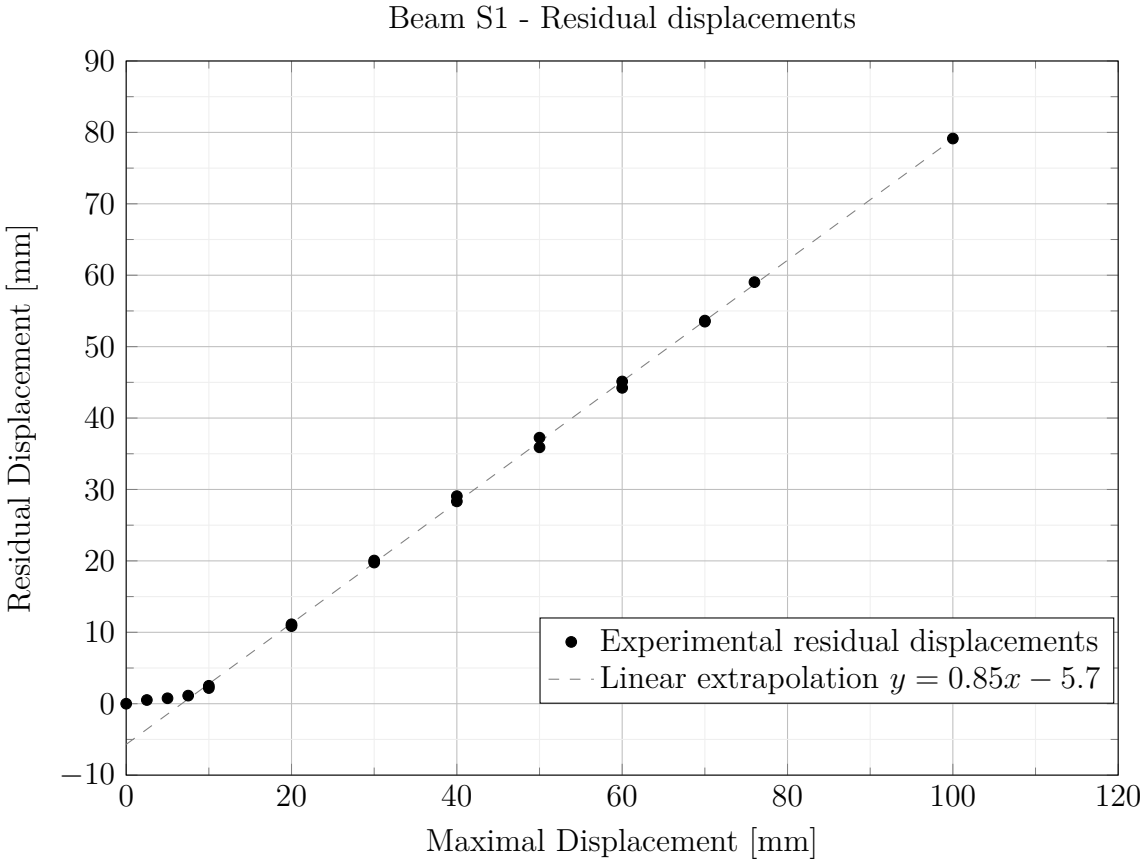


Figure 5.2: Residual displacements of beam S1

5.1.3 Strains

The strains at LS01-LS09 (uneven LS) are represented in Fig. 5.3 corresponding to a displacement up to 10 [mm] of the mid-span of the beam. After LS07, data began to become unreadable, values *"null"* are recorded. And for the clarity of the graph, values above $50000 \mu strains$ are cut because they are not the real strains but an error of measurements.

The loading protocol of the last beam was determined thanks to the strain rate of the first beam (S1, at quasi-static rate) obtained with the optical fibres at the middle of the two longitudinal rebars in Fig. 5.4 (G2 and G5 correspond to gauges in the optical fibre at the exact location of the middle of each longitudinal rebar). The mean value of the strain rate applied is $\dot{\varepsilon} = 0.79 \times 10^{-3}/s$. The loading rate had to be increased in order to have the strain rate within the earthquake's range. Assuming that the increase of the loading rate of the actuator is proportional to the increase of the strain rate in the bars, a loading rate faster than the first loading

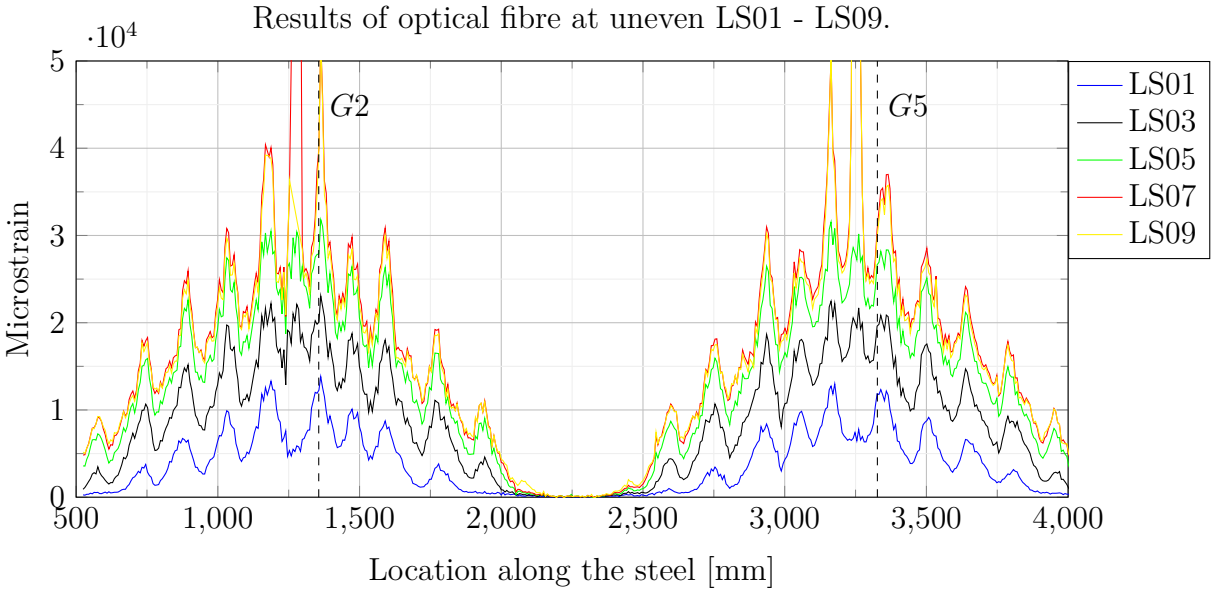


Figure 5.3: Strains in the steel at different Load Stages

rate between 1.3x bigger and 100x bigger must be applied to have a strain rate comparable to an earthquake.

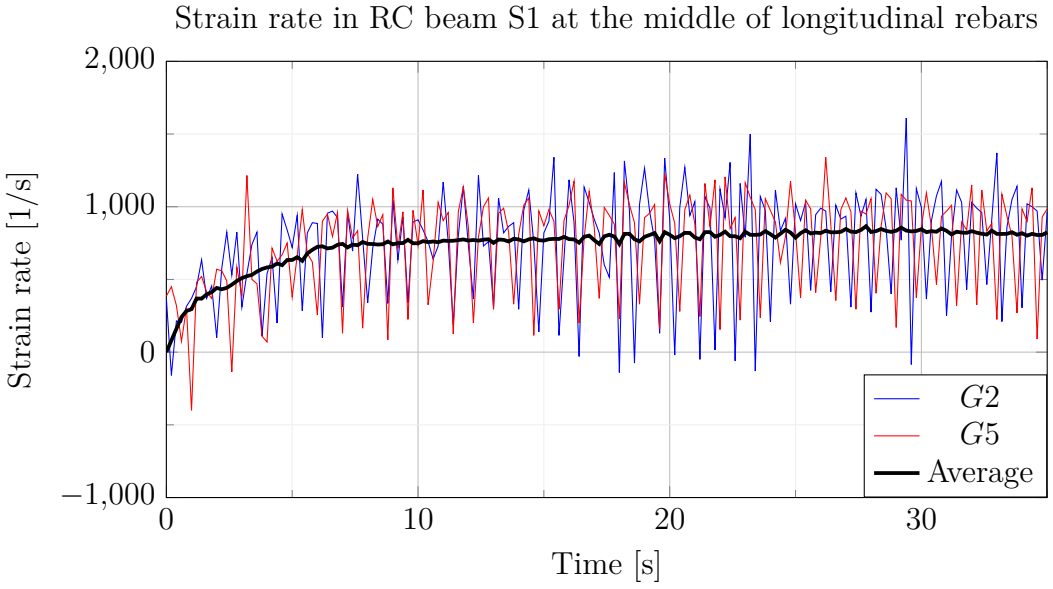


Figure 5.4: Strain rate in beam S1 during Load Stage 07

5.1.4 Cracks

Due to the effort of the jack on the beam, the beam deforms and cracks appear in the concrete. For the first beam, the experimental setup used had rubber between the central steel plate and the beam, and it obstructed the complete development of a big crack in the middle of the beam. Instead, bigger cracks appear next to the central steel plate. Three main cracks appeared in the middle of the beam, other cracks didn't really grow with the load stage but remained quite constant. The cracks location is sketched in Fig. 5.5, and its evolution with respect to the load stage (i.e. maximal displacement) is represented in Fig. 5.6.

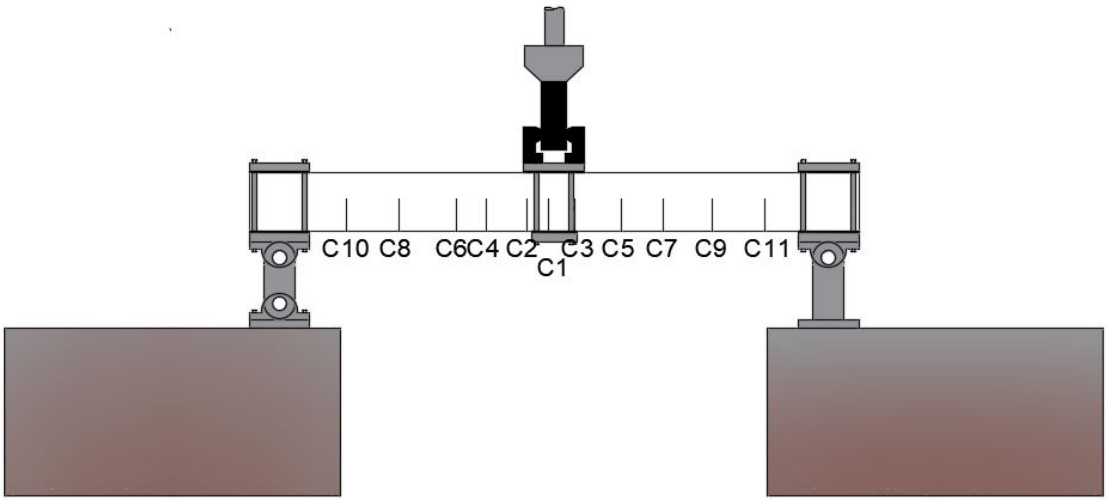


Figure 5.5: Beam S1 - Cracks location

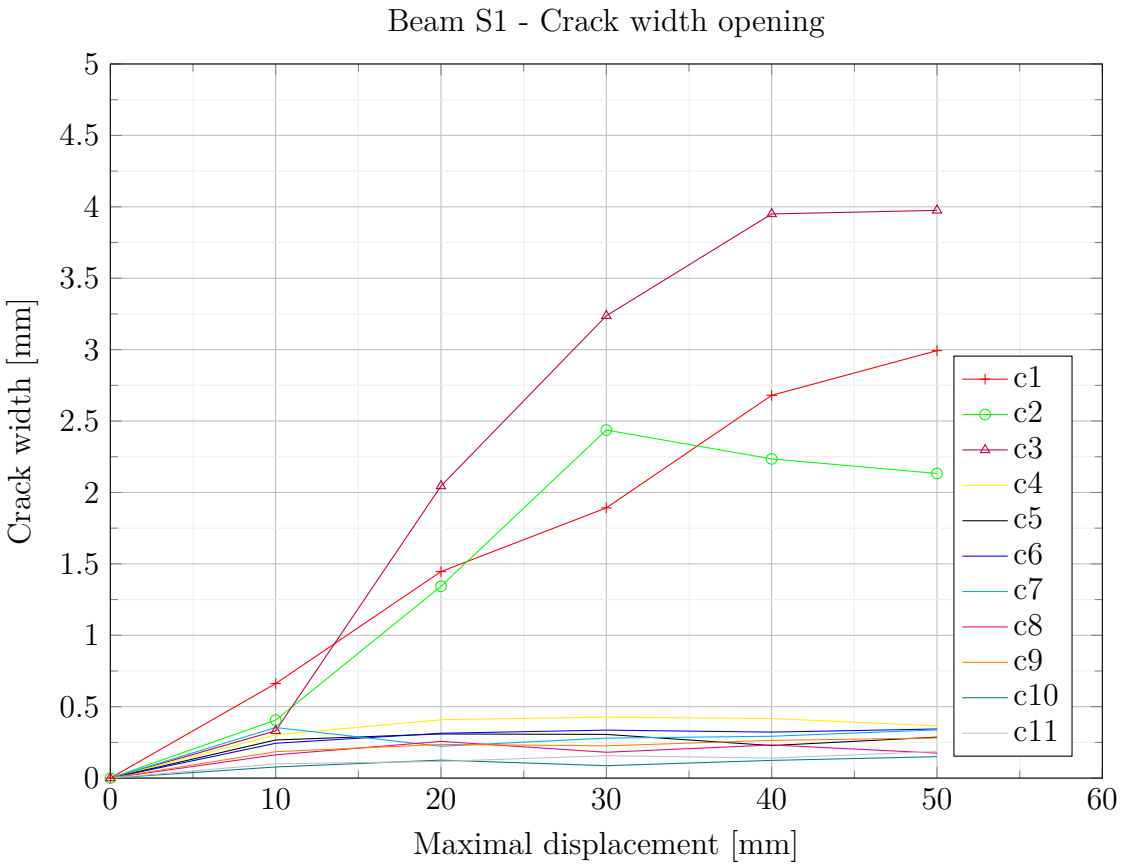


Figure 5.6: Beam S1 - Crack width opening

5.2 Beam N1

The first SMA beam is tested at quasi-static rate and due to a brittle failure of the welded connection between steel and SMA, the beam failure occurred at the third Load Stage. This early failure affects the analyses to do and the quantity of data to analyse.

5.2.1 Load-Displacement response

The Load-Displacement curve is given in Fig. 5.7. The maximal applied force is 17.3 [kN] and the failure of the beam occurs at a displacement of 2.6 [mm] during Load Stage 03. The jack continued to push the beam after the failure of the welded connection up to Load Stage 07. As drawn on the graph, after failure, the applied force is very small.

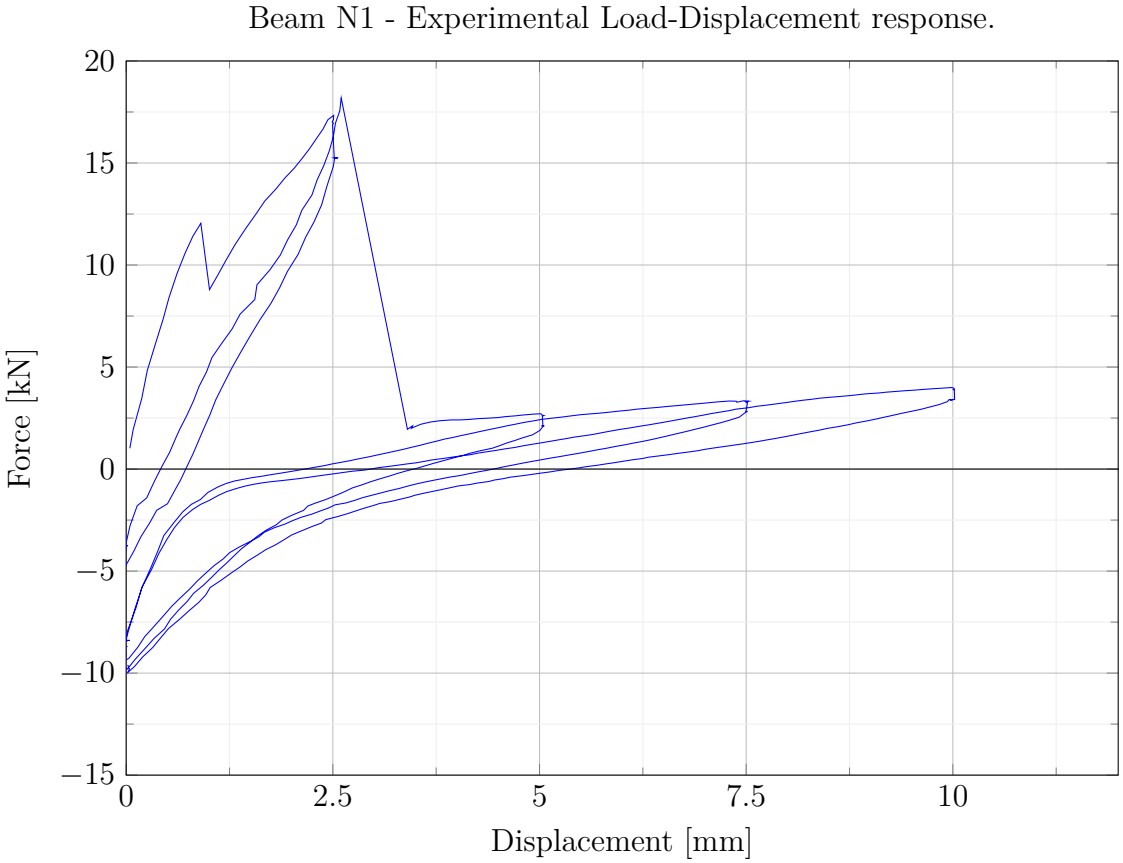


Figure 5.7: Load-Displacement response of beam N1

5.2.2 Recovered displacements

A graph showing the recovered displacements of beam N1 is represented in Fig. 5.8. Due to the premature rupture of the beam, the first load stages only gave reliable information, the residual displacements after 2.6 [mm] displacement were not consistent because the rupture in the longitudinal rebars already occurred. For the first load stages, a similar residual displacement to Beam S1 is observed.

5.2.3 Strains

After the rupture of the welded connection, the strains also broke and thus information after the rupture is not usable. On the following graph in Fig 5.9, the strains after the first Load Stage and just before the failure of the connection all along the beam are represented.

The strains are very concentrated at the location of the SMA. This is a good

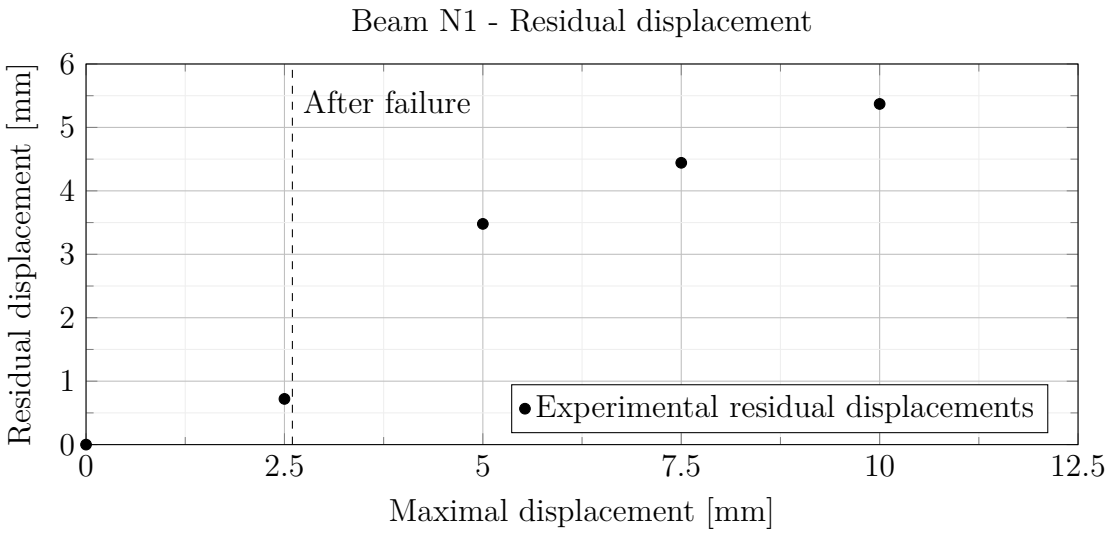


Figure 5.8: Residual displacements of beam N1

result that the author wanted to have. Big strains in the SMA mean that the SMA is taking all the deformations and thus leads the response of the RC structure. The evolution in time of the strains in a SMA rebar is represented in Fig. 5.10. When the failure occurred, the strains instantaneously dropped near to 0. What seems to be residual strains are in fact displacements of the optical fibre sensor that is interpreted by the sensor as strains but aren't.

5.2.4 Cracks

Several cracks developed along the beam, one central crack appeared during the first Load Stage. But the crack width wasn't measured due to premature failure of the beam.

5.2.5 Temperature

One important feature of the beams with SMA was the use of temperature sensors along the steel and the NiTi.
Unfortunately, the recorded values are not usable because they are very noisy and large differences in temperature measurements ($\simeq 20°C$) are recorded at 0.65 [mm] intervals. So the data is therefore not shown in this chapter, but due to the untimely failure of the beam, the SMA rebars did not have time to heat up.
Furthermore, when mechanical deformation is added to temperature variation, it

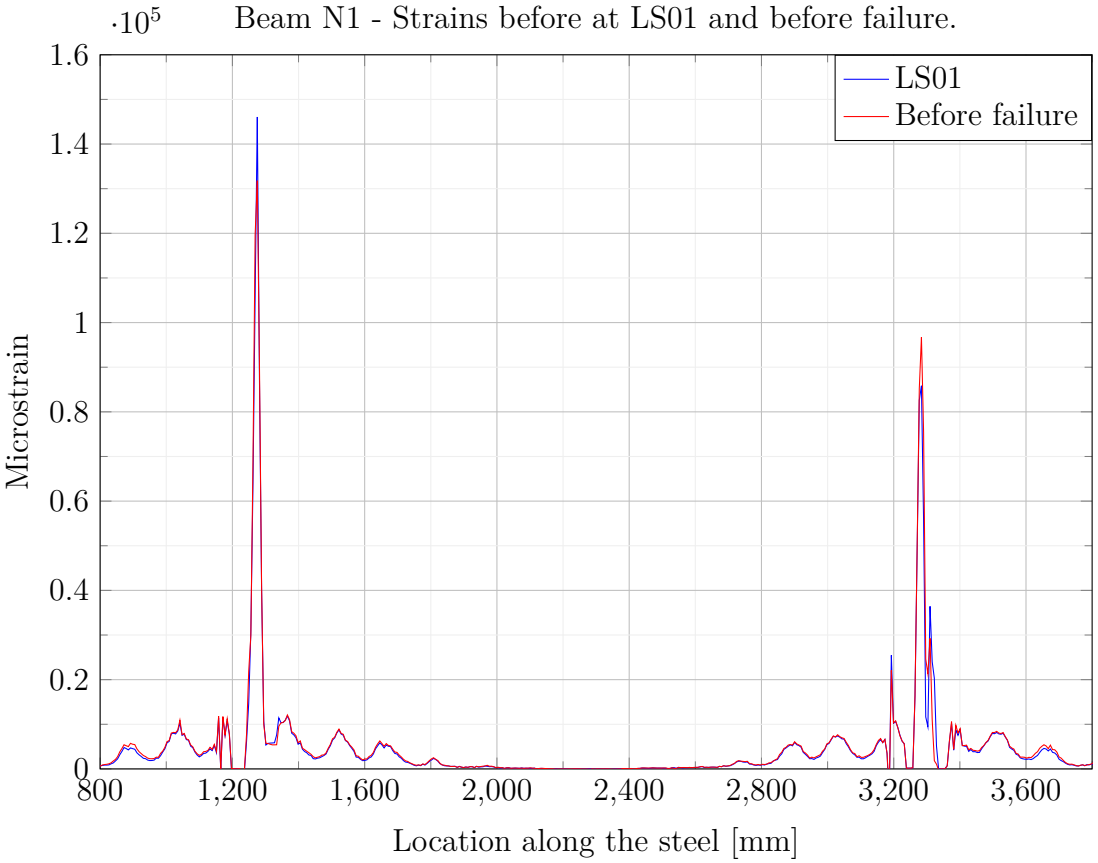


Figure 5.9: Beam N1 - Strains in the longitudinal bottom rebars at LS01 and before failure.

will lead to false measurements because the sensor will record the deformation as a temperature variation. For beam N2, the same problem occurred, the data can't be used.

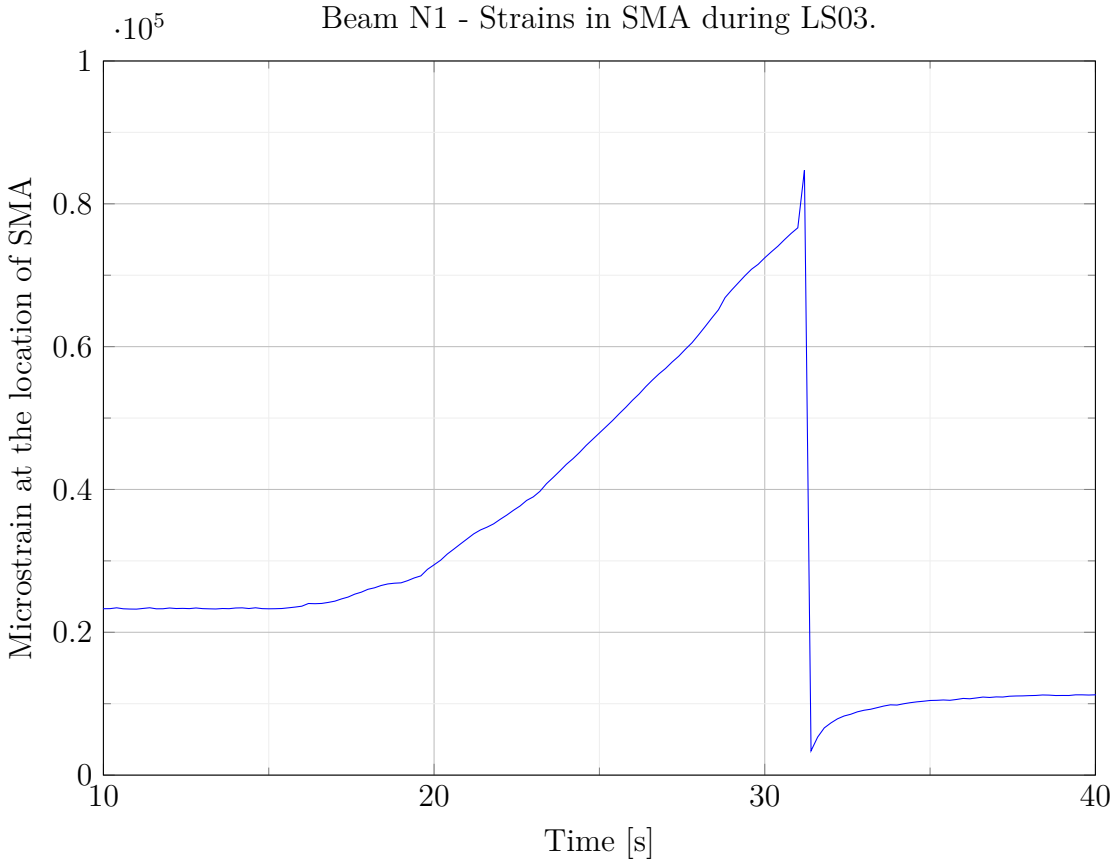


Figure 5.10: Beam N1 - Strains during the load stage of the failure at the location of SMA rebar.

5.3 Beam N2

This beam was supposed to be tested at a quick loading protocol in order to have a strain-rate comparable to what happens during seismic events. But due to the early failure of the first beam, this beam was tested at quasi-static rate also, in order to have data to compare with the RC beam. Unfortunately, this beam failed at the same load stage as N1. Thus the data obtained is limited to the first three load stages.

5.3.1 Load-Displacement response

The Load-Displacement curve is given in Fig. 5.11. The maximal applied force is 17.5 [kN] and the failure of the beam occurs at a displacement of 2.8 [mm] during Load Stage 03. Beam N2 and Beam N1 have similar displacement-capacity and

maximal applied force.

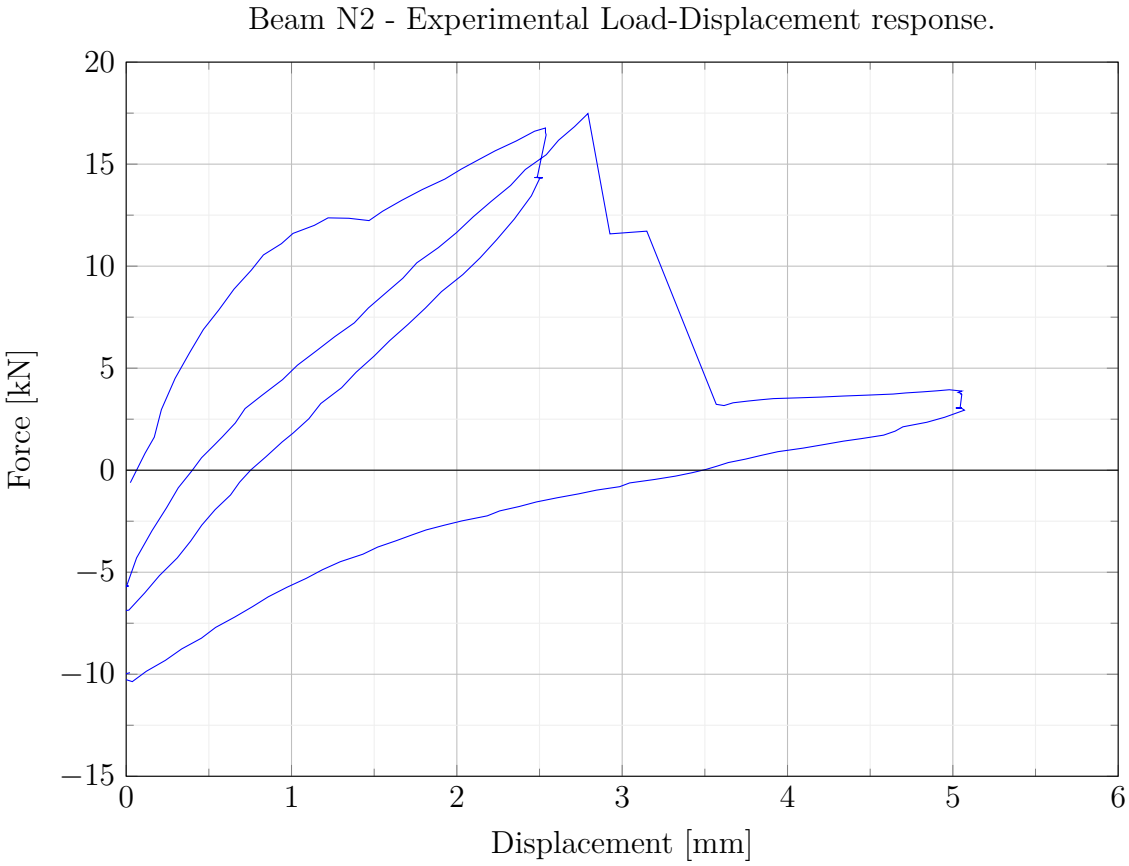


Figure 5.11: Load-Displacement response of beam N2

5.3.2 Recovered displacements

As mentioned for beam N1, only one residual displacement is measured, after a displacement of 2.5mm. A graph showing the residual displacements in function of the maximal displacement is given in Fig. 5.12.

5.3.3 Strains

The strain sensor broke during LS02 when the beam went back to its original position so no strain data after this Load Stage (including during the failure of the welded connection) was recorded. The strains recorded for beam N2 during the first Load Stage are very similar to the strains of beam N1. The graph is shown in

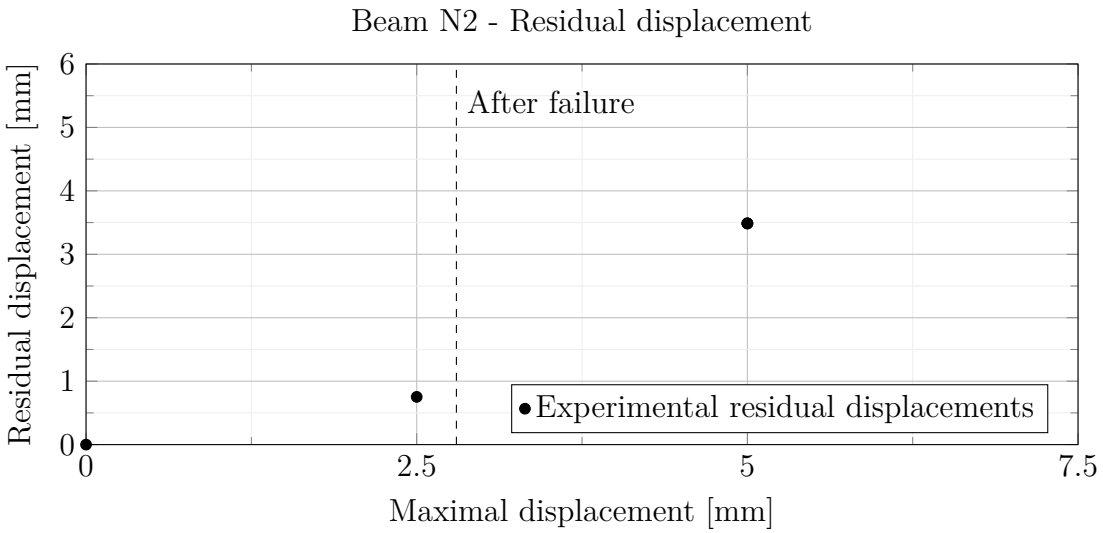


Figure 5.12: Residual displacements of beam N2

Appendix C.

5.3.4 Cracks

Several cracks developed along the beam but were not measured due to premature failure of the beam.

5.4 Numerical results

5.4.1 Beam S1

The numerical Load-Displacement curve of this RC beam is given in Fig. 5.13. According to VecTor2, the maximal and minimal applied force is 59.2 [kN] and -42.8 [mm] and the maximal displacement before failure is 37 [mm].

The numerical analysis of the maximal applied force is pursued with two other software. Response-2000 (Response-2000 is a sectional analysis program that can calculate the strength and ductility of a RC cross-section subjected to shear, moment, and axial load) [83] and with a simple SeismoStruct model (SeismoStruct is a Finite Element package capable of predicting the large displacement behaviour of space frames under static or dynamic loading, taking into account both geometric nonlinearities and material inelasticity) [84]. The maximal forces obtained for the

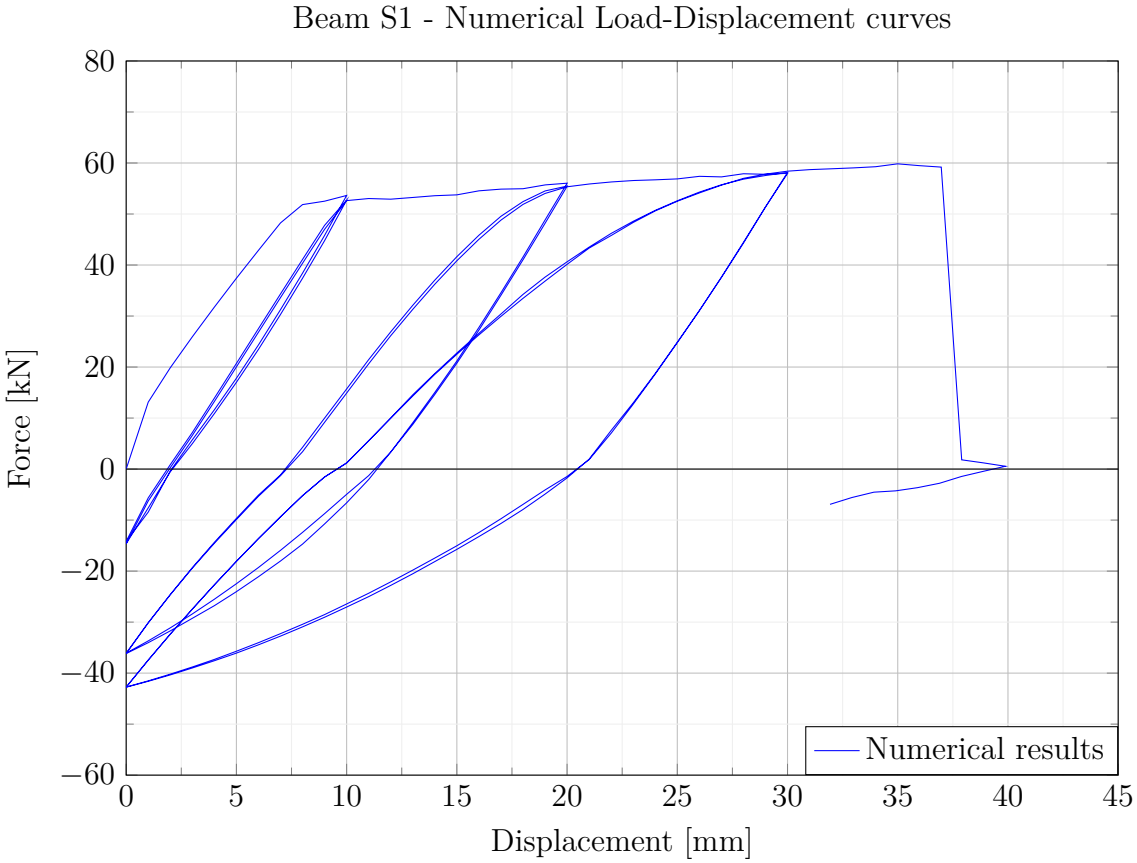


Figure 5.13: Beam S1 - Numerical Load-Displacement response

Beam S1 are 47.6 kN and 59kN for Response2000 and SeismoStruct respectively. Response2000 gives a smaller force compared to VecTor2 and SeismoStruct but this value is closer to the experimental applied force (45.2kN).

The numerical residual displacements of Beam S1 are given in Table 5.1.

Maximal Displacement [mm]	10	10	20	20	30	30
Residual Displacement (Numerical) [mm]	2.1	2.1	11.4	11.3	20.5	20.4

Table 5.1: Beam S1 - Numerical residual displacements

5.4.2 Beam N1

The numerical simulations ran with VecTor2 give the Load-Displacement response given in Fig. 5.14. In this model, the maximal displacement of the beam is 50 [mm], and the maximal and minimal forces are 56.5 [kN] and -35.3 [kN]. Response-2000, which gave results closer to the experimental results, obtained a maximal force of 49.6 [kN]. Once again, maybe VecTor2 gives an overestimate maximal force and the result given by Response-2000 is closer to the experimental test if no brittle failure occurs.

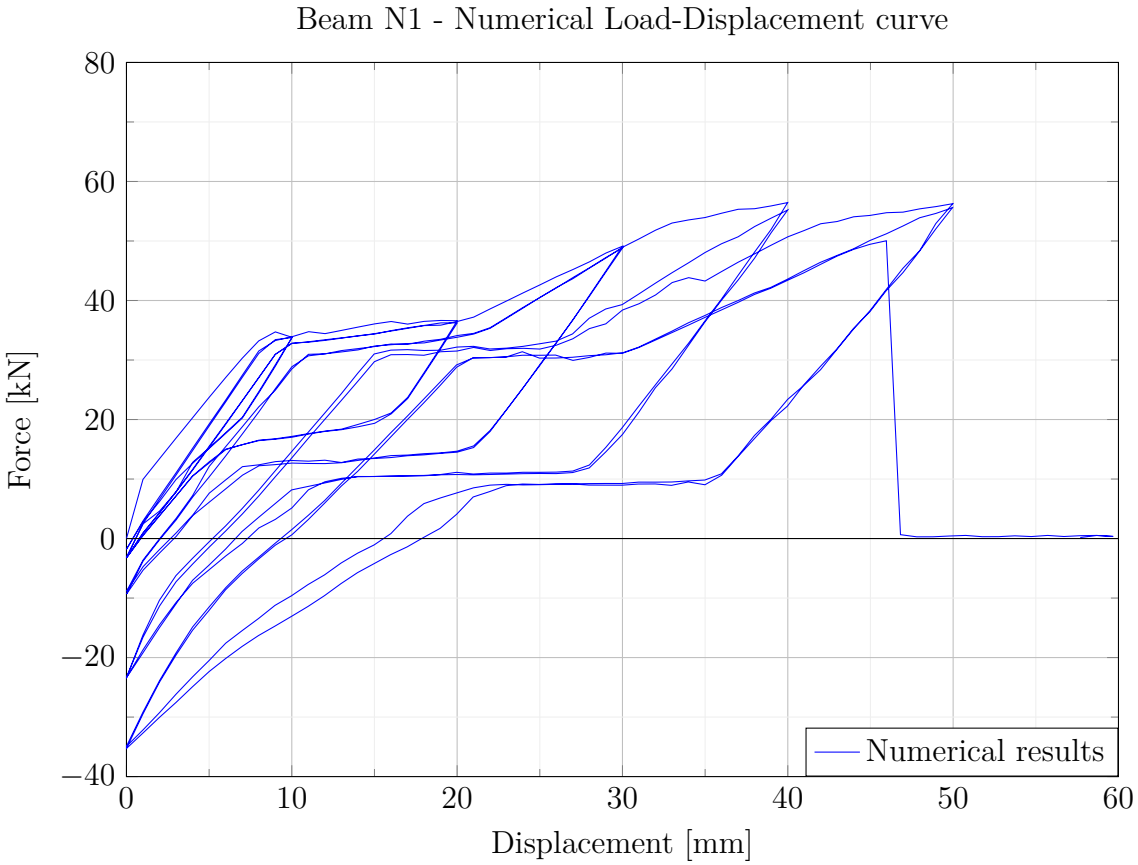


Figure 5.14: Beam N1 - Numerical Load-Displacement response

The numerical residual displacements of Beam N1 are presented in Table 5.2.

Maximal Displacement [mm]	10	10	20	20	30	30	40	40	50	50
Residual Displacement (Numerical) [mm]	0.6	0.4	0.9	0.9	2.9	2.7	6.6	7.3	17.9	15.6

Table 5.2: Beam N1 - Numerical residual displacements

5.5 Overall comments

Due to the brittle failure of the connection between the steel and the NiTi, conclusions for beams N1 and N2 in terms of ductility, residual displacements, cyclic behaviour or cracks width are impossible and comparison with the control beam is limited to the early load stages.
The first load stages of every beam can nevertheless be compared. From the Load-Displacement viewpoint, the three beams have similar behaviour as represented in Fig. 5.15.

The graph in Fig. 5.15 shows that the two SMA beams have a comparable initial stiffness higher than beam S1. Indeed, the stiffness of beam S1 is half the stiffness of the beams N1 and N2, with a value of 8337kN/m, 18665 kN/m and 15117kN/m for S1, N1 and N2 respectively.
Other points that can be compared are the maximal and minimal force applied for these beams, the maximal force is fairly the same, 18.75kN, 17.34kN and 16.77kN for S1, N1 and N2 respectively. But the minimal force, the applied force to bring the beam back to its original shape (to 0 [mm] of displacement), is different, -2.54kN, -4.76 kN and -6.91 kN for S1, N1 and N2 respectively. The two SMA beams have a more important force than the control beam. Maybe the new experimental setup is responsible for this change.
Another point to compare is the residual displacements of the three beams, they are very close to each other. Because it's still in the elastic response of the beams, the difference is still small at this Load Stage. But, it is interesting to note that the control beam has a smaller first residual displacement than the two SMA beams (0.51 [mm], 0.71 [mm] and 0.75 [mm] for S1, N1 and N2).

With the optical fibres, the strains in the steel and the NiTi for SMA beams are measured at the end of Load Stage 01. This allows the evolution of the strains to be seen in relation to the location of the beam reinforcement. The graph in Fig. 5.16 shows the strains at 2.5 [mm] displacement. The general curves look similar for the three beams except for the middle of the beams. The maximal values are really different. Strains of 13049, 145421 and 79800 microstrains for S1, N1 and N2 are recorded. The larger values of SMA beams are on the location of the SMA rebar. At the beginning of the tests, the SMA rebar drove the behaviour of the RC

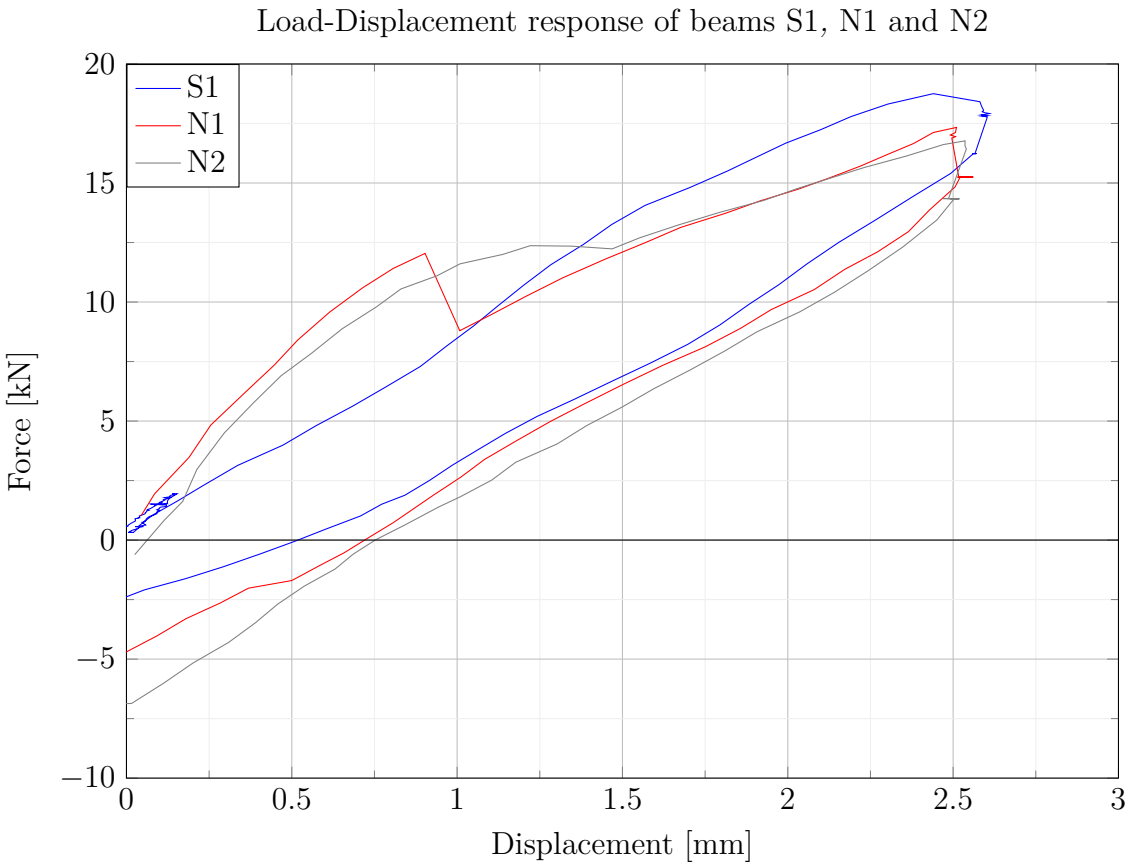


Figure 5.15: Comparison of the Load-Displacement Response of three beams for LS01 and LS02.

beam by concentrating all the deformation at the centre of the beam. This is an interesting feature that the author was aiming for before the test. Effectively, the objective of the use of SMA in RC structures is the concentration of deformations at one plastic hinge and the recovery of deformation after the removal of stress. For the three beams, the rest of the beam bent approximately the same way, as can be seen with the graph of strains.

The tension stress in the SMA rebars calculated with Response-2000, for a moment of 7.6 [kNm], corresponding to a force of 17 [kN] (applied force when the welded connection broke), is 147 [MPa] in the SMA chunks. This corresponds to the failure of a brittle connection as studied by Lezaack et al. [21], represented in Fig 4.15.

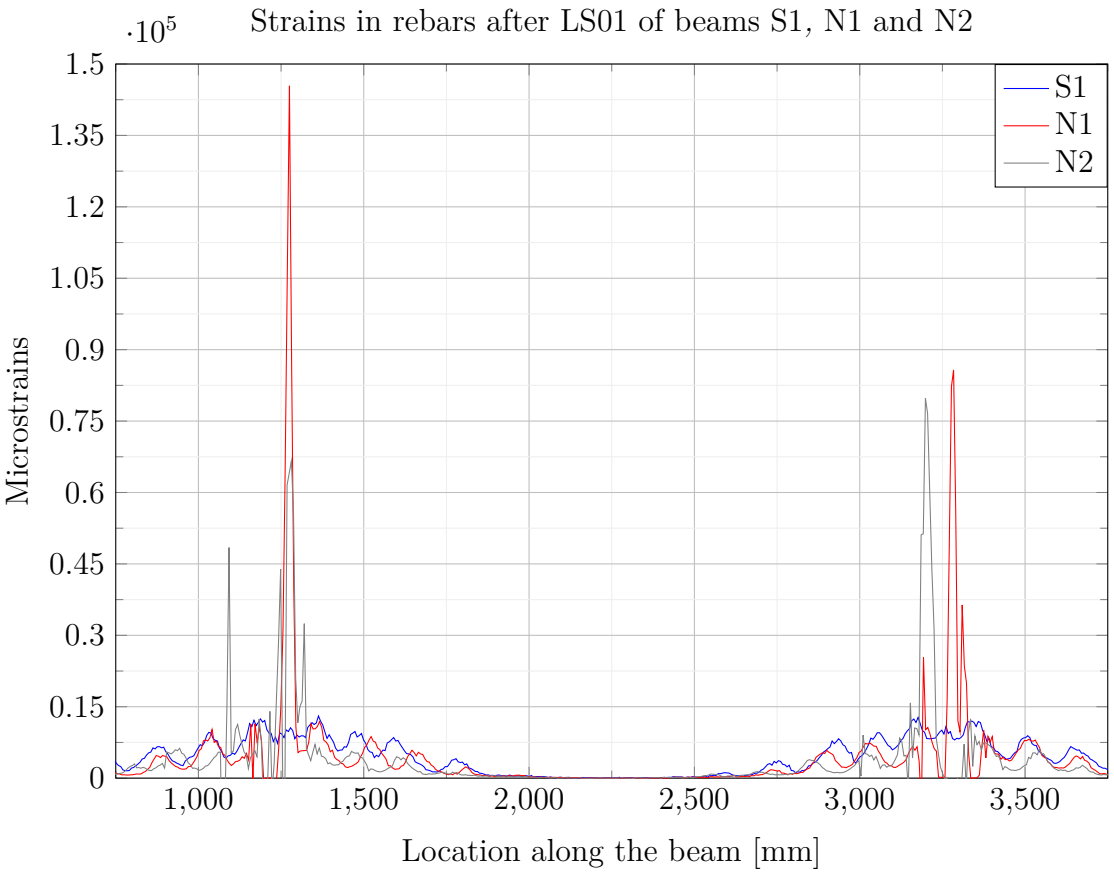


Figure 5.16: Comparison of the strains in the longitudinal bottom rebars of three beams for LS01.

CHAPTER

6

COMPARISON BETWEEN NUMERICAL AND EXPERIMENTAL RESULTS

In this chapter, are compared the results obtained experimentally, in terms of maximal displacements, maximal applied force, stiffness, recovered displacements,... and the results obtained numerically. The objective is that the numerical analysis gives results close to the experimental results.

One VecTor2 model was made for the control RC beam and one for the two SMA RC beams. As the loading rate (displacement-based) cannot be changed in VecTor2, it is assumed that the loading is quasi-static. Results obtained for the SMA beam model can therefore be associated with the beam N1, loaded at quasi-static rate.

6.1 Beam S1

6.1.1 Load-Displacement curves comparison

The Load-Displacement curve of this RC beam and the comparison with the numerical model are given in Fig. 6.1.

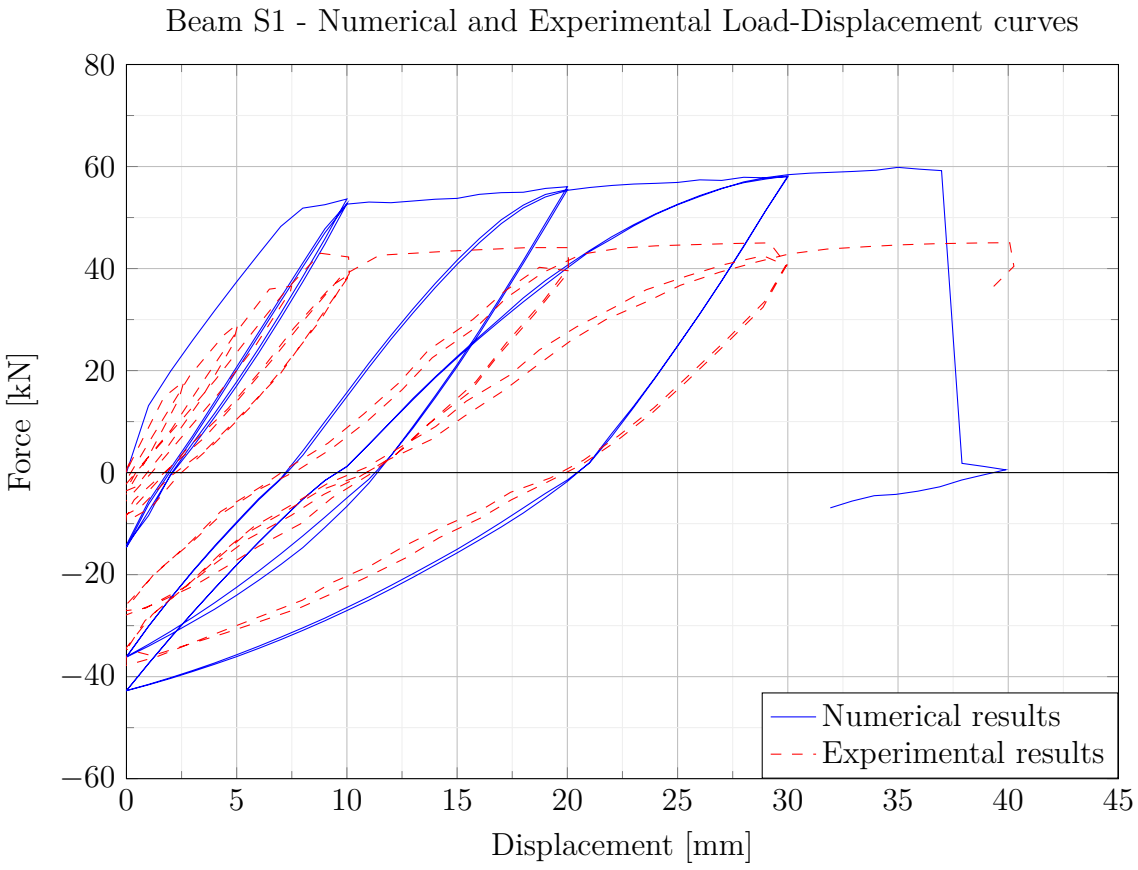


Figure 6.1: Beam S1 - Numerical and experimental Load-Displacement response

6.1.2 Residual displacements comparison

Before the failure of the numerical model of the beam, the residual displacements match very well with the experimental values. These experimental and numerical values are summarised in Table. 6.2. VecTor2 is a software dedicated to calculating RC structures, so it's quite logical that with a good model, the behaviour of the beam is well approximated.

	Maximal Force [kN]	Minimal Force [kN]	Initial Stiffness [kN/m]
Numerical Model (VecTor2)	59.9	-42.8	9.89×10^3
Beam S1	45.1	-41.9	6.51×10^3

Table 6.1: Beams N1 and N2 - Comparison of the numerical model and the experimental tests

Maximal Displacement [mm]	10	10	20	20	30	30
Residual Displacement (Numerical) [mm]	2.1	2.1	11.4	11.3	20.5	20.4
Residual Displacement (Experimental) [mm]	2.5	2.2	11.1	10.9	19.9	19.7

Table 6.2: Beam S1 - Numerical and experimental residual displacements

6.2 Beams N1 and N2

These beams have the same numerical model since they are similar. The numerical analysis was conducted for the three load stages, as the real behaviour of the beams. The VecTor2 model was not able to reproduce a brittle failure of the welded connections, so results will be different after the failure of the beams.

6.2.1 Load-Displacement curves comparison

This data cannot be compared with the data of the experimental tests of the SMA beams in terms of global behaviour. But can be correlated with the numerical data of the beam S1. A similar force resistance capacity is observed but a higher displacement capacity and a lower initial stiffness due to the low stiffness of the SMA compared with the steel.

The Load-Displacement curve of the SMA RC beams N1 and N2 and of the numerical model are given in Fig. 6.2. Both SMA beams have similar behaviour. A good match is obtained between the experimental curves and the numerically calculated curve. Important values for the numerical model (up to 2.8 [mm] displacement, the failure of the experimental beam N2), beam N1 and N2 are summarised in Table 6.3.
The numerical model couldn't catch well the residual displacement and the minimal force applied. For the numerical model, the calculated displacements are in the elastic behaviour of the beam, so after unloading, the beam goes back to almost 0 [mm] displacement with a force quasi null. This is of course a simplification of the reality

to use an elastic linear model. The real behaviour of the beam isn't elastic up to failure. This lead to bigger deformation and force to go back to the original position.

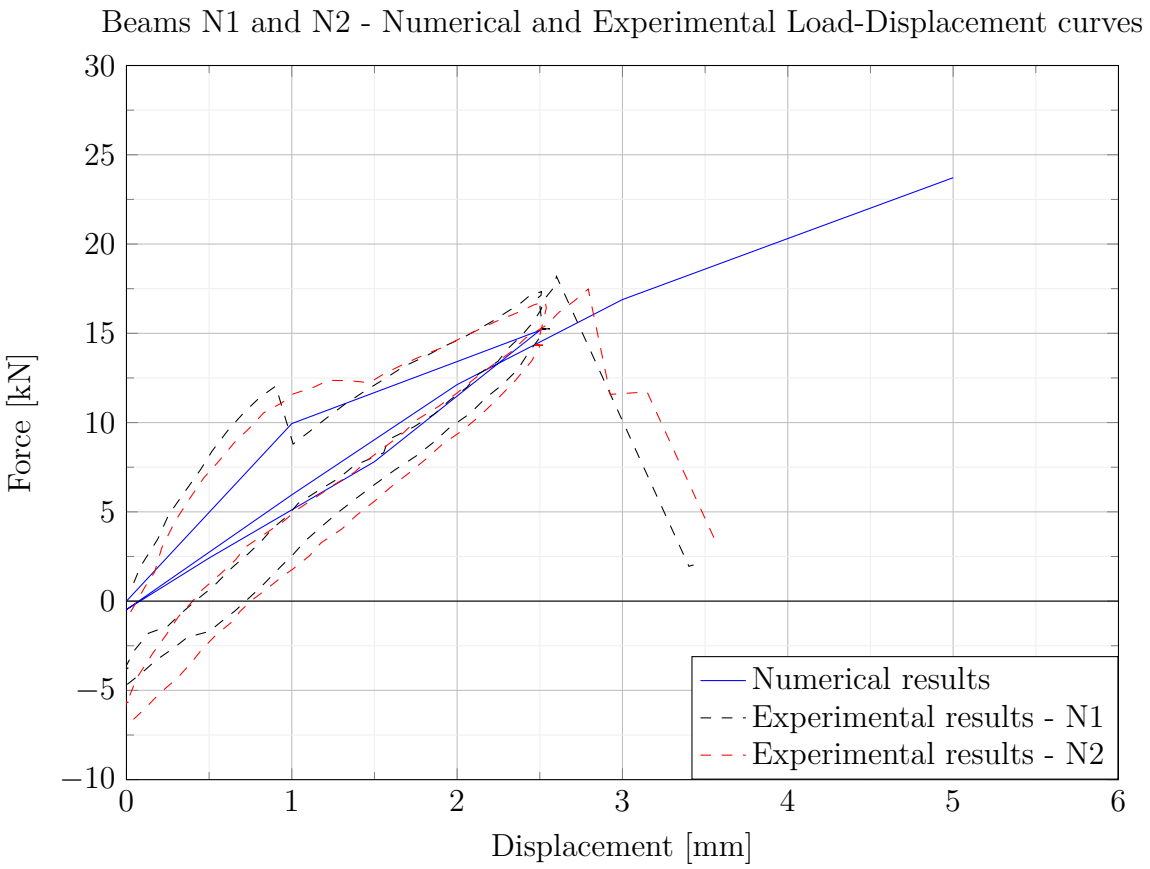


Figure 6.2: Beams N1 and N2 - Numerical and experimental Load-Displacement responses

6.2.2 Residual displacements comparison

The calculated residual displacement doesn't represent well the real behaviour of the beams and is written in Table 6.3. The global behaviour is well represented but the fact that SMA is used in the numerical model adds complexity to the model and the equations used to model the reality. Simplifications in the equations, simplified behaviour of steel, concrete and SMA lead to inaccuracies in the final result. Furthermore, the welded connection isn't modelled in VecTor2, this numerical simplification can lead to inexact behaviour.
Table 5.2 summarises the numerically calculated residual displacements of Beam

	Maximal Force [kN]	Minimal Force [kN]	Residual Displacement [mm]	Initial Stiffness [kN/m]
Numerical Model	15.9	-0.5	0.1	9.84×10^3
Beam N1	18.2	-4.8	0.7	15.24×10^3
Beam N2	17.5	-6.9	0.7	12.88×10^3

Table 6.3: Beams N1 and N2 - Comparison of the numerical model and the experimental tests

N1. These values can be compared with the residual displacement of Beam S1 (Table 6.2), and it can be seen that the residual displacements of Beam N1 are much smaller for the same imposed vertical displacement than Beam S1. For example, at 30 [mm] of vertical displacement, the numerical residual displacement of Beam S1 is 20.4 [mm] while it's only 2.7 [mm] for Beam N1.
According to the numerical analysis, the objective of reducing the residual displacements is well fulfilled.

CHAPTER

7

CONCLUSION

The literature review presented in Chapter 2 shows that SMA can be used as seismic reinforcement with great benefits with regard to steel reinforcement. The main advantages are the shape memory effect and the superelasticity leading to less residual displacement and self-centring behaviour of RC structures. SMA can also be used for the strengthening of existing structures as described in Chapter 2.

The author presented new tests with SMA in two beams and compare them with one control RC beam. A numerical study is also conducted and compared with the experimental results. The main conclusions are the following:

- The welded connections between steel and SMA had a brittle failure occurring very early during the loading protocol in comparison with the estimated resistance of this connection. Although this type of connection failed for these tests, with more research and tests on this linkage, promising results can be found.
- The SMA beams have a greater initial stiffness than the RC control beam, but the maximal force for an imposed displacement is smaller for SMA beams than for the control RC beam.
- In the SMA beams, the strains are very concentrated in the SMA, and thus

this part will lead the behaviour of the beam in flexion.

➢ The numerical model for RC beam with VecTor2 two gives satisfactory results in terms of initial stiffness, residual displacements and minimal forces, while the maximal applied forces are too important. Response-2000 as for it gives a good estimation of the maximal force.

7.1 Future developments

But this work can be continued on several points, for example, a focus on the welded link between SMA and steel to achieve a complete mastery of the process in order to avoid brittle failure during the experimental tests. If that is done, conclusions can be drawn in terms of residual displacements and possible gain in RC SMA structures in comparison with classical RC structures.
Another aspect that can be developed and studied is the strain rate effect of RC structures reinforced with SMA.
Also, more advanced numerical studies can be done to really match the behaviour of RC structures and evenly of big RC structures such as building with SMA at the base (at the plastic hinge).

BIBLIOGRAPHY

[1] Our World in Data. accessed 09 June 2022. URL: https://ourworldindata.org/natural-disasters#natural-disasters-kill-tens-of-thousands-each-year.

[2] CRED/UCLouvain EM-DAT. accessed 09 June 2022. URL: https://public.emdat.be/.

[3] Frédéric Marquis, Jenna Jihyun Kim, and Stephanie E. Elwood Kenneth J.and Chang. "Understanding post-earthquake decisions on multi-storey concrete buildings in Christchurch, New Zealand". In: *Bulletin of Earthquake Engineering* (2017). DOI: 10.1007/s10518-015-9772-8. URL: https://doi.org/10.1007/s10518-015-9772-8.

[4] CEN. "Eurocode 8 - Design of structures for earthquake resistance". In: *E. S. E. 1998-1:2004 (Ed.). In. Brussels, Belgium, 2004: Comité Européen de Normalisation; 2004* ().

[5] Andrew Hamilton Buchanan et al. "Base Isolation and Damage-Resistant Technologies for Improved Seismic Performance of Buildings". In: 2011.

[6] João Saraiva Esteves Pacheco De Almeida. "LGCIV2042 - Earthquake engineering course at UCLouvain". In: (2021).

[7] Ryan D. Hoult and João Pacheco de Almeida. "Residual displacements of reinforced concrete walls detailed with conventional steel and shape memory alloy rebars". In: *Engineering Structures* 256 (2022), p. 114002. ISSN: 0141-0296. DOI: https://doi.org/10.1016/j.engstruct.2022.114002. URL: https://www.sciencedirect.com/science/article/pii/S0141029622001523.

[8] All Answers Ltd. *Shape Memory Alloys in Aerospace Applications [Internet]*. November 2018. [Accessed 9 April 2022]. URL: https://ukdiss.com/examples/shape-memory-alloy-actuator.php.

[9] Saim Raza et al. "Shape memory alloy reinforcement for strengthening and self-centering of concrete structures—State of the art". In: *Construction and Building Materials* 324 (2022), p. 126628. ISSN: 0950-0618. DOI: https://doi.org/10.1016/j.conbuildmat.2022.126628. URL: https://www.sciencedirect.com/science/article/pii/S0950061822003191.

[10] Alaa Abdulridha. *Performance of Superelastic Shape Memory Alloy Reinforced Concrete Elements Subjected to Monotonic and Cyclic Loading*. 2013.

[11] Donghyuk Jung, James Wilcoski, and Bassem Andrawes. "Bidirectional shake table testing of RC columns retrofitted and repaired with shape memory alloy spirals". In: *Engineering Structures* 160 (2018), pp. 171–185. ISSN: 0141-0296. DOI: https://doi.org/10.1016/j.engstruct.2017.12.046. URL: https://www.sciencedirect.com/science/article/pii/S0141029616310112.

[12] M. Motavalli; C. Czaderski; A. v Bergamini and L. Janke. *Application of shape memory alloys in civil engineering; past, present and future*.

[13] M. Saiid Saiidi et al. "Pilot Study of Behavior of Concrete Beams Reinforced with Shape Memory Alloys". In: *Journal of Materials in Civil Engineering* 19.6 (2007), pp. 454–461. DOI: 10.1061/(ASCE)0899-1561(2007)19:6(454).

[14] Adolfo Preciado, Gianni Bartoli, and Harald Budelmann. "The Use of Prestressing Through Time as Seismic Retrofitting of Historical Masonry Constructions: Past, Present and Future Perspective". In: *Journal Ciencia Ergo-Sum ISSN: 1405-0269* 22 (Aug. 2015), pp. 1–11.

[15] Maria Gabriella Castellano, Maurizio Indirli, and Alessandro Martelli. "Progress of application, research and development, and design guidelines for shape memory alloy devices for cultural heritage structures in Italy". In: *Proceedings of SPIE - The International Society for Optical Engineering* (July 2001). DOI: 10.1117/12.434124.

[16] Alessandra Bonci et al. "USE OF SHOCK TRANSMISSION UNITS AND SHAPE MEMORY ALLOY DEVICES FOR THE SEISMIC PROTECTION OF MONUMENTS : THE CASE OF THE UPPER BASILICA OF SAN FRANCESCO AT ASSISI". In: 2001.

[17] AHM Muntasir Billah, Jesika Rahman, and Qi Zhang. "Shape memory alloys (SMAs) for resilient bridges: A state-of-the-art review". In: *Structures* 37 (2022), pp. 514–527. ISSN: 2352-0124. DOI: https://doi.org/10.1016/j.istruc.2022.01.034. URL: https://www.sciencedirect.com/science/article/pii/S2352012422000340.

[18] Parviz Soroushian et al. “Repair and Strengthening of Concrete Structures Through Application of Corrective Posttensioning Forces with Shape Memory Alloys”. In: *Transportation Research Record* 1770 (Jan. 2001), pp. 20–26. DOI: 10.3141/1770-03.

[19] Adolfo Preciado, Gianni Bartoli, and Harald Budelmann. “The Use of Prestressing Through Time as Seismic Retrofitting of Historical Masonry Constructions: Past, Present and Future Perspective”. In: *Journal Ciencia Ergo-Sum ISSN: 1405-0269* 22 (Aug. 2015), pp. 1–11.

[20] Odd Akselsen. “Joining of Shape Memory Alloys”. English. In: IntechOpen, 2010. ISBN: 9789533071060;9533071060;

[21] Matthieu B. Lezaack et al. “Dissimilar friction welding of NiTi shape memory alloy and steel reinforcing bars for seismic performance”. English. In: *Science and Technology of Welding and Joining* (2022).

[22] João Pacheco de Almeida et al. “Shape-memory NiTi alloy rebars in flexural-controlled large-scale reinforced concrete walls: Experimental investigation on self-centring and damage limitation”. In: *Engineering Structures* 220 (2020), p. 110865. ISSN: 0141-0296. DOI: https://doi.org/10.1016/j.engstruct.2020.110865. URL: https://www.sciencedirect.com/science/article/pii/S0141029620301851.

[23] M. Shahria Alam, Maged A. Youssef, and Moncef L. Nehdi. “Exploratory investigation on mechanical anchors for connecting SMA bars to steel or FRP bars”. In: vol. 43. Dec. 2010. DOI: 10.1617/s11527-010-9601-0. URL: https://doi.org/10.1617/s11527-010-9601-0.

[24] Zongcai Deng, Qingbin Li, and Hongjun Sun. “Behavior of concrete beam with embedded shape memory alloy wires”. In: *Engineering Structures* 28.12 (2006), pp. 1691–1697. ISSN: 0141-0296. DOI: https://doi.org/10.1016/j.engstruct.2006.03.002. URL: https://www.sciencedirect.com/science/article/pii/S014102960600109X.

[25] Hui Li, Zhi-qiang Liu, and Jin-ping Ou. “Experimental study of a simple reinforced concrete beam temporarily strengthened by SMA wires followed by permanent strengthening with CFRP plates”. In: *Engineering Structures* 30.3 (2008), pp. 716–723. ISSN: 0141-0296. DOI: https://doi.org/10.1016/j.engstruct.2007.05.020. URL: https://www.sciencedirect.com/science/article/pii/S0141029607002295.

[26] Yachuan Kuang and Jinping Ou. “Self-repairing performance of concrete beams strengthened using superelastic SMA wires in combination with adhesives released from hollow fibers”. In: *Smart Materials and Structures*

17.2 (Feb. 2008), p. 025020. DOI: 10.1088/0964-1726/17/2/025020. URL: https://doi.org/10.1088/0964-1726/17/2/025020.

[27] Alaa Abdulridha et al. "Behavior and modeling of superelastic shape memory alloy reinforced concrete beams". In: *Engineering Structures* 49 (2013), pp. 893–904. ISSN: 0141-0296. DOI: https://doi.org/10.1016/j.engstruct.2012.12.041. URL: https://www.sciencedirect.com/science/article/pii/S0141029613000114.

[28] Kshitij C Shrestha et al. "Feasibility of Cu–Al–Mn superelastic alloy bars as reinforcement elements in concrete beams". In: *Smart Materials and Structures* 22.2 (Jan. 2013), p. 025025. DOI: 10.1088/0964-1726/22/2/025025. URL: https://doi.org/10.1088/0964-1726/22/2/025025.

[29] Adeel Zafar and Bassem Andrawes. "Experimental flexural behavior of SMA-FRP reinforced concrete beam". In: *Frontiers of Structural and Civil Engineering* 7 (Dec. 2013), pp. 341–355. DOI: 10.1007/s11709-013-0221-y.

[30] Sanjay Pareek et al. "Feasibility of externally activated self-repairing concrete with epoxy injection network and Cu-Al-Mn superelastic alloy reinforcing bars". In: *Smart Materials and Structures* 23.10 (Sept. 2014), p. 105027. DOI: 10.1088/0964-1726/23/10/105027. URL: https://doi.org/10.1088/0964-1726/23/10/105027.

[31] Moslem Shahverdi, Christoph Czaderski, and Masoud Motavalli. "Iron-based shape memory alloys for prestressed near-surface mounted strengthening of reinforced concrete beams". In: *Construction and Building Materials* 112 (2016), pp. 28–38. ISSN: 0950-0618. DOI: https://doi.org/10.1016/j.conbuildmat.2016.02.174. URL: https://www.sciencedirect.com/science/article/pii/S0950061816302355.

[32] Moslem Shahverdi et al. "Strengthening of RC beams by iron-based shape memory alloy bars embedded in a shotcrete layer". In: *Engineering Structures* 117 (2016), pp. 263–273. ISSN: 0141-0296. DOI: https://doi.org/10.1016/j.engstruct.2016.03.023. URL: https://www.sciencedirect.com/science/article/pii/S0141029616300438.

[33] Benito Mas, Antoni Cladera, and Carlos Ribas. "Experimental study on concrete beams reinforced with pseudoelastic Ni-Ti continuous rectangular spiral reinforcement failing in shear". In: *Engineering Structures* 127 (2016), pp. 759–768. ISSN: 0141-0296. DOI: https://doi.org/10.1016/j.engstruct.2016.09.022. URL: https://www.sciencedirect.com/science/article/pii/S0141029616305855.

[34] Nubailah Abd Hamid et al. "Behaviour of smart reinforced concrete beam with super elastic shape memory alloy subjected to monotonic loading". In: *AIP Conference Proceedings* 1958.1 (2018), p. 020034. DOI: 10.1063/1.5034565.

[35] Hothifa Rojob and Raafat El-Hacha. "Self-Prestressing Using Iron-Based Shape Memory Alloy for Flexural Strengthening of Reinforced Concrete Beams". In: *ACI Structural Journal* 114 (2017). DOI: 10.14359/51689455.

[36] Raafat El-Hacha and Hothifa Rojob. "Flexural Strengthening of Large-Scale Reinforced Concrete Beams Using Near-Surface-Mounted Self-Prestressed Iron-Based Shape-Memory Alloy Strips". In: *Pci Journal* 63 (Nov. 2018), pp. 55–65. DOI: 10.15554/pcij63.6-03.

[37] Hothifa Rojob and Raafat El-Hacha. "Fatigue performance of RC beams strengthened with self-prestressed iron-based shape memory alloys". In: *Engineering Structures* 168 (2018), pp. 35–43. ISSN: 0141-0296. DOI: https://doi.org/10.1016/j.engstruct.2018.04.042. URL: https://www.sciencedirect.com/science/article/pii/S0141029617315341.

[38] S. Pareek et al. "Plastic hinge relocation in reinforced concrete beams using Cu-Al-Mn SMA bars". In: *Engineering Structures* 175 (2018), pp. 765–775. ISSN: 0141-0296. DOI: https://doi.org/10.1016/j.engstruct.2018.08.072. URL: https://www.sciencedirect.com/science/article/pii/S0141029617325749.

[39] Kinam Hong et al. "Flexural Response of Reinforced Concrete Beams Strengthened with Near-Surface-Mounted Fe-Based Shape-Memory Alloy Strips". In: *International Journal of Concrete Structures and Materials* 12 (2018). DOI: 10.1186/s40069-018-0279-y. URL: https://doi.org/10.1186/s40069-018-0279-y.

[40] Julien Michels, Moslem Shahverdi, and Christoph Czaderski. "Flexural strengthening of structural concrete with iron-based shape memory alloy strips". In: *Structural Concrete* 19.3 (2018), pp. 876–891. DOI: https://doi.org/10.1002/suco.201700120. eprint: https://onlinelibrary.wiley.com/doi/pdf/10.1002/suco.201700120. URL: https://onlinelibrary.wiley.com/doi/abs/10.1002/suco.201700120.

[41] Luis A. Montoya-Coronado et al. "Experimental study on shear strengthening of shear critical RC beams using iron-based shape memory alloy strips". In: *Engineering structures* 200 (2019), p. 109680.

[42] Emanuel Strieder et al. "Strengthening of Reinforced Concrete Beams with Externally Mounted Sequentially Activated Iron-Based Shape Memory Alloys". In: *Materials* 12.3 (2019). ISSN: 1996-1944. DOI: 10.3390/ma12030345. URL: https://www.mdpi.com/1996-1944/12/3/345.

[43] Joan M. Rius et al. “Shear strengthening of reinforced concrete beams using shape memory alloys”. In: *Construction and Building Materials* 200 (2019), pp. 420–435. ISSN: 0950-0618. DOI: https://doi.org/10.1016/j.conbuildmat.2018.12.104. URL: https://www.sciencedirect.com/science/article/pii/S0950061818330903.

[44] Arkabrata Sinha, Nikola Tatar, and Jovan Tatar. “Rapid heat-activated post-tensioning of damaged reinforced concrete girders with unbonded near-surface mounted (NSM) NiTiNb shape-memory alloy wires”. In: *Materials and Structures* 53 (2020). DOI: 10.1617/s11527-020-01522-8. URL: https://doi.org/10.1617/s11527-020-01522-8.

[45] Antoni Cladera et al. “Shear strengthening of slender reinforced concrete T-shaped beams using iron-based shape memory alloy strips”. In: *Engineering Structures* 221 (2020), p. 111018. ISSN: 0141-0296. DOI: https://doi.org/10.1016/j.engstruct.2020.111018. URL: https://www.sciencedirect.com/science/article/pii/S0141029620305587.

[46] F. Azadpour and A.A. Maghsoudi. “Experimental and analytical investigation of continuous RC beams strengthened by SMA strands under cyclic loading”. In: *Construction and Building Materials* 239 (2020), p. 117730. ISSN: 0950-0618. DOI: https://doi.org/10.1016/j.conbuildmat.2019.117730. URL: https://www.sciencedirect.com/science/article/pii/S0950061819331836.

[47] Christoph Czaderski, Moslem Shahverdi, and Julien Michels. “Iron based shape memory alloys as shear reinforcement for bridge girders”. In: *Construction and Building Materials* 274 (2021), p. 121793. ISSN: 0950-0618. DOI: https://doi.org/10.1016/j.conbuildmat.2020.121793. URL: https://www.sciencedirect.com/science/article/pii/S0950061820337971.

[48] E. Effendy et al. “Seismic Behavior of Low-Rise Shear Walls with SMA Bars”. In: *Earth & Space 2006*, pp. 1–8. DOI: 10.1061/40830(188)137.

[49] Alaa Abdulridha and Dan Palermo. “Behaviour and modelling of hybrid SMA-steel reinforced concrete slender shear wall”. In: *Engineering Structures* 147 (2017), pp. 77–89. ISSN: 0141-0296. DOI: https://doi.org/10.1016/j.engstruct.2017.04.058. URL: https://www.sciencedirect.com/science/article/pii/S0141029617312038.

[50] Leonardo Cortés-Puentes et al. “Cyclic loading testing of repaired SMA and steel reinforced concrete shear walls”. In: *Engineering Structures* 168 (2018), pp. 128–141. ISSN: 0141-0296. DOI: https://doi.org/10.1016/j.engstruct.2018.04.044. URL: https://www.sciencedirect.com/science/article/pii/S0141029617331991.

[51] W. Leonardo Cortés-Puentes and Dan Palermo. "Seismic Retrofit of Concrete Shear Walls with SMA Tension Braces". In: *Journal of Structural Engineering* 144.2 (2018), p. 04017200. DOI: 10.1061/(ASCE)ST.1943-541X.0001936.

[52] S Yan et al. "Experimental research on resilient performances of Fe-based SMA-reinforced concrete shear walls". In: *IOP Conference Series: Earth and Environmental Science* 189 (Nov. 2018), p. 032028. DOI: 10.1088/1755-1315/189/3/032028. URL: https://doi.org/10.1088/1755-1315/189/3/032028.

[53] Mohammad Javad Tolou Kian and Carlos Cruz-Noguez. "Reinforced Concrete Shear Walls Detailed with Innovative Materials: Seismic Performance". In: *Journal of Composites for Construction* 22.6 (2018), p. 04018052. DOI: 10.1061/(ASCE)CC.1943-5614.0000893.

[54] Brian Nakashoji. "Seismic Performance of Square Nickel-Titanium Reinforced ECC Columns with Headed Couplers". In: 2014.

[55] M.S. Saiidi and H. Wang. "Exploratory study of seismic response of concrete columns with shape memory alloys reinforcement". In: 103 (May 2006), pp. 436–443.

[56] Saiid Saiidi, Melissa O'Brien, and S.-Z Mahmoud. "Cyclic Response of Concrete Bridge Columns Using Superelastic Nitinol and Bendable Concrete". In: *Aci Structural Journal* 106 (Jan. 2009), pp. 69–77.

[57] Moochul Shin and Bassem Andrawes. "Emergency repair of severely damaged reinforced concrete columns using active confinement with shape memory alloys". In: *Smart Materials and Structures* 20.6 (May 2011), p. 065018. DOI: 10.1088/0964-1726/20/6/065018. URL: https://doi.org/10.1088/0964-1726/20/6/065018.

[58] Moochul Shin and Bassem Andrawes. "Lateral Cyclic Behavior of Reinforced Concrete Columns Retrofitted with Shape Memory Spirals and FRP Wraps". In: *Journal of Structural Engineering* 137.11 (2011), pp. 1282–1290. DOI: 10.1061/(ASCE)ST.1943-541X.0000364.

[59] Carlos A. Cruz Noguez and M. Saiid Saiidi. "Shake-Table Studies of a Four-Span Bridge Model with Advanced Materials". In: *Journal of Structural Engineering* 138.2 (2012), pp. 183–192. DOI: 10.1061/(ASCE)ST.1943-541X.0000457.

[60] Eunsoo Choi et al. "Seismic protection of lap-spliced RC columns using SMA wire jackets". In: *Magazine of Concrete Research* 64.3 (2012), pp. 239–252. DOI: 10.1680/macr.10.00181. eprint: https://doi.org/10.1680/macr.10.00181. URL: https://doi.org/10.1680/macr.10.00181.

[61] F Hosseini et al. “An experimental investigation of innovative bridge columns with engineered cementitious composites and Cu–Al–Mn super-elastic alloys”. In: *Smart Materials and Structures* 24.8 (July 2015), p. 085029. DOI: 10.1088/0964-1726/24/8/085029. URL: https://doi.org/10.1088/0964-1726/24/8/085029.

[62] Mostafa Tazarv and M. Saiid Saiidi. “Low-Damage Precast Columns for Accelerated Bridge Construction in High Seismic Zones”. In: *Journal of Bridge Engineering* 21.3 (2016), p. 04015056. DOI: 10.1061/(ASCE)BE.1943-5592.0000806.

[63] Sebastian Varela and M ‘Saiid’ Saiidi. “A bridge column with superelastic NiTi SMA and replaceable rubber hinge for earthquake damage mitigation”. In: *Smart Materials and Structures* 25.7 (May 2016), p. 075012. DOI: 10.1088/0964-1726/25/7/075012. URL: https://doi.org/10.1088/0964-1726/25/7/075012.

[64] Sebastian Varela and Mehdi Saiidi. “Resilient deconstructible columns for accelerated bridge construction in seismically active areas”. In: *Journal of Intelligent Material Systems and Structures* 28.13 (2017), pp. 1751–1774. DOI: 10.1177/1045389X16679285. eprint: https://doi.org/10.1177/1045389X16679285. URL: https://doi.org/10.1177/1045389X16679285.

[65] Guohua Xing et al. “Enhancing flexural capacity of RC columns through near surface mounted SMA and CFRP bars”. In: *Journal of Composite Materials* 54.29 (2020), pp. 4661–4676. DOI: 10.1177/0021998320937054. eprint: https://doi.org/10.1177/0021998320937054. URL: https://doi.org/10.1177/0021998320937054.

[66] M. A. Youssef, M. S. Alam, and M. Nehdi. “Experimental Investigation on the Seismic Behavior of Beam-Column Joints Reinforced with Superelastic Shape Memory Alloys”. In: *Journal of Earthquake Engineering* 12.7 (2008), pp. 1205–1222. DOI: 10.1080/13632460802003082. eprint: https://doi.org/10.1080/13632460802003082. URL: https://doi.org/10.1080/13632460802003082.

[67] M. Nehdi, M. Shahria Alam, and M.A. Youssef. “Development of corrosion-free concrete beam–column joint with adequate seismic energy dissipation”. In: *Engineering Structures* 32.9 (2010), pp. 2518–2528. ISSN: 0141-0296. DOI: https://doi.org/10.1016/j.engstruct.2010.04.020. URL: https://www.sciencedirect.com/science/article/pii/S0141029610001434.

[68] M. S. Alam M. Nehdi and M. A. Youssef. “Seismic behaviour of repaired superelastic shape memory alloy reinforced concrete beam-column joint”. In: *Smart Structures and Systems, vol. 7, no. 5, pp. 329–348* (2011).

[69] Fadi Oudah and Raafat El-Hacha. "Joint performance in concrete beam-column connections reinforced using SMA smart material". In: *Engineering Structures* 151 (2017), pp. 745–760. ISSN: 0141-0296. DOI: https://doi.org/10.1016/j.engstruct.2017.08.054. URL: https://www.sciencedirect.com/science/article/pii/S0141029617327098.

[70] Fadi Oudah and Raafat El-Hacha. "Innovative Self-Centering Concrete Beam-Column Connection Reinforced Using Shape Memory Alloy". In: *ACI Structural Journal* 115 (2018). DOI: 10.14359/51702132.

[71] Özgür Yurdakul, Onur Tunaboyu, and Özgür Avşar. "Retrofit of non-seismically designed beam-column joints by post-tensioned superelastic shape memory alloy bars". In: *Bulletin of Earthquake Engineering* 16 (2018). DOI: 10.1007/s10518-018-0323-y. URL: https://doi.org/10.1007/s10518-018-0323-y.

[72] Fadi Oudah and Raafat El-Hacha. "Monolithic SMA-reinforced double slotted beam-column connection". In: *Smart Materials and Structures* 29.3 (Jan. 2020), p. 035002. DOI: 10.1088/1361-665x/ab62df. URL: https://doi.org/10.1088/1361-665x/ab62df.

[73] Liu Jin et al. "Size effect and strain rate effect on seismic behavior of reinforced concrete beam-column joints". In: *Structural Concrete* 23.3 (2022), pp. 1453–1468. DOI: https://doi.org/10.1002/suco.202100670. eprint: https://onlinelibrary.wiley.com/doi/pdf/10.1002/suco.202100670. URL: https://onlinelibrary.wiley.com/doi/abs/10.1002/suco.202100670.

[74] Domenico Asprone et al. "Influence of strain rate on the seismic response of RC structures". In: *Engineering Structures* 35 (2012), pp. 29–36. ISSN: 0141-0296. DOI: https://doi.org/10.1016/j.engstruct.2011.10.025. URL: https://www.sciencedirect.com/science/article/pii/S0141029611004342.

[75] Hisaaki Tobushi et al. "Influence of strain rate on superelastic properties of TiNi shape memory alloy". In: *Mechanics of Materials* 30.2 (1998), pp. 141–150. ISSN: 0167-6636. DOI: https://doi.org/10.1016/S0167-6636(98)00041-6. URL: https://www.sciencedirect.com/science/article/pii/S0167663698000416.

[76] Sia Nemat-Nasser and Wei-Guo Guo. "Superelastic and cyclic response of NiTi SMA at various strain rates and temperatures". In: *Mechanics of Materials* 38.5 (2006). Shape Memory Alloys, pp. 463–474. ISSN: 0167-6636. DOI: https://doi.org/10.1016/j.mechmat.2005.07.004. URL: https://www.sciencedirect.com/science/article/pii/S0167663605001213.

[77] P. S. Wong, F. J. Vecchio, and H. Trommels. *VECTOR2 AND FORMWORKS USER'S MANUAL SECOND EDITION*. 2013.

[78] Raluca Constantin. “Seismic behaviour and analysis of U-shaped RC walls”. In: 2016.

[79] Jean-François Cap. “LAUCE2031 - Calcul organique du béton at UCLouvain”. In: (2019).

[80] Marina Maciel Soares, Dan Palermo, and Wilmar Leonardo Cortés-Puentes. “Modelling of mid-rise concrete shear walls reinforced with superelastic shape memory alloys: Nonlinear analysis”. In: *Engineering Structures* 247 (2021), p. 113049. ISSN: 0141-0296. DOI: https://doi.org/10.1016/j.engstruct.2021.113049. URL: https://www.sciencedirect.com/science/article/pii/S0141029621011883.

[81] Luna. accessed 10 March 2022. URL: https://lunainc.com/product/odisi-6000-series.

[82] Carlos G. Berrocal, Ignasi Fernandez, and Rasmus Rempling. “Crack monitoring in reinforced concrete beams by distributed optical fiber sensors”. In: *Structure and Infrastructure Engineering* 17.1 (2021), pp. 124–139. DOI: 10.1080/15732479.2020.1731558. URL: https://doi.org/10.1080/15732479.2020.1731558.

[83] University of Toronto Evan Bentz. *Response 2000*. Accessed 13 July 2022. URL: https://response-2000.software.informer.com/1.0/.

[84] *SeismoStruct*. Accessed 13 July 2022. URL: https://seismosoft.com/products/seismostruct/.

APPENDIX

A

CONSTRUCTION OF THE BEAMS



Figure A.1: Cage rebar



Figure A.2: Cage rebar tied



Figure A.3: Concrete cover



Figure A.4: Poured concrete

APPENDIX

B

EXPERIMENTAL TESTS



Figure B.1: Beam S1 - Experimental setup



Figure B.2: Beam S1 - Experimental setup

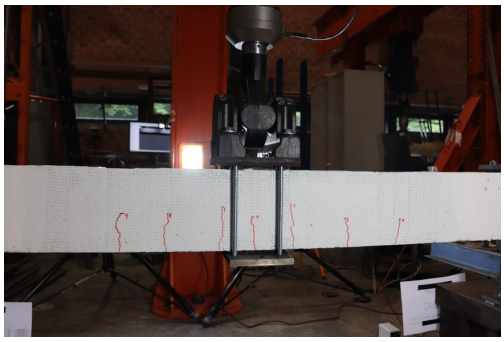


Figure B.3: Beam S1 - First cracks at LS01

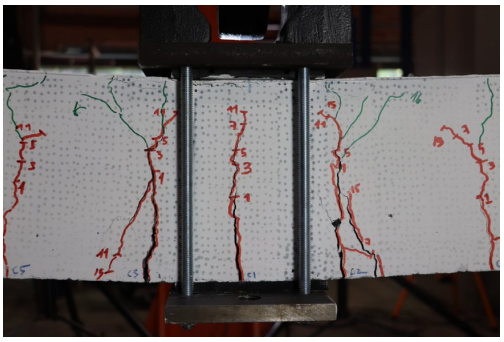


Figure B.4: Beam S1 - Cracks C1, C2 and C3 at LS19



Figure B.5: Beam S1 - Buckling of the bottom longitudinal rebars



Figure B.6: Beam S1 - Load Stage 33 (displacement of 70mm)



Figure B.7: Support conditions



Figure B.8: Support conditions

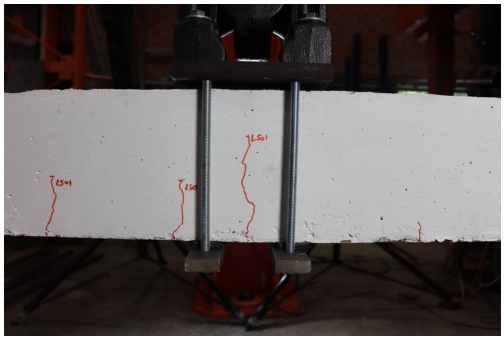


Figure B.9: Beam N1 - First cracks at LS01

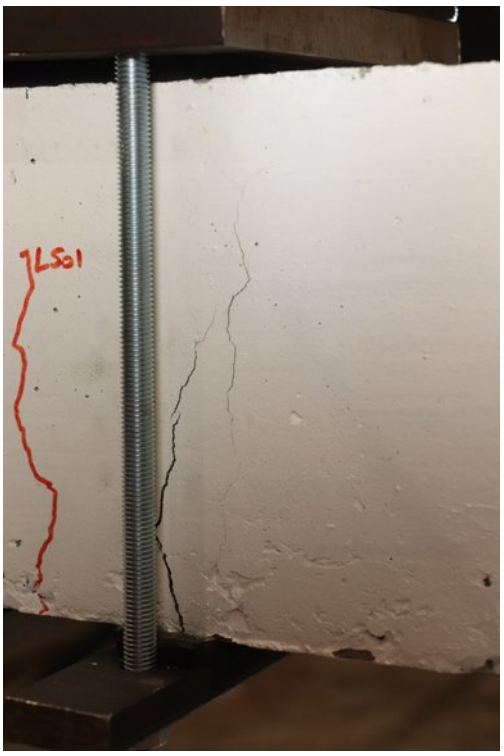


Figure B.10: Beam N1 -Failure of the beam at LS03



Figure B.11: Rupture of the welded connection

APPENDIX

C

STRAINS OF BEAM N2

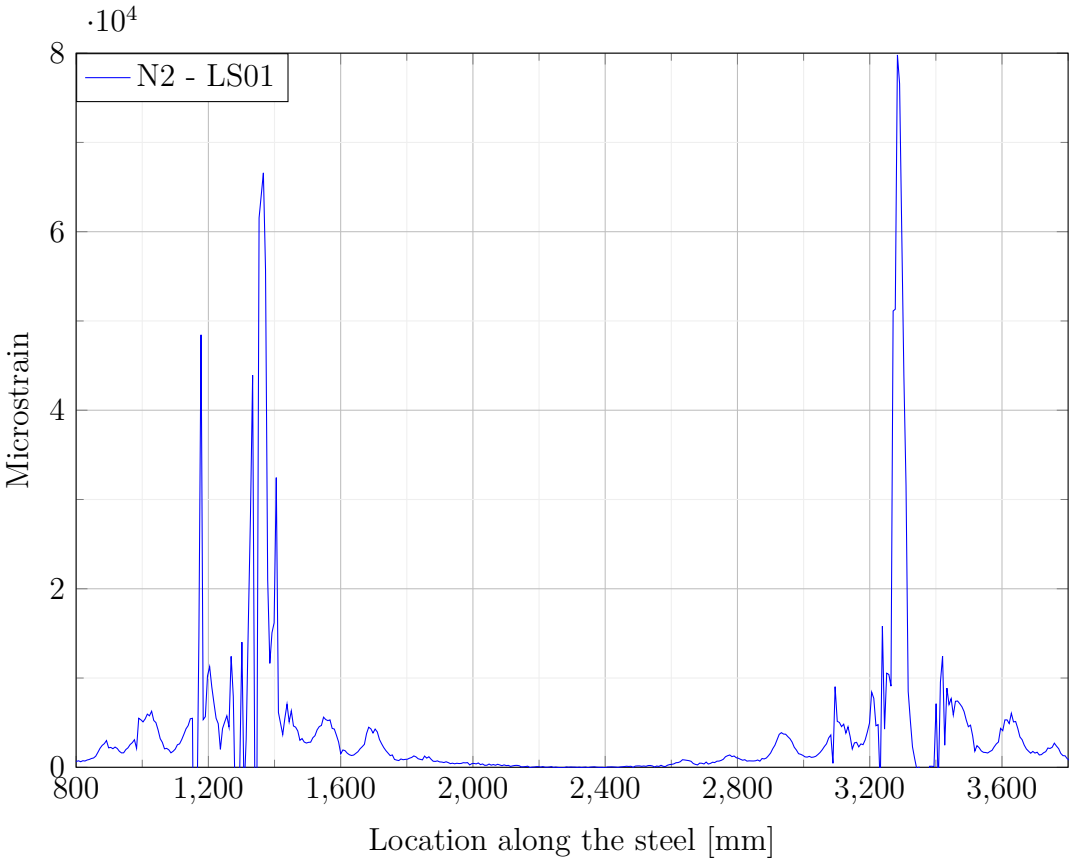


Figure C.1: Beam N2 - Strains in the longitudinal bottom rebars at LS01.

UNIVERSITÉ CATHOLIQUE DE LOUVAIN
École polytechnique de Louvain
Rue Archimède, 1 bte L6.11.01, 1348 Louvain-la-Neuve, Belgique | **www.uclouvain.be/epl**